A Structural and Mechanistic Understanding of Copper(II)-Bis(oxazoline) Catalysed Asymmetric Aziridination; an EPR and ENDOR Investigation

Submitted for the degree of Doctor of Philosophy

by

Mari Elena Owen

School of Chemistry

Cardiff University

September 2013

Acknowledgements

Firstly, I would like to express my thanks to Professor Damien Murphy, for providing me with the opportunity to carry out this research. I am grateful for his supervision and guidance. I must also thank my co-supervisor, Professor Graham Hutchings for his contribution to my research.

My gratitude extends to Dr. Emma Carter; her willingness to share her knowledge and experience has been appreciated.

Furthermore, I would like to thank Dr. Ben Ward for his assistance with the DFT calculations. I am also grateful to Dr. Lucia McDyre and Dr. Tracy Nixon for their help in using air-sensitive techniques.

My thanks must go to Kate for her support and friendship, both inside and outside of the laboratory.

Diolch o galon i'm rhieni am eu cefnogaeth a charedigrwydd trwy gydol fy astudiaethau.

Yn olaf, hoffwn ddiolch yn arbennig i Eilian am ei annogaeth, cymorth a chariad.

Abstract

X- and *Q*-band EPR/ENDOR spectroscopy was used to study the structure of a series of heteroleptic and homoleptic copper(II)-bis(oxazoline) complexes, based on the (−)-2,2′-isopropylidenebis[(4*S*)-4-phenyl-2-oxazoline] (**1**) ligand and bearing different counterions (chloride versus triflate); labelled [Cu(II)(**1a-c**)]. The geometry of the two heteroleptic complexes, [Cu(II)(**1a**)] and [Cu(II)(**1c**)], was found to depend on the choice of counterion. Formation of the homoleptic complex was only evident when the Cu(II)(OTf)$_2$ salt was used whereas Cu(II)Cl$_2$ inhibited the transformation from heteroleptic to homoleptic complex. The hyperfine and quadrupole parameters for the surrounding ligand nuclei were determined by ENDOR. Well resolved ^{19}F and ^{1}H couplings confirmed the presence of both coordinated water and TfO$^-$ counterions in the [Cu(II)(**1a**)] complex.

The structure of other copper(II)-bis(oxazoline) derivatives, based on 2,2'-methylenebis[(4*S*)-4-phenyl-2-oxazoline] (**2**), and 2,2'-isopropylidenebis[(4*S*)-4-*tert*-butyl-2-oxazoline (**3**) were then investigated using *X*- and *Q*-band EPR/ENDOR spectroscopy. Variations in the structures of the complexes as a function of different counterions were also investigated; for ligand **2**, X = TfO$^-$, Cl$^-$ and for ligand **3**, X = TfO$^-$, Cl$^-$, SbF$_6^-$ (where X = counterion). Formation of the homoleptic complex was evident when the Cu(II)(OTf)$_2$ and Cu(II)Cl$_2$ salts were used with ligand **2**, but only when using the Cu(II)(OTf)$_2$ salt with ligand **3**. The substituents on the chiral carbons of the oxazoline rings and on the bridging carbon backbone were found to affect the electron spin density of the structures.

An *X*-band EPR investigation of the interaction of substrates (pyridine, iodobenzene, (diacetoxyiodo)benzene, styrene and PhI=NTs) with [Cu(II)(**1a**)] was also performed, before probing the [Cu(II)(**1a**)] catalysed asymmetric aziridination of styrene, with PhI=NTs as the nitrene source. Using EPR to monitor the course of the reaction after the addition of styrene + PhI=NTs revealed the formation of an additional paramagnetic species, for which the g/^{Cu}A parameters indicated a change to the equatorial environment of the Cu(II) centre. This was discussed within the context of the proposed reaction mechanism which suggests the involvement of a copper-nitrene intermediate.

Table of Contents

Chapter 1

Fundamental concepts of homogeneous catalysis

1.1. Introduction

One of the main uses of transition metals is as catalysts for numerous chemical reactions, including important industrial processes. In this chapter, the concepts of catalysis will firstly be outlined (Section 1.2), including the definition of a catalyst and the advantages of using catalysts in chemical reactions. Once this has been established, a specific type of catalysis, namely asymmetric catalysis, will be considered in some detail (Section 1.3). Asymmetric catalysis is extremely important for reducing the production of unwanted products. A fascinating branch of asymmetric catalysis is that pertaining to *privileged* chiral catalysts (Section 1.4), and the extraordinary features of these highly functional catalysts will be discussed in depth.

The particular privileged chiral catalyst that is the focal point of this work is copper-bis(oxazoline). The structure of the bis(oxazoline) ligand will be described (Section 1.5), with an overview of the various structural variations that have been previously explored in the literature. The catalytic applications of general metal-bis(oxazoline) complexes will also be reviewed, particularly those of copper-bis(oxazoline) complexes (Section 1.6). This will lead to a detailed discussion of the application of copper-bis(oxazoline) as a privileged catalyst in the asymmetric aziridination reaction. This is the foremost reaction of interest in the current research.

The use of the paramagnetic techniques, Electron Paramagnetic Resonance (EPR) and Electron Nuclear DOuble Resonance (ENDOR), to study copper-bis(oxazolines) will then be briefly given (Section 1.7), along with an overview of previous work in the literature relating to the application of these techniques in this field of catalysis. Finally, the aims and objectives of this thesis (Section 1.8) will be discussed in order to provide an understanding of the purpose of the research and an insight into the experimental work that has been performed.

1.2. General concepts of catalysis

"*A catalyst is a substance that changes the rate of a chemical reaction without itself appearing in the products.*" This is the definition given by Ostwald in 1895.[1] Today, a catalyst is described as a substance which increases the rate at which a chemical reaction approaches equilibrium without itself becoming permanently involved.[1] The catalyst decreases the activation energy of the reaction by providing an

alternative pathway that avoids the slow, rate-determining step of the uncatalysed reaction. The rate constant of the reaction is therefore increased in the presence of a catalyst. The energy profiles for catalysed and uncatalysed reactions are compared in Figure 1.1 below.
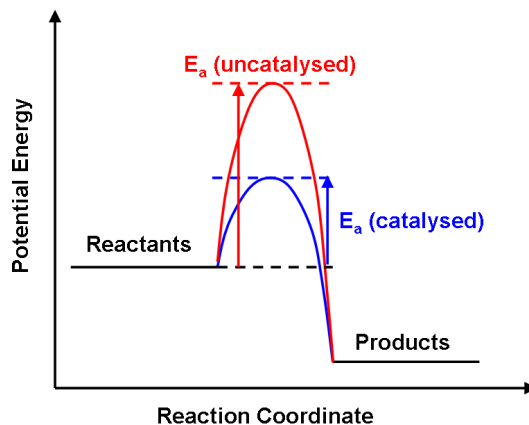
Figure 1.1 A catalyst provides a different reaction pathway with a lower activation energy, resulting in an increase in the rate of formation of products.[2]

If the catalyst and reactants are in the same phase, the reaction is described as homogeneous catalysis, whilst heterogeneous catalysis involves a catalyst which is in a different phase to the reactants. The differences between homogeneous and heterogeneous catalysts are discussed later (Section 1.6). Different classes of catalysts include acid-base catalysts, biological catalysts formed in living cells (primarily enzymes) and organometallic catalysts. Organometallic catalysts consist of a central metal which is surrounded by organic ligands.[1] This type of catalyst is the primary focus of this work.

During the catalytic process, the catalyst may cycle through several intermediate forms.[1] The catalyst can be added to the reactants in the form of the *catalyst precursor*, which must then be activated. Two important values used to measure the efficiency of the catalyst are the turnover number (TON) and the turnover frequency (TOF). The turnover number is the total number of substrate molecules that a catalyst converts into product molecules. This number, within a specific timeframe, is referred to as the turnover frequency.[1]

Different types of selectivity to certain products can be distinguished in a chemical reaction including *chemoselectivity* (selective reaction of one functional group in the presence of two or more different functional groups), *regioselectivity* (selective direction of bond making or breaking over other directions), *enantioselectivity* (selective formation of one specific product enantiomer) and *diastereoselectivity* (selective

formation of one diastereomer).[1] Enantiomers are structures that are not identical, but are mirror images of each other, whilst diastereomers are stereoisomers that are not enantiomers. Examples of these different types of selectivities are illustrated in Figure 1.2. Maximising the selectivity of a reaction enables the reduction of waste, minimises the required work-up equipment and increases the efficiency of feedstock usage.[1,3]
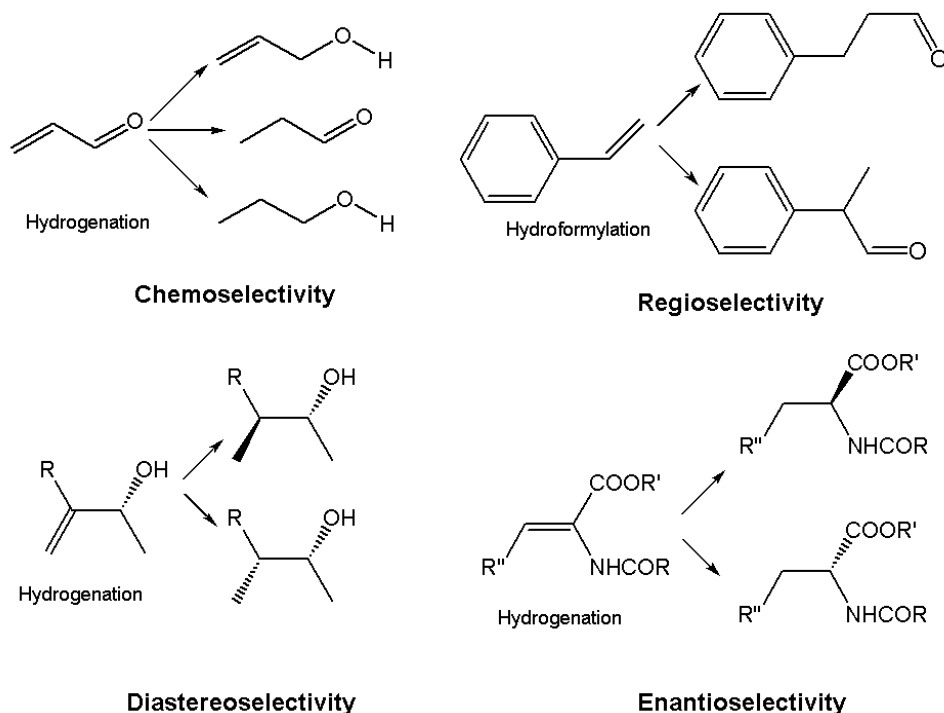
Figure 1.2 Selectivity of chemical conversions.[1]

1.3 Asymmetric catalysis

There is an enormous drive to maximise the enantioselectivity of chemical reactions since enantiomerically pure compounds are mandatory for many applications in the pharmaceutical industry, for vitamins and flavourings and in nonlinear optical and liquid crystalline materials, to name a few.[4] In the field of pharmaceuticals, there are many case studies in which one enantiomer provides the intended effect whilst the other is inactive, or even toxic. A particularly well known example of this is the thalidomide disaster.[5] It is therefore extremely important for chemists to find methods of synthesising the desired compounds with 100% enantiomeric excess (*ee*), and asymmetric catalysis has therefore become an internationally competitive research field in chemistry. To obtain optically pure materials, mixtures of enantiomers can be separated (resolution of racemic mixtures), enantiomerically pure starting materials can be converted, or asymmetric synthesis can be applied.[6]

Enantioselective, asymmetric synthesis involves the preparation of chiral compounds with defined three-dimensional stereochemistry.[7] Structures are *chiral* if they cannot be superimposed upon their mirror image. Chiral molecules are optically active, *i.e.*, they rotate the plane of polarised light. A chiral molecule and its mirror-image partner constitute an enantiomeric pair of isomers, as illustrated with the amino acid example given in Figure 1.3. These optical isomers rotate the plane of polarisation in equal amounts but in opposite directions.[2]
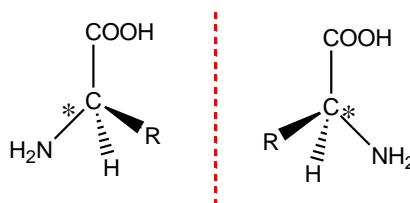
Figure 1.3 The optical isomers of an amino acid, RCHNH$_2$COOH with chiral carbon centres, labelled with asterisks.

Asymmetric synthesis is one of the most active areas of current chemical research because this is a very diverse means of synthesising single enantiomers. This approach can also be beneficial for the environment since the synthesis of unwanted products can be reduced by up to 50%, making product isolation easier and reducing the amount of unwanted material to remove at the end of the reaction.[6,8] In fact, our natural environment demonstrates some of the best examples of asymmetric synthesis. Living systems use enzymes to catalyse stereoselective reactions by exploiting hydrogen bonding, nonbonded dipole-dipole, electrostatic and steric interactions between the active site and substrate, thus controlling the orientation of the substrate and stabilising the transition state, resulting in high levels of stereoselectivity.[7]

Indeed, asymmetric catalysis is an integral aspect of asymmetric synthesis, and a wide range of chiral organometallic catalysts and organocatalysts are now available that attain excellent *ee* levels, with some even mirroring those of enzymes.[9-15] In several of these cases, the enantioselective reaction is catalysed by a chiral Lewis acid complex, often based on main group or transition metal salts coordinated to the chiral organic ligand.[16] Practical asymmetric catalysis was first developed in the early 1970s by Knowles and Kagan.[17,18] Since this discovery, extensive research has been performed in this field, both in academia and in industry. The value of asymmetric catalysis was recognised in 2001, when the Royal Swedish Academy of Sciences awarded the Nobel Prize in Chemistry to three pioneering chemists in the field, William S. Knowles, Ryoji Noyori and K. Barry Sharpless. In his Nobel address, Knowles stated that "*When we started this work we expected these man-made systems to have a highly specific match*

between substrate and ligand, just like enzymes. Generally, in our hands and in the hands of those that followed us, a good candidate has been useful for quite a range of applications."[17] Concurrently, the best asymmetric catalysts are enantioselective over a wide range of substrates, giving the chemist greater scope for investigation.

1.4 'Privileged' catalysts

Certain classes of asymmetric catalysts exhibit excellent enantioselectivities for a large range of substrates and are also active over a variety of different reactions. These have been classified as *privileged chiral catalysts*.[16] Examples of *privileged ligands* include BINOL, the TADDOLate ligand, the salen ligand and the bis(oxazoline) ligand (commonly abbreviated to BOX), as illustrated in Table 1.1.[16] Their wide variety of applications is highlighted in the table and it is this diversity which sets this group of catalysts apart from other asymmetric catalysts. These catalysts continue to find exciting applications in novel enantioselective processes.

Many privileged structures possess a two-fold axis of symmetry. This is an important feature which effectively halves the number of possible transition state geometries available in a particular reaction.[16] These privileged structures are generally very rigid, with several oxygen-, nitrogen- or phosphorous- containing functional groups that allow strong binding to reactive metal centres.[16] Despite these common features, identifying new privileged structures is an exceedingly difficult task as not all privileged structures possess these properties, whilst some structures may possess these properties but do not behave as privileged catalysts.[16]

The method of discovery of each privileged structure illustrated in Table 1.1 is unique. For example, the structures of the TADDOLate and BOX ligands were inspired by natural complexes. The TADDOLate ligand is derived from cheap, readily available tartaric acid whilst the BOX structure is based on the ligand framework of vitamin B_{12}. The inspiration for the design of the chiral manganese salen complex came from the oxo-transfer mechanism of heme-containing enzymes such as cytochrome P-450.[16] BINAP and BINOL on the other hand are completely synthetic molecules which were developed to exploit the axial dissymmetry, induced by the restricted rotation about the biaryl bond.[16]

Table 1.1 Examples of *privileged* chiral ligands and catalysts.[16]

Ligand	Applications
X = OH BINOL X = PPh$_2$ BINAP	Diels-Alder Mukaiyama aldol aldehyde alkylation hydrogenation alkene isomerisation Heck reaction
TADDOLate ligand	Diels-Alder aldehyde alkylation ester alcoholysis iodolactonisation
Salen Complexes	epoxidation epoxide ring-opening Diels-Alder imine cyanation conjugate addition
Bis(oxazoline)	Diels-Alder Mukaiyama aldol conjugate addition cyclopropanation aziridination
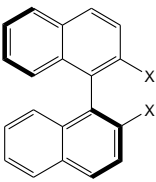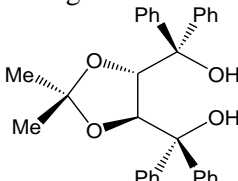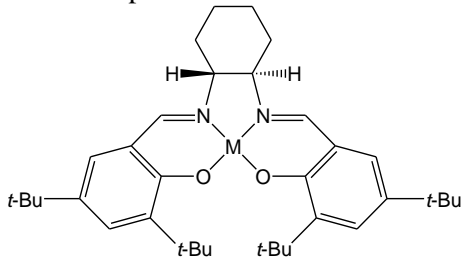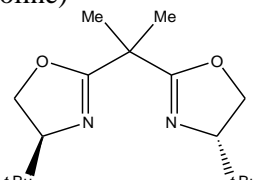
1.5 Bis(oxazoline)-metal complexes

The popularity of the bis(oxazoline) (or BOX) ligands stems from their versatility and efficiency in promoting a range of important enantioselective organic reactions. The potential of C$_2$-symmetric BOX ligands was recognised in the 1990s by numerous research groups, including those of Pfaltz, Masamune, Evans and Corey.[3,19-22] This widespread interest led to the number of applications for the BOX ligand dramatically increasing, and today, the neutral BOX ligands are amongst the most commonly used in asymmetric catalysis.[20] They are employed in an array of enantioselective metal-catalysed processes, including the Diels-Alder reaction, Mukaiyama aldol, conjugate addition, cyclopropanation, aziridination, Lewis acid-catalysed cycloadditions and ene reactions, Michael additions, oxidations and reductions.[16,20] The trajectories from which the reaction substrates can approach C$_2$ symmetric metal-bis(oxazoline) complexes are illustrated in Figure 1.4. This figure

shows that the preferential approach of the reaction substrates is away from the *R* groups of the ligand. This is due to the steric hindrance of these bulky groups.[23]
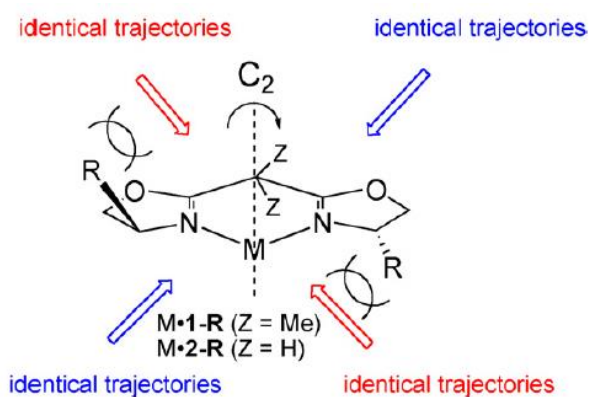
Figure 1.4 C_2 symmetrical metal-bis(oxazoline) complexes.[23]

Another major attraction is that the large majority of these ligands are easily obtained from inexpensive, readily available chiral amino alcohols in a few high-yielding synthetic steps.[24] The standard example of this synthesis involves the reaction of dialkylmalonyl dichloride with an optically active 1,2-amino alcohol, conversion of the bis-hydroxyamide to the corresponding bis-chloroamide, and ring closure under basic conditions.[25] The chiral metal-BOX complex is then prepared by reaction of the BOX ligand with the corresponding metal salt, for example copper triflate. Metal-BOX catalysts usually have a metal to ligand ratio of 1:1. Two metal sites are occupied by the ligand, with up to four available for substrate interactions.[23] The efficiency of the catalyst for asymmetric induction is tested in the reaction of interest, before attempting to identify the reaction intermediate, in order to understand the stereochemical outcome of the catalytic process.[25] The reaction conditions, the reactivity of the metal ions and the ligand structure are important factors which can influence the formation of a heteroleptic (one coordinated ligand) or homoleptic (two coordinated ligands) complex.[26]

The use of chiral, oxazoline-based ligands in asymmetric catalysis was first reported by Brunner *et al.*,[27] in 1986. Following this early pioneering work, numerous BOX ligands with significant structural differences have been synthesised, to optimise catalytic performance for a variety of applications. This field has been most recently reviewed by Desimoni *et al.*[25] Prior to this, extensive reviews had been written by Ghosh and co-workers,[26] as well as McManus and Guiry.[24]

A narrow representation of the various structural deviations of some of the C_2 symmetric BOX ligands is shown in Figure 1.5. Ligands with a single carbon nucleus

bridging between the oxazoline rings are the most commonly employed, as shown in structures **1-11**, but alternatives have been explored in which adjustments have been made to the nature, size and flexibility of the link between the two oxazoline rings.[24] In ligands **12-15**, the oxazoline rings are directly coordinated with no bridging atoms, whilst in structures **16-19** the oxazolines rings are bridged with a pyridine molecule; these are named bis(oxazolinyl) pyridine ligands, commonly known as py-BOX ligands. A diverse range of ligands with one, two or more oxazoline rings, various heteroatoms and additional chiral elements have been synthesised.[24] The ligands illustrated in Figure 1.5 are all of the more common type, *i.e.*, C_2 symmetric ligands with two oxazoline rings.

1 R = Ph[3,28]
2 R = *t*-Bu[22,29]
3 R = CH₃
4 R = CH₂Ph[30]
5 R = *i*-Pr[22,29]
6 R = H (S, S)[31]
7 R = Me (S, S)[32]
8 (R, R)[32]
9 R = H (1S, 2R)[33,34]
10 R = Me (1S, 2R)[33]
11 R-R = CH₂-(CH₂)₁₋₄[35]
12 R = Ph[36]
13 R = CH₂Ph[36]
14 R = *t*-Bu[36]
15 R = *i*-Pr[36]
16 R = Ph[37]
17 R = *t*-Bu[38-41]
18 R = *i*-Pr[38-41]
19 R = *i*-Bu[38-41]

Inda-BOX
9, 10, 11
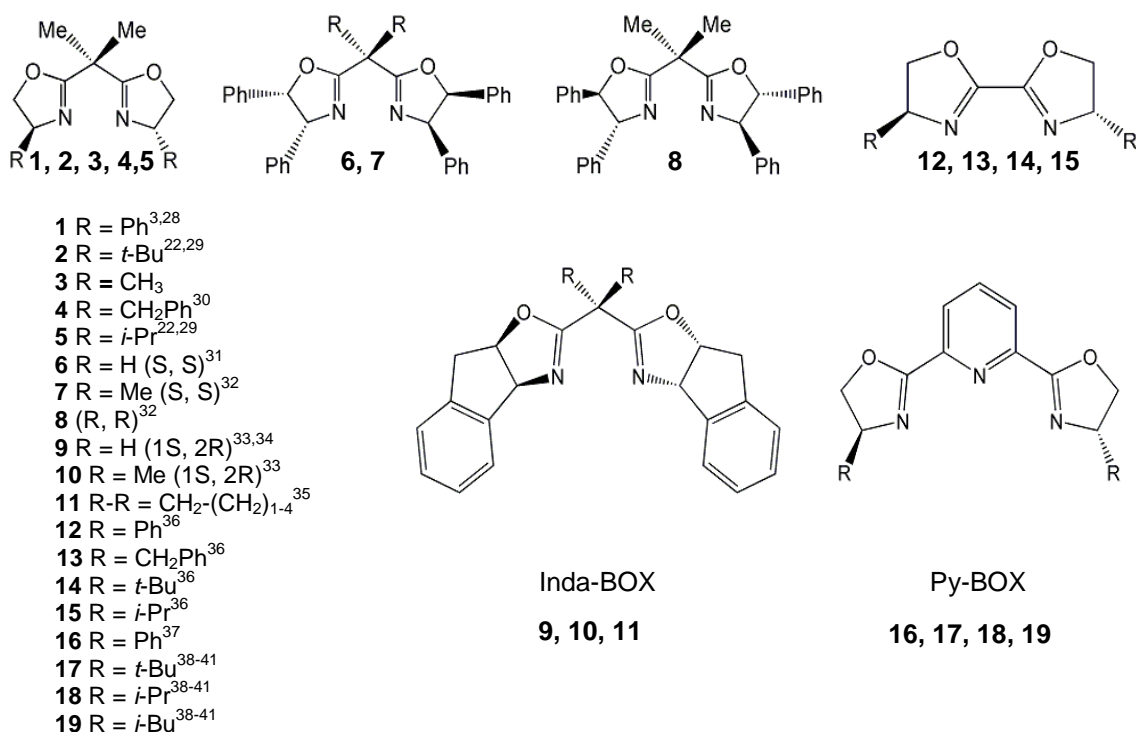
Py-BOX
16, 17, 18, 19

Figure 1.5 Examples of BOX ligand structures.[26]

The denticity of the ligand has also been explored, with examples of monodentate, bidentate, tridentate and tetradentate BOX ligands. Ligands **16-19**, labelled py-BOX ligands, are tridentate ligands, whilst **1-15** are all bidentate. The ability of the metal centre to coordinate through bidentate, tridentate or tetradentate coordination allows the design of the ligand to be adapted for the required catalytic reaction. For example, the tridentate py-BOX ligands were designed by Nishiyama in 1989 for hydrosilyation reactions.[38] Bidentate ligands are however by far the most popular in asymmetric catalysis and Cu(II) is the leading cation involved in their complexation.[25] On coordination of the bidentate ligand, an almost planar metallacycle

is formed. This, along with the presence of the pendent five-membered rings, are useful factors in limiting the flexibility of these ligand systems.[42]

Following the visionary work by Brunner on chiral pyridine-oxazoline ligands,[27] numerous non-symmetrical chiral oxazoline-based ligands have also been reported.[20,24] Synthesising novel BOX ligands is a topical area of research. For example, between 2009 and 2012 alone, Frain *et al*.,[43] synthesised two new 4,4'-BOX ligands, Gök *et al*.,[44] synthesised five new chiral BOX ligands with chiral trans-(2*R*,3*R*)-diphenylcyclopropane backbones, and Jiang *et al*.,[45] published the synthesis of novel chiral BOX ligands with a bipyridinyl backbone.

The ability of the BOX ligand to coordinate with a large number of metals is another important feature. Optimisation of enantioselectivity can be controlled not only by the choice of chiral organic ligand, but also by the choice of metal (Cu, Zn, Ni *etc*.).[23-26,46] Crystal structures have been reported of BOX complexes coordinated to a wide range of metals, including Ag(I), Cu(I), Cu(II), Zn(II), Ni(II), Fe(II), W(0), Rh(II), Ru(II) and Pd(II).[25]

Accordingly, Cu(II) is commonly employed as the cation of choice with BOX ligands due to its efficiency as a Lewis acid centre.[47] In accordance with the Irving-Williams series, Cu(II) forms the most stable ligand-metal complexes (Mn < Fe < Co < Ni < **Cu**).[48] Cu(II) has a strong tendency to form square planar or elongated tetragonal complexes.[49] For [Cu(BOX)](X)$_2$ complexes, where X = weakly or non-coordinating ligand, such as SbF_6^- or TfO^- ($TfO^- = CF_3SO_3^-$), the coordination of a bidentate substrate is favoured in the equatorial plane.[47] Jahn-Teller distortion of Cu(II) d^9 complexes results in an elongation of the remaining apical site.[47] Together, these factors result in well-defined complexes with excellent catalytic properties.

A study by Johnson and Evans,[47] highlights the advantages of using a Cu(II) centre in enantioselective cycloaddition, aldol, Michael, and carbonyl ene reactions. They set out to find the "*best metal centre*" for these reactions, and having studied ten different metal triflates for the Diels-Alder reaction, they found that Cu(OTf)$_2$ was the best in delivering cycloadducts in high diastereomeric excess (*de*) and enantiomeric excesses (*ee*).[47,50] The ability of copper to coordinate to both oxygen and sulphur is also a very useful property.[51] Furthermore, copper is particularly attractive due to its low cost in comparison to other transition metals.

1.6 Homogeneous and heterogeneous applications of Cu-bis(oxazoline) complexes

A homogeneous catalyst is one in which the reaction constituents (substrates and catalyst components) are in the same phase, usually the liquid phase. A heterogeneous catalyst is where one or more of the reaction constituents are in different phases. Examples of homogenous catalysts include Lewis acids (*e.g.,* for Diels-Alder reactions), organic catalysts (*e.g.,* thiazolium ions in Cannizzarro reactions), enzymes and porphyrin complexes (*e.g.,* for epoxidation reactions).[1] Homogeneous catalysis often involves (organo)metallic complexes as the catalyst, which are often transition metal complexes. Heterogeneous catalysis is also very diverse; there are many large-scale industrial processes which employ heterogeneous catalysts, including the Contact process, the Haber-Bosch process and Ziegler-Natta polymerisation.[52]

A heterogeneous catalyst is commonly in the solid phase, with the reactants as liquids or gases. The main advantage of heterogeneous catalysts is the ease of separation from the reaction products. Also, they are often more robust and have longer catalyst lifetimes.[53] In addition to this, heterogeneous catalysts tend to have higher thermal stability than their homogeneous counterparts. This allows reactions to be run under higher temperatures, resulting in increased reaction rates.[54] The local environment of the active metal species in heterogeneous catalysts has a strong impact on the activity and the selectivity of the resulting catalyst.

Unlike heterogeneous catalysts, which usually have a number of different active sites, homogeneous transition metal catalysts usually have only one type of site. This often results in the more reproducible homogeneous catalysts being more catalytically active and more selective, thus producing pure products in high yields. As a result, energy usage, and therefore costs, can be minimised. Mechanistic studies of homogeneous catalysts are usually less complex than those of heterogeneous catalysts. This is largely due to many techniques of physical organic chemistry being more suitable for homogeneous reactions in solution.[55]

Distinguishing between these two categories of catalysts has become more arduous with the advent of "heterogenised homogeneous catalysts," also known as "homogeneous-heterogeneous catalysts," "polymer-supported homogeneous catalysts," or "polymer-anchored catalysts."[53] These are solid and insoluble, but the catalytically active components are the same as those of homogeneous catalysts bound to the surface of polymers. These are treated as homogeneous catalysts because of their chemical behaviour.[53] [Cu(BOX)] is commonly used as a homogeneous catalyst, although numerous research groups have modified the catalyst, through immobilising and

supporting the catalysts by a variety of means.[56] A comprehensive review on the use of BOX ligands for heterogeneous catalytic applications was published in 2002 by Rechavi.[57]

Hutchings and co-workers have conducted extensive research into heterogeneous copper-exchanged zeolite Y modified using bis(oxazolines),[58-61] and were the first to report a heterogeneous catalyst for the asymmetric aziridination of alkenes.[62] Other researchers in this field include Alonso *et al.*,[63] who have immobilised [Cu(BOX)] onto laponite clay and Paluti *et al.*,[64] who immobilised aza-bis(oxazoline) copper complexes onto alkanethiol self-assembled monolayers on gold. These three very different examples emphasise the potential and versatility of immobilised [Cu(BOX)]. Immobilisation of the catalyst overcomes the difficulty of separation and re-use of homogeneous catalysts, which is costly and time-consuming.

Much work has also been performed into investigating SiO_2 supported [Cu(BOX)] systems.[65] Tanaka *et al.*,[66] prepared novel SiO_2-supported chiral [Cu(BOX)] complexes for asymmetric Diels-Alder reactions. A subsequent study by Mayoral *et al.*,[67] also immobilised Cu(II) chiral complexes onto silica, although they were using the IndaBox ligand. Tanaka *et al.*,[66] focused on characterising the [Cu(BOX)] complexes on bare and functionalised SiO_2 surfaces using a wide range of techniques, including X-ray Absorption Fine Structure (XAFS), Electron Paramagnetic Resonance (EPR) and Fourier Transform Infra-Red (FT-IR) spectroscopy, before measuring the catalytic activity. They proposed that the hydrogen bond formation between the chiral BOX ligand and the achiral methacrylate on the silica surface resulted in a "glue effect", increasing the enantioselectivity for the endo product dramatically (in comparison to its homogeneous counterpart). Mayoral *et al.*,[67] took a different approach, instead concentrating on evaluating the effect of surface area and texture on catalytic activity. Their results led to the conclusion that solids with very large pores and low surface area, result in a substantial deactivation upon recovery, whilst the best results were obtained using solids with highly developed surface area. Another study by this group described the immobilisation of supported chiral aza-bis(oxazoline)-copper complexes.[68] Impressively, they could re-use the catalyst up to six times without loss of effectiveness.

Despite the extensive research into heterogeneous metal-BOX catalysts, homogeneous catalysts provide a more diverse range of potential applications and therefore the research into novel applications of oxazoline based catalysts is largely based on homogeneous catalysis. As explained earlier, mechanistic studies of homogenous systems are usually more facile. This benefits researchers looking to

understand the catalytic mechanisms of these systems. The scope of research of the Evans group into homogeneous [Cu(BOX)] catalysed reactions is particularly vast, they have successfully applied this catalyst in a wide range of reactions, including the aziridination of olefins,[69] aldol additions of enolsilates to pyruvate esters,[70] and in the glyoxylate-ene reaction.[71]

Corey *et al.*,[3] first demonstrated the potential of metal-BOX complexes in asymmetric Diels-Alder reactions in 1991, using $FeCl_2$ or FeI_2 as the metal salt. Following this, in 1993, Evans *et al.*,[72-74] demonstrated that copper complexes derived from BOX ligands and mild Lewis acids such as $Cu(OTf)_2$ and $Cu(SbF_6)_2$ are efficient homogeneous chiral catalysts for the Diels-Alder reaction with cyclopentadiene as the diene and various acrylimide derivatives as the dienophile. This reaction scheme is shown in Figure 1.6. Evans and co-workers,[75] also determined that the [Cu(BOX)] catalysed hetero Diels-Alder reaction of crotonyl phosphonate and ethyl vinyl ether gave a high yield and diastereoselectivity, with dihydropyran obtained in 93% *ee*. Interestingly, the derived adduct obtained from *tert*-butyl substituted [Cu(BOX)] gave the opposite enantiomer of that produced using phenyl substituted [Cu(BOX)].[75] This emphasises the importance of the careful selection of ring substituent.
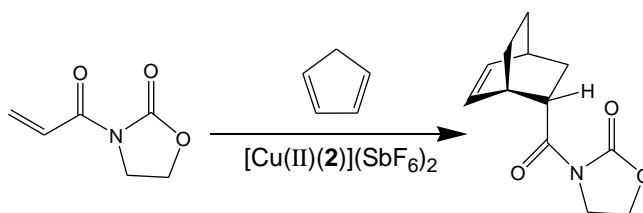
Figure 1.6 Reaction scheme for the [Cu(BOX)] catalysed Diels-Alder reaction.[76] The structure of ligand **2** is shown in Figure 1.5.

Exciting recent developments in homogeneous [Cu(BOX)] catalysed Diels-Alder reactions include the work of Seki and co-workers.[77] They reacted 1,2-dihydropyridine with a chiral oxazolidinone dienophile using ligands **3** and **5** (Figure 1.5) and $Cu(OTf)_2$ to synthesise an endo-isoquinuclidine derivative (97% *de*) with useful medicinal properties. The importance of [Cu(BOX)] was also highlighted in 2010 by Dentel,[78] who carried out asymmetric thia-Diels-Alder reactions involving new dithioesters, and proposed stereochemical models for Cu(II)/BOX/dithioester complexes. This was the first published example of a catalytic asymmetric thia-hetero-Diels-Alder reaction, where a chiral Lewis acid activates the thiocarbonyl dienophile.

The research group of Masamune *et al.*,[21,31] have demonstrated the excellent catalytic potential of homogeneous [Cu(BOX)] complexes for the asymmetric

cyclopropanation of a variety of olefins. Parallel to this work, Evans *et al.*,[22,29] also investigated chiral BOX ligands in cyclopropanation reactions of mono- and 1,1-disubstituted olefins. Unlike the work performed by Masamune, here the active catalyst was prepared by treatment with neutral BOX ligands and CuOTf. Remarkably, almost complete enantioselectivity (>99% *ee*) was observed.[22,29]

1.6.1 The aziridination reaction

Homogeneous and heterogeneous studies of the [Cu(BOX)] catalysed asymmetric aziridination of olefins have been performed by various research groups. In 1993, the Evans and Jacobsen groups simultaneously reported copper catalysed asymmetric aziridination procedures.[79,80] As mentioned earlier, Hutchings and co-workers have published an abundance of reports on their research into the heterogeneous [Cu(BOX)] catalysed aziridination reaction.[58,59,61,81]

Aziridines are saturated three-membered heterocycles which have one nitrogen atom.[82] Developing chiral aziridines is of great importance in synthetic chemistry due to their ease of conversion into many complex molecules, including chiral amines, amino-alcohols and amino acids.[82] This is due to the high strain energy within the aziridine ring, which results in an ability to undergo highly regio- and stereoselective ring opening reactions.[82] The synthesis of aziridines, especially optically active aziridines, is also important due to the anti-tumour and antibiotic properties of numerous aziridine-containing compounds, for example ß-lactam antibiotics.[82]

Optimising the yields and enantioselectivities of [Cu(BOX)] catalysed aziridination reactions improves the efficiency of the reaction. The choice of solvent affects the catalytic performance, with coordinating solvents, such as methanol and acetonitrile, most suitable for [Cu(BOX)] catalysed aziridination. Non-coordinating solvents, such as toluene, result in poor % yields and *ee*.[60]

The choice of nitrene donor has also been shown to influence both the % yield and *ee*. [*N*-(*p*-tolylsulfonyl)imino]phenyliodinane (PhI=NTs, *p*-CH$_3$C$_6$H$_4$SO$_2$N=IPh) was initially used as the nitrene donor. The asymmetric aziridination of styrene, using PhI=NTs as the nitrogen source is described in Figure 1.7.
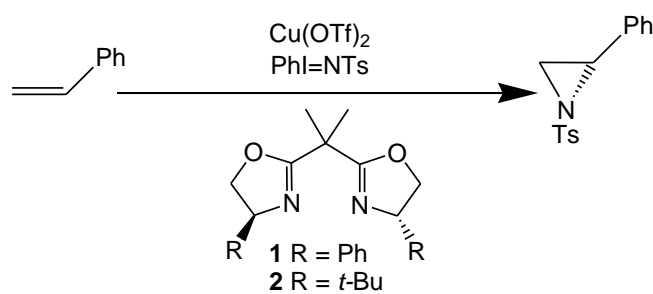
Figure 1.7 Reaction scheme for the [Cu(II)(BOX)] catalysed aziridination of styrene (TfO⁻ = CF₃SO₃⁻, PhI=NTs = p-CH₃C₆H₄SO₂N=IPh)

Subsequent studies have used other nitrene donors, including [N-(p-nitrophenylsulfonyl)-imino]phenyliodinane (PhI=NNs, p-NO₂C₆H₄SO₂N=IPh) and chloramine-T, amongst others.[83-86] Södergren and co-workers,[84] have investigated a range of nitrene donors based on the structure of PhI=NTs, synthesised using variations of the preparation methods of Yamada *et al*.[87] They determined that p-NO₂C₆H₄SO₂N=IPh resulted in higher % yields and % *ee* in comparison to PhI=NTs, for a range of different olefins in [Cu(BOX)] catalysed aziridination reactions. Using methyl styrene, they calculated a yield of 44% when using PhI=NTs, but remarkably, with p-NO₂C₆H₄SO₂N=IPh, the yield increased to 83%. Similarly, the *ee* was 62% when using PhI=NTs, compared to 80% with p-NO₂C₆H₄SO₂N=IPh. Their results suggest that the choice of nitrene donor is crucial for the optimisation of the catalytic reaction for specific substrates.[84] The Hutchings group have also investigated the effect of nitrene donor, comparing PhI=NTs and chloramine-T.[85] They concluded that PhI=NTs was preferable, with significantly higher aziridine yields. This work proceeded that of Aujila *et al*.,[83] who first used chloramine-T as a nitrene donor in the aziridination reaction in an effort to avoid the two-step procedure for synthesisng PhI=NTs.[87]

Careful selection of olefin is also necessary for optimum catalytic performance. Langham *et al*.,[58] determined the yields and enantioselectivities for CuHY-catalysed aziridination for a range of alkenes, including styrene, α-methylstyrene and p-chlorostyrene. From the alkenes which were tested, styrene gave the best yield of product. *Trans*-methyl cinnamate gave matching *ee* to styrene (61%) but the yield was considerably lower.

As mentioned above for the Diels-Alder reaction, the substituents on the BOX ligand can have a direct effect on the product stereochemistry. From an evaluation of ligand architecture, Evans concluded that the phenyl-substituted ligand is superior to the

more sterically demanding *tert*-butyl analogue (using various cinnamate esters as the olefin in the aziridination reaction).[79]

The choice of counterion has also been shown to have a large influence on the catalytic activity, resulting in significant differences in enantioselectivities and yields. Evans *et al*.,[22,79] determined that highly electronegative counterions are essential for efficient asymmetric catalysis, for example $Cu(OTf)_2$ can be used to form an efficient catalyst whilst reactions catalysed by BOX complexes of CuCl are slow, with low enantioselectivities and yields.[79] This is due to the triflate group being more labile and electronegative than the chloride group.[79,88]

There is some ambiguity regarding the mechanism of copper-catalysed olefin aziridination and in particular, the oxidation state of the active catalyst. Evans has noted that both Cu(I)OTf and $Cu(II)(OTf)_2$ can be employed in the formation of chiral bis(oxazoline) catalysts, and that both species result in similar enantioselectivities.[69,79] They have speculated that the active catalyst is in the +2 oxidation state and that PhI=NTs functions as an oxidant for Cu(I). This was demonstrated by comparing the UV-vis spectrum of Cu(I)-bis(oxazoline) + PhI=NTs, with that of Cu(II)-bis(oxazoline) + PhI=NTs. The resulting spectra were indistinguishable, suggesting that a similar catalytically active metal complex is accessible from both the +1 and +2 metal oxidation states.[69] Jacobsen *et al.,*[89] proposed that the Cu(I)-diimine catalysed aziridination reaction proceeds through a discrete Cu(III)-nitrene intermediate (using $Cu(I)PF_6$ as the starting salt) in a redox mechanism, as shown in Figure 1.8 below. This was deduced after using tosyl azide (TsN_3), which is known to extrude dinitrogen under photochemical conditions, as the stoichiometric nitrene source. They have reported that the photochemical reaction of TsN_3 with styrene resulted in the formation of aziridine with the same enantioselectivity as that obtained in the catalytic aziridination reaction, suggesting a common Cu-nitrene intermediate.[89]
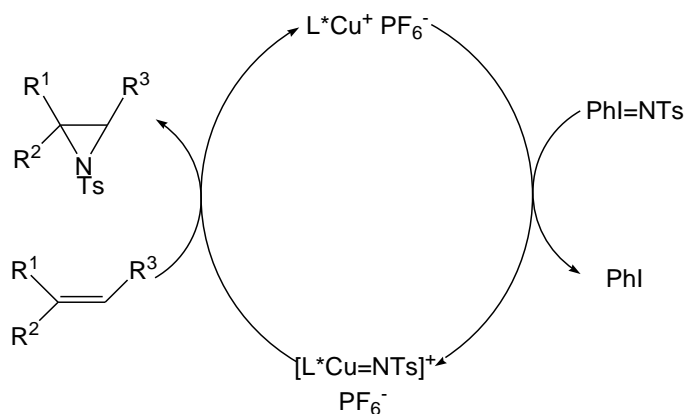
Figure 1.8 Proposed redox mechanism for aziridination.[89]

More recently, after combining the results from hybrid density functional theory (DFT) calculations and kinetic experiements, Brandt *et al.,*[90] provided strong evidence to support the theory of Jacobsen and co-workers,[89] that the active catalyst is a Cu(I) species. They also showed in their calculations how a Cu(II)-catalyst precursor enters the Cu(I)/Cu(III)-cycle through a reaction with PhI=NTs.

Rasappan *et al.,*[23] have reviewed the role of the coordination geometries and electronic properties of metal-bis(oxazoline) complexes in asymmetric induction. After identifying the possible trajectories from which substrates can approach the C_2 metal-bis(oxazolines) (see Figure 1.4), the intermediates of the aziridination reaction are discussed, as illustrated in Figure 1.9. Structures **a** show the possible Cu=NTs intermediates formed by a concerted pathway as proposed by Jacobsen.[89]
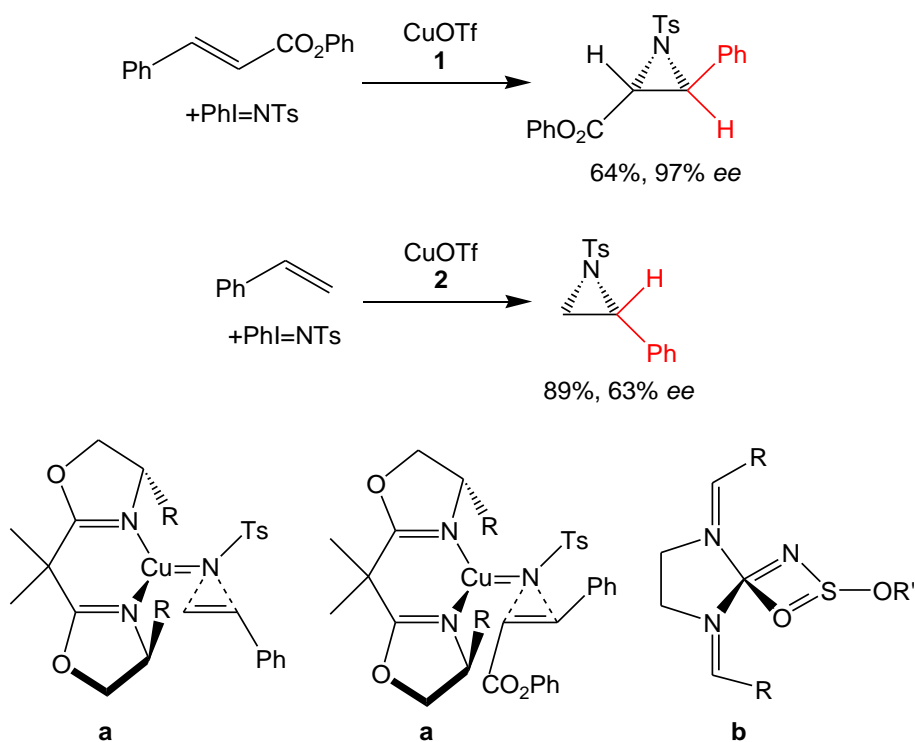
Figure 1.9 Asymmetric aziridination with copper(I)-bis(oxazolines).[23] The structures of ligands **1** and **2** are shown in Figure 1.4.

Figure 1.9 also considers an alternative step-wise mechanism for the aziridination reaction, as suggested by Brandt *et al.*[90] This involves the coordination of the oxygen of the tosyl group, as well as the nitrene moiety, *via* a square planar copper complex, labelled **b**. Nevertheless, a complete structural and electronic understanding of the mechanism has not been achieved, despite these different mechanistic propositions.

1.7 Use of EPR to study Cu-bis(oxazoline) catalysts

In order to understand how asymmetry is transmitted from the catalyst to the substrate, the structure of the ligated catalyst must first be understood. This is easier to determine in catalysts with limited rotational freedom.[42] For paramagnetic Cu(II) based BOX complexes, Electron Paramagnetic Resonance (EPR) and the related hyperfine techniques such as Electron Nuclear DOuble Resonance (ENDOR) are ideal methods to examine the three-dimensional structure of the ligated catalyst, and any structural or electronic perturbations to the metal complex. These techniques will be explained in Chapter 2.

Unlike many other enantioselective reactions, in which the mechanistic details of the asymmetric reactions are well understood, there are still many unknowns in [Cu(BOX)] catalysed reactions. In particular, confusion still remains over the oxidation state of the metal centre, as high yields and selectivities can be obtained from both Cu(I) and Cu(II) precursors.[79] EPR is an ideal tool to probe the mechanistic details of reactions involving transition metal complexes that undergo redox cycles. This has been highlighted by Čaplar *et al.,*[91] who, in their investigation of an oxidation reaction, used EPR spectroscopy to determine the oxidation state of the copper metal centre in 1,5-methylene- and diethylmethylene-bridged BOX ligands.

Despite the many advantages offered by the family of EPR techniques, only a handful of papers containing EPR characterisation of BOX ligands have been reported, and no ENDOR data was published until recently.[92] The limited number of papers which have reported EPR spectra of [Cu(BOX)] complexes have primarily focused on the oxidation state of the copper, and have not investigated other factors such as the effect of the counterion, ligand structure or metal:ligand ratio. Čaplar *et al.*,[91] for example, used EPR only to confirm the presence of a Cu(II) species. Iwasawa *et al.*,[66] reported the EPR spectra of a surface-functionalized SiO_2-supported [Cu(BOX)] complex. The spectra recorded before and after surface functionalisation with a silane coupling reagent were typical of a copper ion in a four coordinate square-planar symmetry. Alonso *et al.*,[63] focused their studies on immobilised [Cu(BOX)] complexes and used EPR, along with IR and EXAFS (Extended X-ray Absorption Fine Structure) to compare the heterogeneous [Cu(BOX)] catalyst (immobilised on laponite clay) with their homogeneous counterparts. In an investigation into the catalytic enantioselective aldol additions of enolsilanes to pyruvate esters, Evans *et al.,*[70] included EPR spectra of [Cu(*tert*-butyl BOX)](OTf)$_2$ with the addition of methyl pyruvate. However, this data was not simulated and no spin Hamiltonian parameters were reported.[70]

1.8 Aims and objectives

Herein, of this thesis, *X*- and *Q*-band EPR and ENDOR spectroscopies have been used to characterise a series of [Cu(BOX)] complexes synthesised from different Cu(II) starting salts bearing TfO⁻ and Cl⁻ counterions. The effect of changing the ligand architecture has been explored, using commercially available BOX ligands. Variations in the ligand architecture which have been considered are the choice of substituents on the bridging carbon backbone and on the chiral carbons of the oxazoline rings. Additionally, the metal:ligand ratio has been studied, in order to assess the sensitivity of the metal and ligand complexation to this ratio. The resulting EPR and ENDOR spectra have been simulated and analysed in order to achieve a greater understanding of the electronic properties and structural details of these complexes. These results have been considered alongside the relevant catalytic information, in order to evaluate their implications on the catalytic properties of these [Cu(BOX)] complexes.

Subsequently, EPR was used to probe the structural and electronic elements of individual substrate interaction (including pyridine, iodobenzene, (diacetoxyiodo)-benzene, styrene and PhI=NTs). The role of [Cu(II)(BOX)] in the asymmetric aziridination reaction, with PhI=NTs as the nitrene donor and styrene as the olefin, has been explored. The progress of the reaction after the addition of PhI=NTs and styrene has been followed using EPR, with the aim to gain an increased understanding of the reaction mechanism and any catalytic intermediates. EPR spectroscopy has been used to observe changes in [Cu(II)] concentration and also to determine whether any additional paramagnetic species were formed during the reaction.

To summarise the contents of the thesis: Chapter 2 explains the theory of the paramagnetic EPR and ENDOR techniques, with particular emphasis on the paramagnet of interest, Cu(II). Chapter 3 gives details of the experimental procedures used, both to prepare the complexes and the measurement conditions. The focus of Chapter 4 is a detailed study of the counterion effect and the implications of changing the metal:ligand ratio. Chapter 5 also considers these factors, but using structurally different BOX ligands. The aziridination reaction is studied in Chapter 6, before summarising the findings and results in the conclusion in Chapter 7.

1.9 References

1   Van Leeuwen, P. W. N. M. *Homogeneous Catalysis: Understanding the Art*; Kluwer Academic Publishers, **2004**.

2   Atkins, P.; De Paulo, J. *Atkins' Physical Chemistry*; 8th ed.; Oxford University Press, **2006**.

3   Corey, E. J.; Imai, N.; Zhang, H. Y. *Journal of the American Chemical Society,* **1991**, *113*, 728.

4   Murphy, D. M.; Fallis, I. A.; Carter, E.; Willock, D. J.; Landon, J.; Van Doorslaer, S.; Vinck, E. *Physical Chemistry Chemical Physics,* **2009**, *11*, 6757.

5   Newman, C. G. *Clinics in perinatology,* **1986**, *13*, 555.

6   Caprio, V.; Williams, J. M. J. *Catalysis in Asymmetric Synthesis*; 2nd ed.; Wiley, **2009**.

7   Movassaghi, M.; Jacobsen, E. N. *Science,* **2002**, *298*, 1904.

8   Gladysz, J.; Michl, J. *Chemical Reviews,* **1992**, *92*, 739.

9   Aitken, R. A.; Kilenyi, S. N. *Asymmetric Synthesis*; Chapman & Hall: London, **1992**.

10   Koskinen, A. *Asymmetric Synthesis of Natural Products*; John Wiley & Sons: Chichester, **1993**.

11   Ojima, I. *Catalytic Asymmetric Synthesis*; 2nd ed.; Wiley-VCH, **2000**.

12   Noyori, R. *Asymmetric Catalysis in Organic Synthesis*; Wiley-Interscience: New York, **1994**.

13   Nogradi, M. *Stereoselective Synthesis*; Wiley-VCH: Weinheim, **1995**.

14   Gawley, R. E.; Aube, J. *Principles of Asymmetric Synthesis*; Pergamon: Oxford, **1996**; Vol. 14.

15   Jacobsen, E. N.; Pfaltz, A.; Yamamoto, H. *Comprehensive Asymmetric Catalysis*; Springer Verlag: New York, **1999**; Vol. 1-3.

16   Yoon, T. P.; Jacobsen, E. N. *Science,* **2003**, *299*, 1691.

17   Knowles, W. S. *Angewandte Chemie International Edition,* **2002**, *41*, 1998.

18   Kagan, H. B.; Dang Tuan, P. *Journal of the American Chemical Society,* **1972**, *94*, 6429.

19   Pfaltz, A. *Accounts of Chemical Research,* **1993**, *26*, 339.

20   Christmann, M.; Brase, S. *Asymmetric Synthesis - The Essentials*; 2nd ed.; Wiley-VCH Verlag GmbH & Co.: Weinheim, **2008**.

21   Lowenthal, R. E.; Abiko, A.; Masamune, S. *Tetrahedron Letters,* **1990**, *31*, 6005.

22   Evans, D. A.; Woerpel, K. A.; Hinman, M. M.; Faul, M. M. *Journal of the American Chemical Society,* **1991**, *113*, 726.

23   Rasappan, R.; Laventine, D.; Reiser, O. *Coordination Chemistry Reviews,* **2008**, *252*, 702.

24   McManus, H. A.; Guiry, P. J. *Chemical Reviews,* **2004**, *104*, 4151.

25   Desimoni, G.; Faita, G.; Jørgensen, K. A. *Chemical Reviews,* **2006**, *106*, 3561.

26   Ghosh, A. K.; Mathivanan, P.; Cappiello, J. *Tetrahedron: Asymmetry,* **1998**, *9*, 1.

27   Brunner, H.; Obermann, U.; Wimmer, P. *Journal of Organometallic Chemistry,* **1986**, *316*, 1.

28   Corey, E. J.; Ishihara, K. *Tetrahedron Letters,* **1992**, *33*, 6807.

29   Evans, D. A.; Woerpel, K. A.; Scott, M. J. *Angewandte Chemie International Edition in English,* **1992**, *31*, 430.

30   Von Matt, P.; Lloyd-Jones, G. C.; Minidis, A. B. E.; Pfaltz, A.; Macko, L.; Neuburger, M.; Zehnder, M.; Rüegger, H.; Pregosin, P. S. *Helvetica Chimica Acta,* **1995**, *78*, 265.

31   Lowenthal, R. E.; Masamune, S. *Tetrahedron Letters,* **1991**, *32*, 7373.

32   Desimoni, G.; Faita, G.; Mella, M. *Tetrahedron,* **1996**, *52*, 13649.

33   Davies, I. W.; Senanayake, C. H.; Larsen, R. D.; Verhoeven, T. R.; Reider, P. J. *Tetrahedron Letters,* **1996**, *37*, 813.

34   Ghosh, A. K.; Mathivanan, P.; Cappiello, J. *Tetrahedron Letters,* **1996**, *37*, 3815.

35   Davies, I. W.; Gerena, L.; Castonguay, L.; Senanayake, C. H.; Larsen, R. D.; Verhoeven, T. R.; Reider, P. J. *Chemical Communications,* **1996**, 1753.

36   Helmchen, G.; Krotz, A.; Ganz, K. T.; Hansen, D. *Synlett,* **1991**, 257.

37   Nishiyama, H.; Kondo, M.; Nakamura, T.; Itoh, K. *Organometallics,* **1991**, *10*, 500.

38   Nishiyama, H.; Sakaguchi, H.; Nakamura, T.; Horihata, M.; Kondo, M.; Itoh, K. *Organometallics,* **1989**, *8*, 846.

39   Nishiyama, H.; Yamaguchi, S.; Kondo, M.; Itoh, K. *The Journal of Organic Chemistry,* **1992**, *57*, 4306.

40   Nishiyama, H.; Yamaguchi, S.; Park, S. B.; Itoh, K. *Tetrahedron: Asymmetry,* **1993**, *4*, 143.

41   Nishiyama, H.; Park, S. B.; Itoh, K. *Tetrahedron: Asymmetry,* **1992**, *3*, 1029.

42   Walsh, P. J.; Kozlowsk, M. C. *Fundamentals of Asymmetric Catalysis*; Unversity Science Books, **2009**.

43 Frain, D.; Kirby, F.; McArdle, P.; O'Leary, P. *Tetrahedron Letters,* **2010**, *51*, 4103.

44 Gök, Y.; Noël, T.; Van der Eycken, J. *Tetrahedron: Asymmetry,* **2010**, *21*, 2275.

45 Jiang, F.; Wu, Z.; Yang, G.; Xie, F.; Zhang, W. *Tetrahedron Letters,* **2011**, *52*, 2844.

46 Dagorne, S.; Bellemin-Laponnaz, S.; Maisse-François, A. *European Journal of Inorganic Chemistry,* **2007**, 913.

47 Johnson, J. S.; Evans, D. A. *Accounts of Chemical Research,* **2000**, *33*, 325.

48 Irving, H.; Williams, R. J. P. *Journal of the Chemical Society,* **1953**, 3192.

49 Hathaway, B. J.; Billing, D. E. *Coordination Chemistry Reviews,* **1970**, *5*, 143.

50 Evans, D. A.; Miller, S. J.; Lectka, T.; Von Matt, P. *Journal of the American Chemical Society,* **1999**, *121*, 7559.

51 Aggarwal, V. K.; Jones, D. E.; Martin-Castro, A. M. *European Journal of Organic Chemistry,* **2000**, *2000*, 2939.

52 Atkins, P.; Overton, T.; Rourke, J.; Weller, M.; Armstrong, F. *Shriver & Atkins Inorganic Chemistry*; 4th ed.; Oxford University Press: Oxford, **2006**.

53 Nakamura, A.; Tsutsui, M. *Principles and Applications of Homogeneous Catalysis*; Wiley-Interscience, **1980**.

54 Masters, C. *Homogeneous Transition-metal Catalysis-a gentle art*; Chapman and Hall Ltd, **1981**.

55 Parshall, G. W. *Homogeneous Catalysis: The applications and chemistry of catalysis by soluble transition metal complexes*; John Wiley & Sons, Inc., **1980**.

56 Fraile, J. M.; García, J. I.; Mayoral, J. A. *Coordination Chemistry Reviews,* **2008**, *252*, 624.

57 Rechavi, D.; Lemaire, M. *Chemical Reviews,* **2002**, *102*, 3467.

58 Langham, C.; Piaggio, P.; McMorn, P.; Willock, D. J.; Hutchings, G. J.; Bethell, D.; Lee, D. F.; Bulman Page, P. C.; Sly, C.; Hancock, F. E.; King, F. *Chemical Communications,* **1998**, 1601.

59 Langham, C.; Bethell, D.; Lee, D. F.; McMorn, P.; Bulman Page, P. C.; Willock, D. J.; Sly, C.; Hancock, F. E.; King, F.; Hutchings, G. J. *Applied Catalysis A: General,* **1999**, *182*, 85.

60 Taylor, S.; Gullick, J.; McMorn, P.; Bethell, D.; Page, P. C. B.; Hancock, F. E.; King, F.; Hutchings, G. J. *Journal of the Chemical Society-Perkin Transactions 2,* **2001**, 1714.

61 Taylor, S.; Gullick, J.; McMorn, P.; Bethell, D.; Bulman Page, P. C.; Hancock, F. E.; King, F.; Hutchings, G. J. *Topics in Catalysis,* **2003**, *24*, 43.

62 Langham, C.; Taylor, S.; Bethell, D.; McMorn, P.; Bulman Page, P. C.; Willock, D. J.; Sly, C.; Hancock, F. E.; King, F.; Hutchings, G. J. *Journal of the Chemical Society, Perkin Transactions 2,* **1999**, 1043.

63 Alonso, P. J.; Fraile, J. M.; García, J.; García, J. I.; Martínez, J. I.; Mayoral, J. A.; Sánchez, M. C. *Langmuir,* **2000**, *16*, 5607.

64 Paluti, C. C.; Gawalt, E. S. *Journal of Catalysis,* **2010**, *275*, 149.

65 Framery, E.; Andrioletti, B.; Lemaire, M. *Tetrahedron: Asymmetry,* **2010**, *21*, 1110.

66 Tanaka, S.; Tada, M.; Iwasawa, Y. *Journal of Catalysis,* **2007**, *245*, 173.

67 Fakhfakh, F.; Baraket, L.; Ghorbel, A.; Fraile, J. M.; Herrerías, C. I.; Mayoral, J. A. *Journal of Molecular Catalysis A: Chemical,* **2010**, *329*, 21.

68 Rosario Torviso, M.; Blanco, M. N.; Cáceres, C. V.; Fraile, J. M.; Mayoral, J. A. *Journal of Catalysis,* **2010**, *275*, 70.

69 Evans, D. A.; Bilodeau, M. T.; Faul, M. M. *Journal of the American Chemical Society,* **1994**, *116*, 2742.

70 Evans, D. A.; Kozlowski, M. C.; Burgey, C. S.; MacMillan, D. W. C. *Journal of the American Chemical Society,* **1997**, *119*, 7893.

71 Evans, D. A.; Burgey, C. S.; Paras, N. A.; Vojkovsky, T.; Tregay, S. W. *Journal of the American Chemical Society,* **1998**, *120*, 5824.

72 Evans, D. A.; Miller, S. J.; Lectka, T. *Journal of the American Chemical Society,* **1993**, *115*, 6460.

73 Evans, D. A.; Murry, J. A.; Von Matt, P.; Norcross, R. D.; Miller, S. J. *Angewandte Chemie International Edition in English,* **1995**, *34*, 798.

74 Evans, D. A.; Kozlowski, M. C.; Tedrow, J. S. *Tetrahedron Letters,* **1996**, *37*, 7481.

75 Evans, D. A.; Johnson, J. S.; Burgey, C. S.; Campos, K. R. *Tetrahedron Letters,* **1999**, *40*, 2879.

76 Evans, D. A.; Barnes, D. M.; Johnson, J. S.; Lectka, T.; Von Matt, P.; Miller, S. J.; Murry, J. A.; Norcross, R. D.; Shaughnessy, E. A.; Campos, K. R. *Journal of the American Chemical Society,* **1999**, *121*, 7582.

77 Seki, C.; Hirama, M.; Hutabarat, N. D. M. R.; Takada, J.; Suttibut, C.; Takahashi, H.; Takaguchi, T.; Kohari, Y.; Nakano, H.; Uwai, K.; Takano, N.; Yasui, M.; Okuyama, Y.; Takeshita, M.; Matsuyama, H. *Tetrahedron,* **2012**, *68*, 1774.

78   Dentel, H.; Chataigner, I.; Lohier, J. F.; Gulea, M. *Tetrahedron,* **2012**, *68*, 2326.

79   Evans, D. A.; Faul, M. M.; Bilodeau, M. T.; Anderson, B. A.; Barnes, D. M. *Journal of the American Chemical Society,* **1993**, *115*, 5328.

80   Li, Z.; Conser, K. R.; Jacobsen, E. N. *Journal of the American Chemical Society,* **1993**, *115*, 5326.

81   Gullick, J.; Taylor, S.; Kerton, O.; McMorn, P.; King, F.; Hancock, F. E.; Bethell, D.; Bulman Page, P. C.; Hutchings, G. J. *Catalysis Letters,* **2001**, *75*, 151.

82   Pellissier, H. *Tetrahedron,* **2010**, *66*, 1509.

83   Aujla, P. S.; Baird, C. P.; Taylor, P. C.; Mauger, H.; Vallée, Y. *Tetrahedron Letters,* **1997**, *38*, 7453.

84   Södergren, M. J.; Alonso, D. A.; Andersson, P. G. *Tetrahedron: Asymmetry,* **1997**, *8*, 3563.

85   Gullick, J.; Taylor, S.; McMorn, P.; Bethell, D.; Bulman Page, P. C.; Hancock, F. E.; King, F.; Hutchings, G. *Journal of Molecular Catalysis A: Chemical,* **2002**, *180*, 85.

86   Gullick, J.; Taylor, S.; McMorn, P.; Bethell, D.; Bulman-Page, P. C.; Hancock, F. E.; King, F.; Hutchings, G. J. *Journal of Molecular Catalysis A: Chemical,* **2002**, *182-183*, 571.

87   Yamada, Y.; Yamamoto, T.; Okawara, M. *Chemistry Letters,* **1975**, 361.

88   Mohr, F.; Binfield, S. A.; Fettinger, J. C.; Vedernikov, A. N. *The Journal of Organic Chemistry,* **2005**, *70*, 4833.

89   Li, Z.; Quan, R. W.; Jacobsen, E. N. *Journal of the American Chemical Society,* **1995**, *117*, 5889.

90   Brandt, P.; Södergren, M. J.; Andersson, P. G.; Norrby, P. *Journal of the American Chemical Society,* **2000**, *122*, 8013.

91   Caplar, V.; Raza, Z.; Roje, M.; Tomisic, V.; Horvat, G.; Pozar, J.; Piantanida, I.; Zinic, M. *Tetrahedron,* **2004**, *60*, 8079.

92   Owen, M. E.; Carter, E.; Hutchings, G. J.; Ward, B. D.; Murphy, D. M. *Dalton Transactions,* **2012**, *41*, 11085.

Chapter 2

The theory of Electron Paramagnetic Resonance (EPR) and Electron Nuclear DOuble Resonance (ENDOR) spectroscopies

2.1 Introduction

Electron Paramagnetic Resonance (EPR) spectroscopy is used to study paramagnetism in solids, liquids and gases. EPR describes the resonant absorption of microwave radiation by a paramagnetic sample in a static magnetic field.[1] This chapter will firstly focus on the background, the fundamental theory and the practicalities of Continuous Wave (CW-) EPR, before considering the hyperfine technique of Continuous Wave Electron Nuclear DOuble Resonance (CW-ENDOR). An ENDOR investigation involves the detection of NMR resonances *via* the intensity changes of a simultaneously irradiated EPR line.[2] The basic principles of CW-ENDOR are described, followed by the theory of orientation selective ENDOR for structure determination in frozen solutions and powders.

CW-EPR is an extremely useful tool in catalytic chemistry due to the high sensitivity of the technique, which enables the detection of low concentrations of paramagnetic species. Many important homogeneous asymmetric catalysts are based on paramagnetic transition metal complexes such as Cr(III), Mn(II), Fe(III), Co(II) and Cu(II), and therefore these catalysts can be effectively studied using EPR/ENDOR spectroscopy. An understanding of the composition, structure and bonding of the active site throughout the catalytic cycle can be achieved.[3] Additionally, the paramagnetic reaction intermediates can sometimes be isolated and identified.[3] The *g* factor, central metal hyperfine and zero field splitting for high spin systems can be obtained using CW-EPR.[4] ENDOR is important in providing structural information from the powder EPR spectra of metal complexes, through the electron nuclear hyperfine interaction tensor.[2] Despite this, relatively few studies have fully exploited CW-EPR/ENDOR in their investigations of paramagnetic transition metal ions in homogeneous catalysis. Some examples of previous EPR studies of copper-bis(oxazoline) catalysts were presented in Chapter 1 (Section 1.7).

This chapter will deal with the fundamentals of CW-EPR and CW-ENDOR theory by focusing on the paramagnetic d^9 Cu(II) complexes.

2.2 Fundamentals of CW-EPR spectroscopy

2.2.1 Historical perspective

The EPR technique originates from the Stern-Gerlach[5] experiment which showed that the magnetic moment of an electron in a spherical atom can take only discrete orientations in a magnetic field.[4] Following this, Uhlenbeck and Goudsmit[6] related the electron magnetic moment with the concept of electron spin angular momentum.[4] An EPR signal was first recorded in 1945 by Zavoisky,[7] who detected a radiofrequency absorption line from a $CuCl_2.2H_2O$ sample. Today, EPR experiments are carried out using a wide range of frequencies and magnetic field strengths. Microwave frequencies are classed in bands and in EPR the most common of these is the X-band frequency.[8] The X-band frequency and other nominal microwave frequencies, and their corresponding resonance fields for $g = 2$, are listed in Table 2.1.

Table 2.1 Microwave frequencies and their corresponding resonance fields.[9]

Band	v / GHz	λ / cm	B (electron) / Gauss
L	1.1	27	390
S	3.0	10	1070
X	9.5	3.2	3400
K	24	1.2	8600
Q	35	0.85	12500
W	360	0.31	34000

In an EPR spectrum, the absorption of microwave frequency radiation is plotted against the magnetic field intensity.[8] The traditional method for recording an EPR spectrum is the continuous wave (CW) method, in which low intensity microwave radiation continuously irradiates the sample.[8] Alternatively, pulsed EPR involves the application of short pulses of high power microwave radiation to the sample.[4] Here, the response is recorded in the absence of radiation.[8] EPR spectroscopy can only be used for systems with net electron spin angular momentum.[4] However, there are many such systems, for example, free radicals in the solid, liquid or gaseous states, some point defects (localised crystal imperfections) in solids, biradicals, systems in the triplet state (two unpaired electrons), systems with three or more unpaired electrons and most transition metal ions and rare-earth ions.[4]

2.2.2 The electron spin and the electron Zeeman interaction

Electrons are characterised by an intrinsic angular momentum (spin), which is dependent on the magnitude and direction in space. There are two possible states for the

electron spin, labelled α and β.[8] In a free electron, the orientation of the angular momentum in space is different in the α and β states, although the magnitude of the angular momentum is the same.[8] The spin vector, S (or S_x, S_y, S_z, along the x, y, z axes of a Cartesian frame) possesses units of $\hbar$. The modulus of S is given by:

$$|S| = \sqrt{S(S+1)} \qquad [2.1]$$

where $S = 1/2$ is the electron spin quantum number and $|S| = \sqrt{(3/4)}$. α and β electron spin states are thought of as those with definite components of S_z, which is in $\hbar$ units of either +1/2 (α state) or -1/2 (β state). These spin states are said to be *degenerate* in the absence of a magnetic field, when both the α and β states have the same energy.[8]

In the presence of a magnetic field, the electron spin energy level is split into two states.[8] This is known as the *Zeeman effect*. The interaction of an electron magnetic moment with an applied magnetic field is described as the electron *Zeeman interaction*.[8] Due to its magnetic moment (μ_S), the electron behaves like a bar magnet when placed in a magnetic field, B_0. The state of lowest energy will occur when μ_S is aligned with the magnetic field, and the state of highest energy when μ_S is aligned against the magnetic field.[10] These two states are labelled by the direction of the electron spin, M_s, with respect to the direction of the magnetic field.[10] The parallel state is known as $M_s = -1/2$ and the antiparallel state is $M_s = +1/2$. The *Zeeman effect,* and the corresponding microwave absorption, is represented graphically in Figure 2.1. The equation for the electron Zeeman Hamiltonian (in the absence of any hyperfine interaction) takes the form

$$H = \mu_B \bullet B \bullet g \bullet S \qquad [2.2]$$

where S is the vector operator of the electron spin and g is the g-tensor. The energy difference between the electron Zeeman levels can be written as

$$\Delta E = h\nu = g_e \mu_B B \qquad [2.3]$$

where g is a number called the Landé factor or g factor. $g_e = 2.002319$ for a free electron, $h = 6.624 \times 10^{-34}$ Js is Planck's constant and μ_B is the atomic unit of the magnetic moment, the *Bohr magneton* (9.27410^{-24} JT^{-1}).
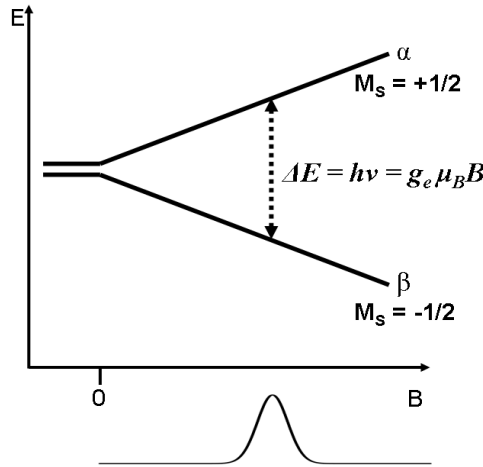
Figure 2.1 Illustration of the electron Zeeman effect and the corresponding absorption of microwaves.

The magnetic moment μ_S is proportional to the electron spin angular momentum, S, and these vectors are parallel to each other.[8] Their directions are opposite since the proportionality constant is negative. The relationship between μ_S and S can be expressed as follows:

$$\mu_S = -g\mu_B S \qquad [2.4]$$

2.2.3 The nuclear Zeeman interaction and the hyperfine interactions

Nulei can also be characterised by a spin angular momentum (I).[8] This relates to the nuclear magnetic moment, μ_N, as such:

$$\mu_N = g_n \mu_n I \qquad [2.5]$$

where g_n is the nuclear g-factor and μ_n is the nuclear magneton (5.05×10^{-27} JT^{-1}).

The magnitude and z component of the nuclear spin (in units of $\hbar$) is given as follows:

$$|I| = \sqrt{I(I+1)} \qquad [2.6]$$

and

$$I_Z = -I, -I + 1, \dots , I \qquad [2.7]$$

The energy of nuclear spins, E, is affected by the presence of a magnetic field due to the nuclear spin angular momentum component along the direction of magnetic field I_Z.[8] This is known as the *nuclear Zeeman effect:*

$$E = -g_n \mu_n B_0 I_Z \qquad [2.8]$$

where B_0 is the magnetic field intensity.

An additional magnetic field from the nuclear magnetic moment is experienced in the presence of a nuclear spin.[8] This is the *hyperfine interaction*, and results in a splitting of the resonance EPR lines into numerous components.[8] The general rule for

this splitting is that $2nI + 1$ components will be seen for the interaction with a spin I nucleus. ^{63}Cu and ^{65}Cu have a nuclear spin of 3/2. This leads to four EPR signals for each isotope, as predicted by the rule $2nI + 1$.

2.2.4 The spin Hamiltonian

Considering the simplest two spin system ($S = 1/2$, $I = 1/2$) in an external magnetic field, the spin Hamiltonian (H) is given as:

$$H = H_{EZ} + H_{NZ} + H_{HFS} \tag{2.9}$$

where EZ = electron Zeeman term, NZ = nuclear Zeeman term, and HFS = hyperfine interaction. This equation can then be written as:

$$H = \mu_B B_0 \cdot g \cdot S - g_n \mu_n B_0 \cdot I + h S \cdot A \cdot I \tag{2.10}$$

where S and I are the vector operators of the electron and nuclear spins, and g and A are the g- and hyperfine coupling tensors.[2] Assuming that only isotropic interactions are present in the system, and that the external magnetic field is aligned along the z axis, H is given as:

$$H = g\mu_B B_0 S_Z - g_n \mu_n B_0 I_Z + ha S \cdot I \tag{2.11}$$

where g is now the dimensionless isotropic g-factor and a is the isotropic hyperfine coupling constant in hertz (Hz). In the high field approximation and excluding second order terms, the energy levels for the two spin system ($S = 1/2$, $I = 1/2$) is described as:

$$E(M_S, M_I) = g\mu_B B_0 M_S - g_n \mu_n B_0 M_I + ha M_S M_I \tag{2.12}$$

where M_S and M_I are the magnetic spin quantum numbers with values of $\pm 1/2$. This equation can be simplified as follows:

$$E(M_S, M_I)/h = \nu_e M_S - \nu_n M_I + a M_S M_I \tag{2.13}$$

where $\nu_e = g\mu_B B_0/h$ and $\nu_n = g_n \mu_n B_0/h$. Four possible energy levels result from this equation (labelled $E_a - E_d$), which can be defined as:

$$E_a = -\tfrac{1}{2} g\mu_B B_0 - \tfrac{1}{2} g_n\mu_n B_0 - \tfrac{1}{4}ha \tag{2.14}$$

$$E_b = +\tfrac{1}{2} g\mu_B B_0 - \tfrac{1}{2} g_n\mu_n B_0 + \tfrac{1}{4}ha \tag{2.15}$$

$$E_c = +\tfrac{1}{2} g\mu_B B_0 + \tfrac{1}{2} g_n\mu_n B_0 - \tfrac{1}{4}ha \tag{2.16}$$

$$E_d = -\tfrac{1}{2} g\mu_B B_0 + \tfrac{1}{2} g_n\mu_n B_0 + \tfrac{1}{4}ha \tag{2.17}$$

Considering the EPR selection rules, ($\Delta M_S = \pm 1$ and $\Delta M_I = 0$), it can be deduced that there are two possible resonance transitions. These are ΔE_{cd} (labelled EPR 1) and ΔE_{ab} (labelled EPR 2):

$$\Delta E_{cd} = E_c - E_d = g\mu_B B - \tfrac{1}{2}ha \tag{2.18}$$

$$\Delta E_{ab} = E_b - E_a = g\mu_B B + \tfrac{1}{2}ha \tag{2.19}$$

Two absorption peaks at different magnetic field positions arise from the EPR 1 and EPR 2 transitions. These peaks are separated by a, which is the isotropic hyperfine splitting.[2] This is shown in Figure 2.2a, where two EPR transitions are evident. This differs from Figure 2.2b, which represents a system where an unpaired electron, $S = 1/2$, is interacting with a Cu(II) nucleus, $I = 3/2$. Here, four EPR transitions are evident, resulting in four absorption peaks and hence four EPR signals, as explained in Section 2.2.3.
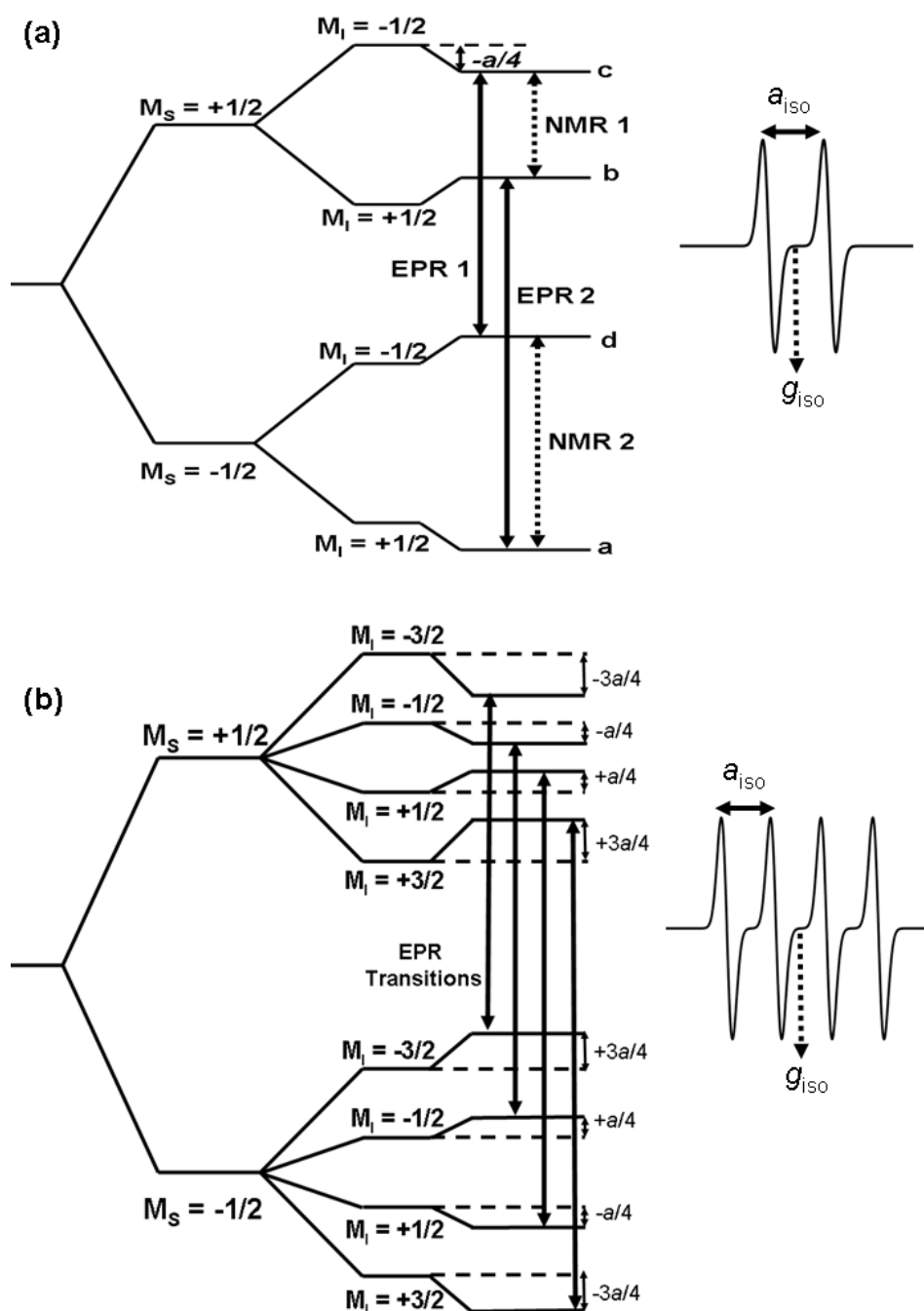
Figure 2.2 Energy level diagrams for a system with one electron, $S = 1/2$, interacting with (a) a proton ($I = 1/2$), and (b) a copper(II) nucleus ($I = 3/2$). Their corresponding isotropic EPR spectra are shown on the right.

*2.2.5 The **g**-matrix*

For a free electron, the *g*-value is a scalar quantity which has a value of g_e = 2.0023. A mixture of orbital angular momentum into the spin ground state (through spin-orbit coupling), results in a deviation from g_e. The components of the **g**-matrix therefore incorporate *p*-, *d*-, or *f*- orbital character, unlike g_e.[9] Therefore, in copper(II) complexes, the *g*-factors are shifted from the free-electron value of 2.0023 due to spin-orbit coupling of the $3d^9$ ground state to appropriate excited states.[1] The real components of the **g**-matrix are then given by:

$$g_{ij} = g_e\delta_{ij} + 2 \sum_k \sum_{m \neq 0} \frac{\zeta_k <m|l_{ki}|0> <0|l_{kj}|m>}{E_0 - E_m}$$ [2.20]

where the indices *i* and *j* refer to molecular coordinate axes (*x, y, z*), *k* denotes the atoms with unpaired electron density, *m* denotes the filled and empty molecular orbitals (MOs) with energy E_m (E_0 is the energy of the SOMO), ζ_k is the spin-orbit coupling constant for atom *k*, and l_{ki} is the *i*-component of the orbital angular momentum operator for atom *k*. The integrals $<m|l_{ki}|0>$ are easily computed for an electron centred on a single atom if the MOs are written as linear combinations of real *p* or *d* atomic orbitals.[9]

As a result of the orbital contribution to g_e in real systems, and particularly in frozen solution, an anisotropic **g** tensor is observed. Upon freezing the solution, the orientation of the paramagnetic species become immobilised in a disordered orientation in the magnetic field.[8]

A paramagnet is described as isotropic when $g_{11} = g_{22} = g_{33}$.[11] This is extremely rare for *d* transition metal complexes as this would only occur for perfectly cubic, octahedral or tetrahedral symmetries.[11] However, isotropic spectra are commonly observed for *d* transition metal complexes in liquid solutions. The anisotropic molecule must be tumbling quickly enough to average any anisotropy.[11] When this happens g_{iso} can be expressed as:

$$g_{iso} = 1/3 \, (g_{11} + g_{22} + g_{33})$$ [2.21]

An example of an isotropic Cu(II) EPR spectrum is shown in Figure 2.3b.

If two of the principal *g* values of a paramagnetic form are equal, the *g* values are said to be axial.[11] The unique *g* value is usually referred to as $g_\parallel$ (corresponding to g_{33} for example), whilst the other value is referred to as $g_\perp$ (=$g_{11} = g_{22}$).[11] An axial Cu(II) spectrum showing four signals in the parallel region, and four in the perpendicular region, is shown in Figure 2.3a.
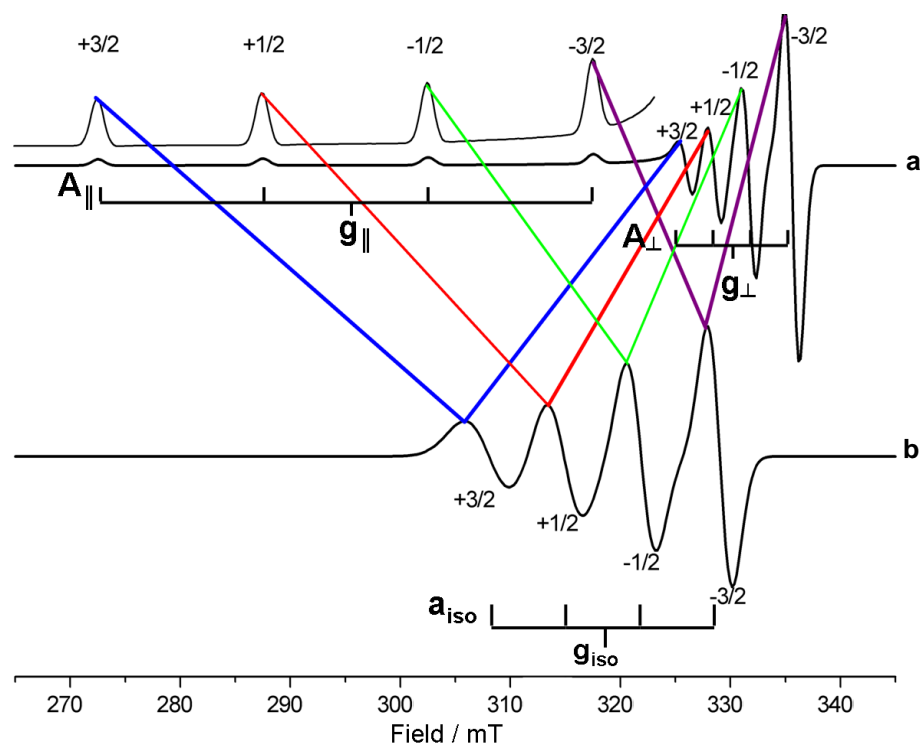
Figure 2.3 *X*-band EPR spectra for a Cu(II) system, showing (a) axial symmetry and (b) isotropic symmetry.

When all three *g* values are inequivalent, $g_{11} \neq g_{22} \neq g_{33}$, the symmetry of the paramagnet is described as rhombic.[11] Other possible symmetries include monoclinic, triclinic and axial non-collinear. Table 2.2 summarises the range of different symmetries and their corresponding properties.[12]

Table 2.2 Classification of EPR symmetry elements in relation to *g* and *A* tensors, the coincidence of tensor axes and the point symmetry of the paramagnetic species.[12]

EPR Symmetry	g and A Tensors	Coincidence of Tensor Axes	Molecular Point Symmetry
Isotropic	$g_{xx} = g_{yy} = g_{zz}$ $A_{xx} = A_{yy} = A_{zz}$	All coincident	O_h, T_d, O, T_h, T
Axial	$g_{xx} = g_{yy} \neq g_{zz}$ $A_{xx} = A_{yy} \neq A_{zz}$	All coincident	$D_{4h}, C_{4v}, D_4. D_{2d},$ $D_{6h}, C_{6v}, D_6, D_{3h},$ D_{3d}, C_{3v}, D_3
Rhombic	$g_{xx} \neq g_{yy} \neq g_{zz}$ $A_{xx} \neq A_{yy} \neq A_{zz}$	All coincident	D_{2h}, C_{2v}, D_2
Monoclinic	$g_{xx} \neq g_{yy} \neq g_{zz}$ $A_{xx} \neq A_{yy} \neq A_{zz}$	One axis of g and A coincident	C_{2h}, C_s, C_2
Triclinic	$g_{xx} \neq g_{yy} \neq g_{zz}$ $A_{xx} \neq A_{yy} \neq A_{zz}$	Complete non-coincidence	C_1
Axial non-collinear	$g_{xx} = g_{yy} \neq g_{zz}$ $A_{xx} = A_{yy} \neq A_{zz}$	Only g_{zz} and A_{zz} coincident	$C_3, S_6, C_4, S_4, C_{4h},$ C_6, C_{3h}, C_{6h}

Representing the **g**-tensor as a 3 x 3 matrix can simplify the understanding of these symmetry groups.[8] The Zeeman Hamiltonian in Equation [2.2] can be written in matrix form as:

$$H = \mu_B \begin{pmatrix} S_x \\ S_y \\ S_z \end{pmatrix} \bullet \begin{pmatrix} g_1 & 0 & 0 \\ 0 & g_2 & 0 \\ 0 & 0 & g_3 \end{pmatrix} \bullet \begin{pmatrix} B_0^x \\ B_0^y \\ B_0^z \end{pmatrix} \qquad [2.22]$$

It is often assumed that one set of principal axes diagonalises all the relative matrices, but in truth, these principal axes can be *non-coincident*, as stated in Table 2.2. These low-symmetry effects can be seen in transition metal ions in sites of monoclinic or triclinic symmetry.[1,13] The observable effects of non-coincidence matrix axes on powder EPR patterns range from very obvious to barely visible, and are generally more noticeable if two or more matrices have large anisotropies that are comparable in magnitude. A simplified illustration of non-coincidence is shown in Figure 2.4.
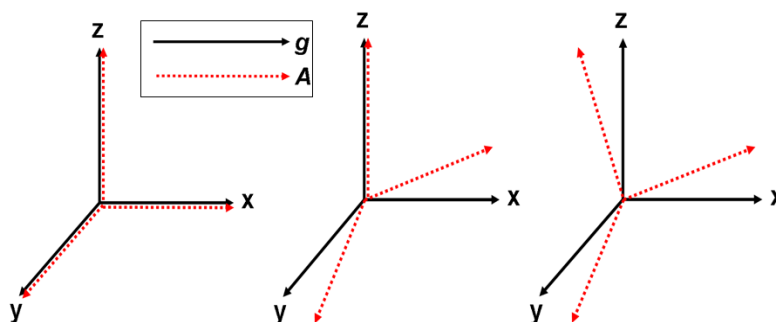
Figure 2.4 Illustration of coincidence in the *g* / *A* frame: (a) all coincident, (b) one axis of *g* and *A* coincident, and (c) complete non-coincidence.

An effect known as *g-strain* should also be considered during the analysis of EPR spectra for Cu(II) systems. Until this point of the discussion, it has been assumed that each spin Hamiltonian parameter has a discrete value which applies to each paramagnetic site within the sample.[11] However, it is possible for the surroundings of the paramagnetic ion have a degree of flexibility. Slight changes in geometry can therefore arise, despite the chemical identity of each paramagnetic site being the same.[11] This results in small differences in the *g*-values of individual sites within the sample.[11] As shown in Figure 2.3a, four lines are seen in the parallel region of the Cu(II) EPR spectra. The *g*-strain effect results in a broadening effect, *i.e.*, increasing the widths and decreasing the intensities of the parallel hyperfine components at higher field positions.[11,14] This broadening effect is usually more prominent at higher microwave frequency due to the increased shift of the resonance fields, for example at *Q*-band compared with *X*-band.[11]

2.2.6 Superhyperfine splitting

In d transition metal compounds, the ligand derived hyperfine (superhyperfine) interaction, is usually smaller than the metal hyperfine interaction.[12] When Cu(II) is ligated to nuclei with $I > 0$, superhyperfine splitting can sometimes be observed.[15] This is due to the magnetic interaction of the unpaired electron spin with the nuclear magnetic moment. Examples of copper complexes in which the central copper atom is ligated to nuclei with $I > 0$ include copper-salen complexes and copper-phthalocyanine complexes. Murphy *et al.*,[16,17] have used EPR and ENDOR to investigate copper-salen complexes, which have two nitrogens and two oxygens coordinated to the metal centre. Van Doorslaer *et al.,*[18] have used similar techniques to study copper-phthalocyanine complexes, in which the copper is coordinated to four nitrogen atoms.

In the case of ^{14}N interacting nuclei ($I = 1$), each Cu(II) absorption is further split into a triplet pattern with intensities of 1:1:1. For two equivalent nitrogens, as in the BOX ligand, the superhyperfine patterns will consist of features having intensities in the ratio of 1:2:3:2:1. In summary, the number of EPR lines for n equivalent nuclei is given by $2nI + 1$, with the multiplicities for each line corresponding to the coefficients of the binomial expression, often recalled by using Pascal's Triangle. For non-equivalent ligands, the patterns become extremely complex.[15]

Simulated examples of Cu(II) spectra with one ligated nitrogen, and with two equivalent ligated nitrogens, are shown in Figures 2.5a and 2.5b respectively. Only the predominant isotope of copper, ^{63}Cu, has been included in these simulations; ^{65}Cu has been omitted for clarity. Due to the difference of around 7% in the nuclear magnetic moments of ^{63}Cu and ^{65}Cu, the presence of both isotopes results in a broadening of the lines due to the larger hyperfine splitting of ^{65}Cu as a result of its larger g_n.[1]
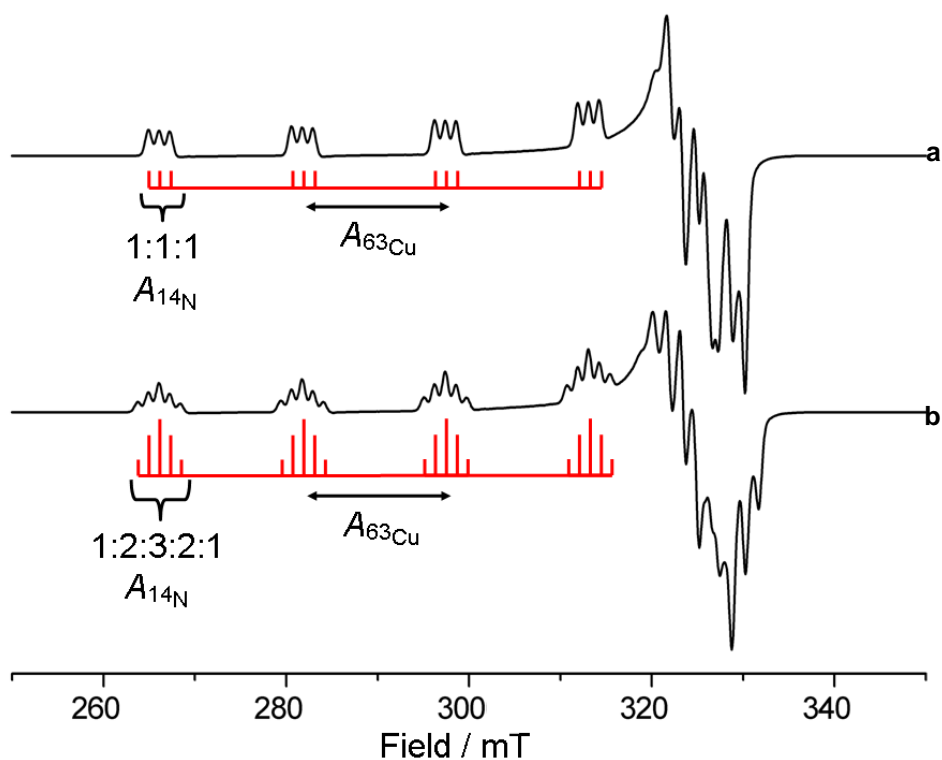
Figure 2.5 Simulated *X*-band EPR of a hypothetical square planar Cu(II) complex interacting with (a) one equivalent nitrogen nucleus and (b) two equivalent nitrogen nuclei.

It is evident from Figure 2.5 that the perpendicular region is extremely complex, and can be difficult to analyse due to the close proximity and overlapping nature of the peaks. The parallel region however is more distinguishable, and therefore easier to analyse. The clarity of the parallel region has led to trends in the hyperfine values being determined, and for copper complexes these trends have been summarised in graphs known as the *Peisach-Blumberg Plots*, an example of which is shown in Figure 2.6.[15]

These empirical plots of $g_\parallel$ versus $A_\parallel$ classify the EPR properties of copper complexes.[15] They are very useful to distinguish different types of planar coordination, for example bearing four nitrogens, four oxygens, four sulphurs, and combinations of these. It must be noted that these plots are most reliable in the simplest cases, where all the ligated atoms are the same.[15] In Figure 2.6, the upper left sections of each region correspond to more negatively charged ML_4 complexes, whilst the lower right-hand are from the more positively charged complexes.[1] Small deviations from square planar coordination will result in a reduction in $A_\parallel$ whilst large deviations will also shift $g_\parallel$ to smaller values.[15] In the case of [Cu(BOX)] complexes these plots can in principle be used to aid the distinction between heteroleptic [Cu(BOX)](OTf)$_2$ (2N2O) complexes and homoleptic [Cu(BOX)$_2$] (4N) complexes. From the plot, it can be deduced that

2N2O complexes such as [Cu(BOX)](OTf)$_2$, generally have higher $g_\parallel$ values and lower $A_\parallel$ values compared to 4N complexes such as [Cu(BOX)$_2$].
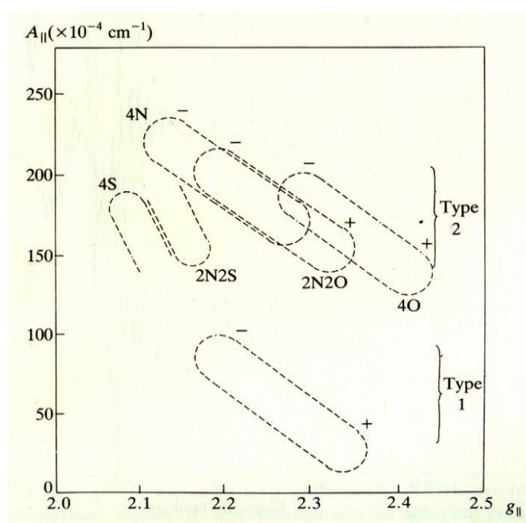
Figure 2.6 The Peisach-Blumberg Plot.[1,15]

2.2.7 Comparison of X- and Q-band frequencies

As previously stated in Section 2.2.1, *X*-band (9.5 GHz) is the most commonly used frequency in EPR spectroscopy. It is however important to acknowledge some of the advantages of recording the EPR spectra at higher frequencies, for example *Q*-band (35 GHz). Considering Equation [2.3], it can be readily deduced that the energy differences between the electron Zeeman levels at higher frequency is larger. *Q*-band frequency therefore results in better resolution of *g*-values. This provides a more detailed understanding of the symmetry of the system with low *g* anisotropy, since some systems that appear axial at lower frequencies (*e.g., X*-band) are actually of lower symmetry.[11] *Q*-band frequency can also make it easier to measure the metal hyperfine splitting because of the reduction of second order effects such as ligand superhyperfine splitting.[11] Another advantage of *Q*-band frequency is the improvement of resolution of metal quadrupolar effects, which are discussed in Section 2.3.6. Figure 2.7 shows a comparison of Cu(II) EPR spectra simulated at (a) *X*-band and (b) *Q*-band, but using the same *g* axis scale (as opposed to the more common field axis scale) to highlight the enhancement in *g*-resolution.
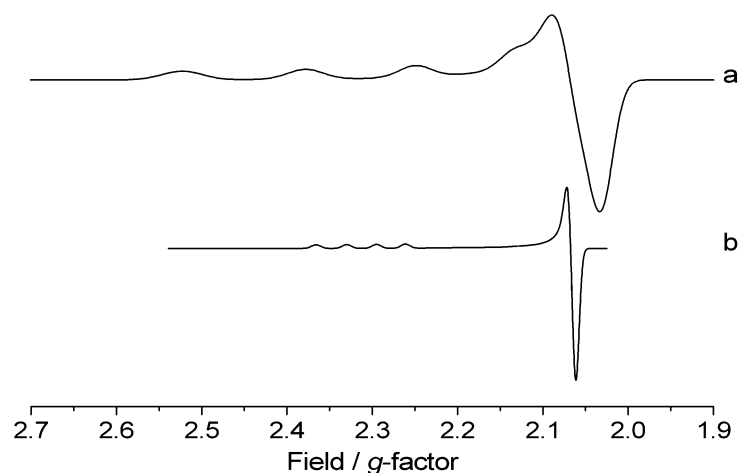
Figure 2.7 Comparison of simulated Cu(II) powder EPR spectra at (a) *X*-band and (b) *Q*-band frequency.

2.2.8 The physical state of the sample

EPR spectroscopy of *d*-transition metal complexes is usually performed as a fluid or frozen solution, a powdered solid or a single crystal.[11] For [Cu(BOX)] samples, recording the sample as a frozen solution is the most suitable method to obtain a magnetically dilute sample. Samples are therefore often recorded at low temperature (~140 K). The purpose of freezing the solution is to ensure that a random collection of paramagnets is obtained. Solvents must form a glass when frozen to avoid the formation of crystallites.[12] A bad glass can often be overcome by using a mixed solvent system; examples of common solvent systems which tend to give a good glass are toluene/dichloromethane, methanol/acetonitrile, ethanol/dimethylsulphoxide.[11] For the [Cu(BOX)] samples synthesised in this work, it was generally found that tetrahydrofuran/dichloromethane formed a good glass with good superhyperfine resolution whilst at the same time giving the best solubility of the complex. The randomness of the paramagnets can be checked by rotating the sample tube in the cavity; if the two spectra are not identical the paramagnets do not have a completely random orientation.[12]

2.3 Fundamentals of CW-ENDOR spectroscopy

2.3.1 Basic principles of ENDOR

ENDOR is a double resonance experiment that can be described as a combination of EPR and NMR spectroscopy. As it is a double resonance technique, two irradiating fields excite different transitions simultaneously; that is both the electron and nuclear spin transitions are excited.[2] This section deals with the fundamentals of this technique.

2.3.2 Spin populations

In an ENDOR experiment, NMR transitions are observed indirectly through the changes in microwave absorption of a simultaneously irradiated EPR transition.[2] In order to understand this, the population difference between the four energy levels of a simplified two spin system ($S = 1/2$, $I = 1/2$) must be considered. As previously described, there are four energy levels and two EPR transitions (EPR 1 and EPR 2) in the case of a simplified two spin system (Figure 2.2a). For the NMR transitions, the NMR selection rules ($\Delta M_S = 0$ and $\Delta M_I = \pm 1$) can be applied. Two NMR transitions are therefore possible:

$$\text{NMR 1: } \Delta E_{bc} = E_b - E_c = g\mu_n B - \tfrac{1}{2}ha \qquad [2.23]$$

$$\text{NMR 2: } \Delta E_{ad} = E_d - E_a = g\mu_n B + \tfrac{1}{2}ha \qquad [2.24]$$

The Boltzmann Law describes the relative populations of the four hyperfine levels (labelled **a**, **b**, **c** and **d** in Figure 2.2a). At temperatures above a few Kelvin, the electronic Boltzmann factor can be written as:

$$N_\alpha / N_\beta = \exp\left(-g\mu_B B_0 / kT\right) = 1 - g\mu_B B_0 / kT \qquad [2.25]$$

where k is the Boltzmann constant (1.3806×10^{-23} JK^{-1}) and T is the absolute temperature of the lattice. The differences between the nuclear spin levels (**c,b** and **d,a**) are so small that they can be ignored; these differences are of the order of $g_n\mu_n B_0/kT$, which is approximately only 10^{-3} of the population difference between the electronic levels. With ε denoting $g\mu_B B_0/kT$, the initial population difference between the upper and lower levels is illustrated in Figure 2.8. A slight excess in the lower level is represented as $1+\varepsilon$, whilst a slight depletion in the upper level is defined as $1-\varepsilon$.
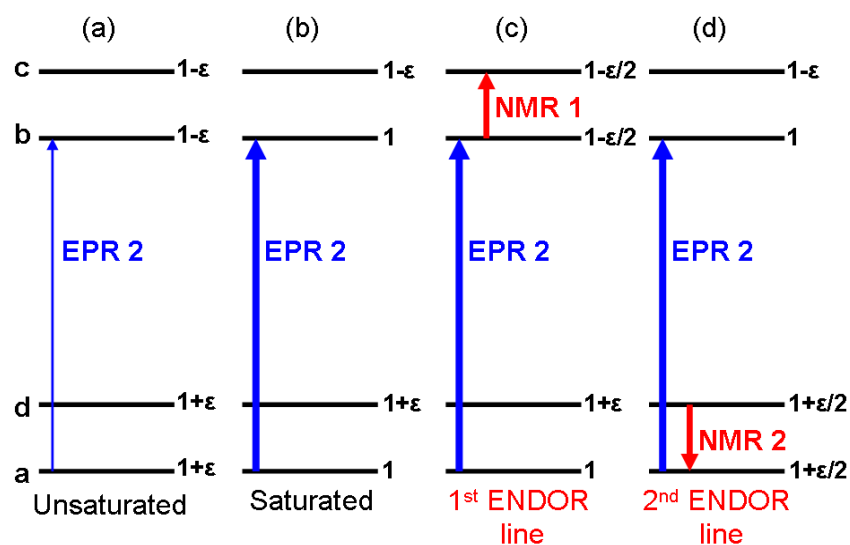
Figure 2.8 Four level energy diagram for a two spin system ($S = \frac{1}{2}$ and $I = \frac{1}{2}$). The four levels **a**, **b**, **c** and **d** correspond to the same energy levels as represented in Figure 2.2a.[2]

The thermal populations in the Zeeman levels **a** and **b** are almost equal, as long as the EPR transition **a→b** is induced with sufficiently low microwave (*mw*) power (Figure 2.8a).[2] Here, the induced transition rate **a→b** cannot compete with the efficient spin-lattice relaxation, and so the 'hot spins' return from **b→a**.

If the *mw* field is strong enough (Figure 2.8b), the induced absorption rate is able to compete with the electronic spin relaxation rate. Saturation of the levels **a** and **b** occurs and the population levels will therefore equalise.[2]

The application of a nuclear radiofrequency (*rf*) between levels **b** and **c** desaturates the EPR signal (*i.e.*, the population difference is restored between **a** and **b**) *via* induced absorption. This equalises the populations of levels **b** and **c** (Figure 2.8c), and leads to an overall increase in the inequality in the populations of the two energy levels corresponding to the EPR transition (**a** and **b**). This increases the EPR signal intensity and produces an ENDOR response. The observation of the first ENDOR line therefore corresponds to the NMR 1 frequency.[2]

The subsequent application of *rf* power between levels **a** and **d** results in the desaturation of the EPR signal by induced emission, giving a second EPR signal which corresponds to the NMR 2 frequency (Figure 2.8d). The partial desaturation of the EPR signal by the *rf* field can be considered as a decrease in the effective spin lattice relaxation time, which is generally characteristic of the ENDOR mechanism.[2]

To reiterate, the nuclear resonances in ENDOR are observed indirectly *via* their influence on the EPR line (known as a quantum transformation). In this simplified description of ENDOR (Figure 2.8), relaxation effects have been omitted. In reality, the presence of a saturating *mw* and *rf* field would result in the three energy levels **a**, **b** and **c** quickly becoming equally populated. The ENDOR signal would therefore disappear, producing a *transient* ENDOR response. In order to observe a continuous ENDOR response, there must be a complete relaxation pathway for the electron spins, parallel to the spin lattice pathway.[2] One such pathway shall now be discussed in Section 2.3.3.

2.3.3 The steady state ENDOR effect

In a simple, two spin system ($S = 1/2$, $I = 1/2$), there are several different types of relaxation pathways, illustrated in Figure 2.9.[2] The solid lines represent radiation induced transitions, whilst the dashed lines represent radiationless electron spin-lattice (W_e), nuclear spin-lattice (W_n) and cross relaxation processes (W_{x1} and W_{x2}). W_e and W_n are the inverse of the spin lattice relaxation $W_i = 1/T_1$. In the cross relaxation processes

(W_{x1} and W_{x2}), both electron and nuclear transitions occur simultaneously. This can be described as follows:

$$W_{x1} = \left| + - > \rightarrow \right| - + > \; (\text{'flip flop'} \text{ transition}) \qquad [2.26]$$

$$W_{x2} = \left| + + > \rightarrow \right| - - > \; (\text{'flop flop'} \text{ transition}) \qquad [2.27]$$

The EPR transition ($\nu_{\text{EPR 1}}$) is irradiated with *mw* radiation of sufficient power to prevent the spin lattice radiation rate W_{e1} from competing with the induced transition. As the Boltzmann populations equalise the signal is partially saturated. From Figure 2.9, it is evident that W_{e1} is the most efficient route for electron relaxation from **c→d**.

An alternative pathway is **c→b→a→d**, known as the *bypass route*. This route is normally inefficient because the nuclear relaxation rates, W_{n1} and W_{n2}, are significantly smaller than W_{e1}, thus resulting in an accumulation of spins in levels **b** and **d**. However, it may be possible to overcome the 'bottleneck' caused by W_{n1} by pumping the transition **c→b** with a saturating *rf* field (of frequency $\nu_{\text{NMR 1}}$ which effectively short circuits W_{n1}). This results in an improvement in the efficiency of the bypass route and increases the effective spin lattice relaxation rate. The EPR transition is therefore desaturated, leading to a corresponding increase of the EPR signal intensity. This effect is known as the *steady state ENDOR effect*.[2]

The magnitude of the EPR response is dependent on the relative rates W_e, W_n, W_{x1} and W_{x2}. Neglecting W_{xi} (Equations [2.26] and [2.27]), optimum ENDOR signals are observed when $W_e = W_n$ since no relaxation bottleneck appears in the bypass route.[2]
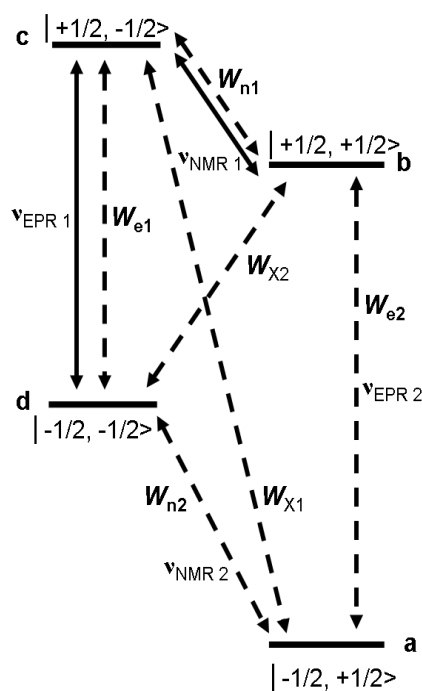
Figure 2.9 Four level energy diagram for a two spin system ($S = \frac{1}{2}$ and $I = \frac{1}{2}$). The four levels **a**, **b**, **c** and **d** correspond to the same energy levels as represented in Figure 2.2a. Solid lines = induced transitions; dashed lines = relaxation transitions.[2]

2.3.4 Orientation selective ENDOR

For transition metal Cu(II) complexes, such as $[Cu(II)(BOX)](OTf)_2$, an anisotropic EPR spectrum is obtained in frozen solution, see for example Figures 2.3, 2.5 and 2.7. All orientations of the paramagnetic species are observed; the spectrum is a superposition of resonances from randomly aligned molecules. This leads to complex ENDOR spectra, in which an in-depth understanding of the g and A anisotropy of the system is essential.[2]

For a uniaxial system, the EPR resonance is dependent on the orientation of the field position.[8] The g value will therefore vary with respect to the direction of the magnetic field. The first EPR peak will appear at the $B_\parallel$ field position and another will appear at $B\perp$. The orientation dependence with respect to the change in applied magnetic field direction for a uniaxial Cu(II) system is illustrated in the angular dependency plot, or *roadmap* shown in Figure 2.10.
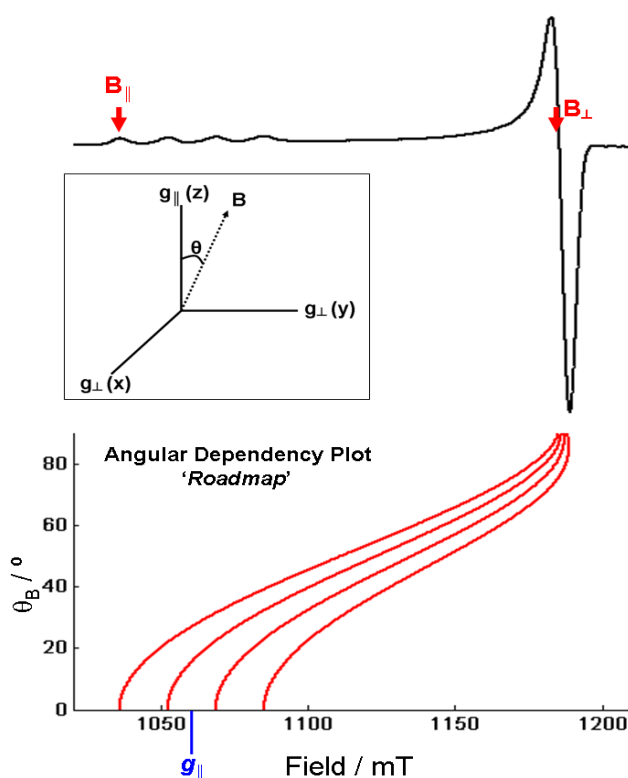
Figure 2.10 Simulated Q-band EPR spectrum of a $[Cu(BOX)](OTf)_2$ sample with the corresponding *roadmap*. A definition of the magnetic field direction (θ) for an axial paramagnet $(g_\parallel.g\perp)$ is shown in the subset.

Orientation selective ENDOR is the recording of ENDOR spectra at selected field positions in the EPR spectrum, yielding a single crystal-like spectrum from polycrystalline matrices, as explained by Hoffman[19] and Kreilick.[20,21] The main turning points are labelled with the red arrows in Figure 2.10; at these fixed magnetic field

positions, the resulting ENDOR signal comes only from the subset of molecules with orientations that contribute to the EPR intensity at that particular field. The orientation dependency of the *g* and *A* tensors is therefore of paramount importance, as the profile and shape of the ENDOR spectrum is dependent on the field position selected in the EPR spectrum.

The resulting ENDOR spectra are simulated at each different field position, using identical parameters. This provides information on the principal components of the hyperfine and quadrupole tensors as well as their orientation relative to *g*. The *g* tensor orientations contributing to the EPR resonance positions at the selected magnetic fields, *B*, must therefore be determined. The hyperfine tensor *A*, is then analysed to extract the isotropic (a_{iso}) and dipolar ($A_{dipolar}$) contributions. a_{iso} can be easily computed as the average of A_1, A_2 and A_3, and this provides an insight into the electronic structure or *s*-orbital contribution to the SOMO of the paramagnetic compound. $A_{dipolar}$ can be described as the direct coupling between the unpaired electron and the nuclei through space. This is used to calculate the distance to the interacting nucleus using the simple point-dipole approximation, which will be explained in Section 2.3.5.

To illustrate the orientation selectivity of the technique, model simulated spectra for an axially symmetric two-spin ($S = 1/2$, $I = 1/2$) system will be considered. The variation in resonance field position as a function of the angle θ between *B* and the unique axis of the *g* tensor is determined *via* a roadmap, as described above.

To begin with, a hypothetical coupling of $A_1 = A_2 = A\perp = 5$ MHz and $A_3 = A\parallel = 10$ MHz is described. The magnetic field is swept, altering the position of the external magnetic field position (θ_B). The position of the proton remains constant ($\theta_H = 0°$, *i.e.*, A_3 is aligned along the *z* axis of the *g* tensor and the field vector; see Figure 2.11). Only the largest ($A_3 = A\parallel = 10$ MHz) coupling is observed when $\theta_B = 0°$. At $\theta_B = 90°$, all orientations perpendicular to the *z* axis are included. Since $A_1 = A_2 = A\perp = 5$ MHz, two peaks separated by 5 MHz are observed. At all other field positions, contributions from all principal axes of the nuclear tensor are observed. In this example, only one resonance is observed at all field positions.
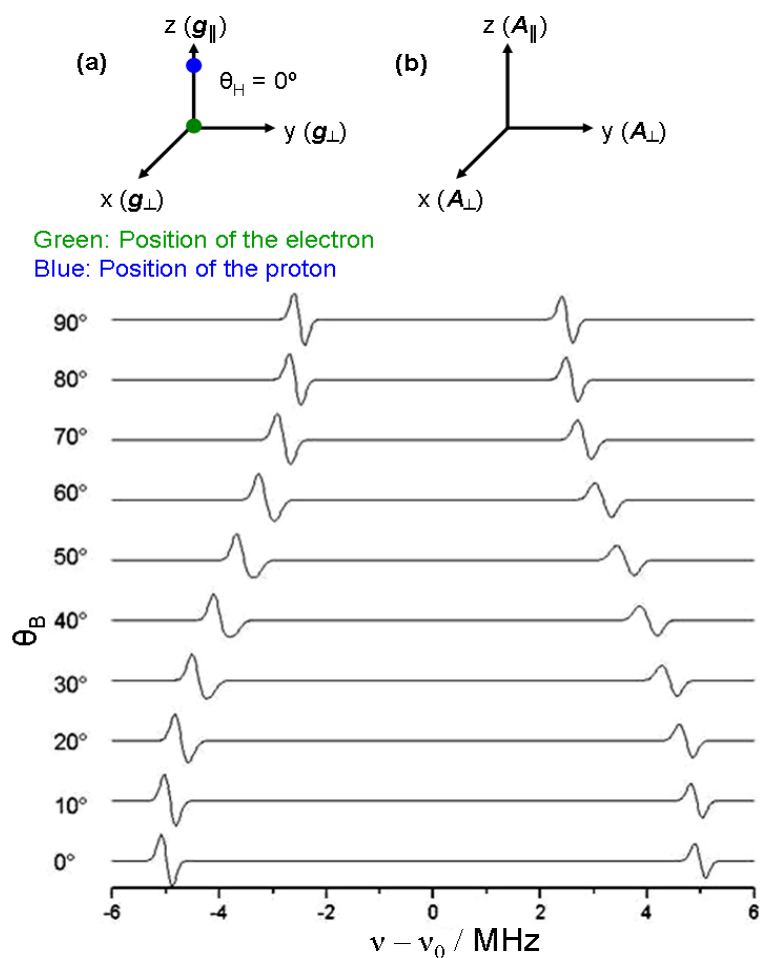
Figure 2.11 Magnetic field orientation (θ_B) dependence of the ENDOR spectrum, simulated for an axially symmetric $S = \frac{1}{2}$, $I = \frac{1}{2}$ system; a) coordinate system of the g tensor, showing the relative proton position ($\theta_H = 0°$); b) coordinate system of the hyperfine tensor; $A_1 = A_2 = A\perp = 5$ MHz, $A_3 = A_{\parallel} = 10$ MHz.

An alternative geometrical arrangement involves the rotation of the proton tensor so that it is perpendicular to the g tensor, *i.e.*, $\theta_H = 90°$ (Figure 2.12). When $\theta_B = 0°$, only the smallest coupling A_2 ($A\perp$) is observed, as this is now aligned along the z axis (in the g frame). Between 0 and 90°, a linear combination of $A_{\parallel}$ and $A_{\perp}$ gives resonances with intermediate coupling values. A coupling of 5 MHz is observed at every field position, as a result of the presence of the $A_{\perp}$ component in the z direction and the x-y plane of the g frame. The maximum coupling ($A_{\parallel}$), is evident at a field position corresponding to $\theta_B = 90°$.
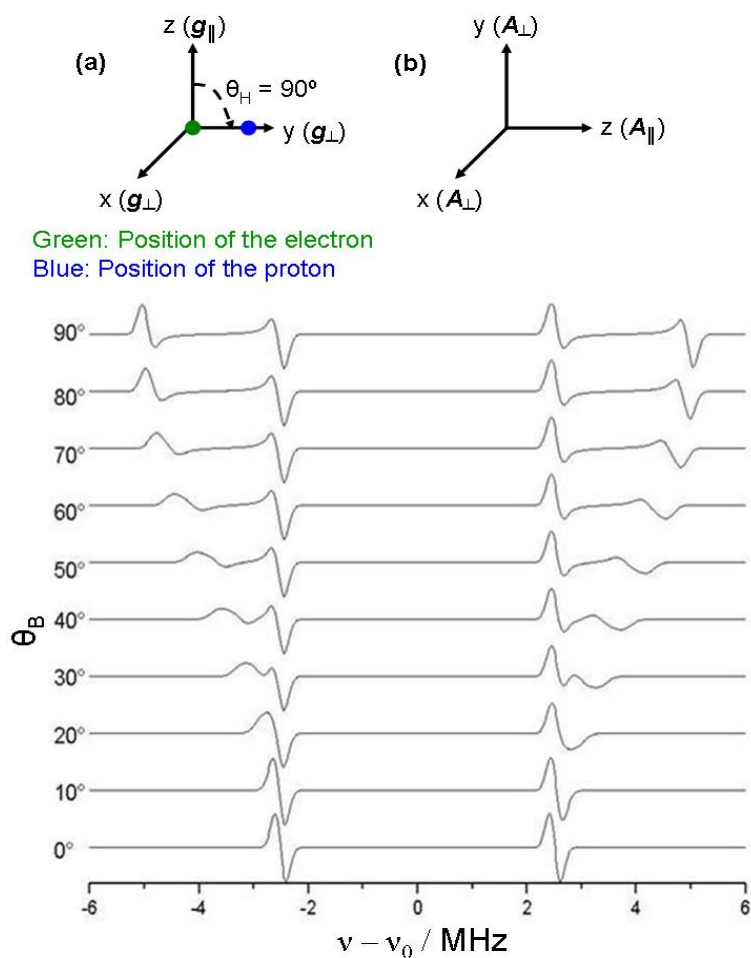
Figure 2.12 Magnetic field orientation (θ_B) dependence of the ENDOR spectrum, simulated for an axially symmetric $S = \frac{1}{2}$, $I = \frac{1}{2}$ system; a) coordinate system of the **g** tensor, showing the relative proton position ($\theta_H = 90°$); b) coordinate system of the hyperfine tensor; $A_1 = A_2 = A_\perp = 5$ MHz, $A_3 = A_\parallel = 10$ MHz.

The spectra are further complicated if an arbitrary angle for the position of the proton is chosen, for example $\theta_H = 50°$ (Figure 2.13). Only a partial contribution from A_3 is now observed when $\theta_B = 0°$. The magnitude of this is dependent on θ_H. At $\theta_B = 40°$ (*i.e.*, $90° - \theta_H$) $A_1 = A_2 = 5$ MHz is visible. This coupling is present in the spectra at all remaining angles due to contribution of the *x-y* plane. However, $A_3 = 10$ MHz is only evident at $\theta_B = 50°$ because this is the only angle at which the *z* axis of the hyperfine tensor is aligned with that of the field vector.

It must be noted that the largest coupling for an axial hyperfine tensor is observed only at the field position which corresponds to the angle at which that tensor is in relation to the **g** tensor (assuming g_z is aligned with the *z* axis of the field vector). Therefore, for a real axial system, it is necessary to perform the orientation selection experiment in order to determine at which field position the largest coupling occurs. This provides valuable information about the mutual orientation between the interacting spins.
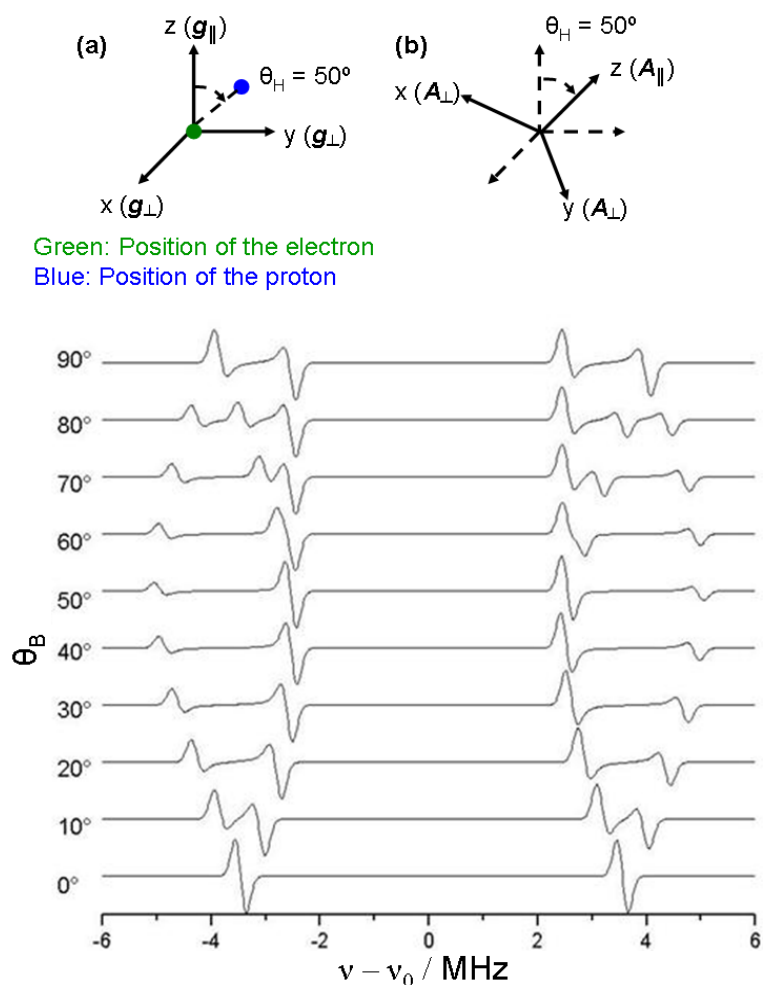
Figure 2.13 Magnetic field orientation (θ_B) dependence of the ENDOR spectrum, simulated for an axially symmetric $S = \frac{1}{2}$, $I = \frac{1}{2}$ system; a) coordinate system of the g tensor, showing the relative proton position ($\theta_H = 50°$); b) coordinate system of the hyperfine tensor; $A_1 = A_2 = A\perp = 5$ MHz, $A_3 = A_\parallel = 10$ MHz.

The EPR profiles shown in Figure 2.11-2.13 are even more complex if the sign of the hyperfine tensors are different, for example if $A\perp = -5$ MHz and $A_\parallel = +10$ MHz. This type of scenario will not be considered here.

2.3.5 The point-dipole approximation

The point-dipole approximation enables the calculation of the electron-nuclear distance from ENDOR spectroscopy. This approximation is given in Equation 2.28:

$$A_{\text{dip}}^{\zeta} = \left(\frac{\mu_0}{4\pi h}\right)\frac{g\mu_B g_n \mu_n}{R^3}\left(3\cos^2\xi - 1\right) \qquad [2.28]$$

This equation can be used to calculate the distance (R) for a pure dipolar coupling for a given orientation (θ_H) of the hyperfine tensor in Hz (μ_0 is the vacuum permittivity, μ_n and μ_B are the nuclear and Bohr magneton respectively, and g and g_n

are the electronic and nuclear g values). The equation considers only magnetic dipoles as point charges and is therefore only valid for distances of greater than 2 Å, which is common in transition metal complexes, where the unpaired electron is metal centred and the superhyperfine occurs with ligand nuclei.[2]

2.3.6 ^{14}N ENDOR and the quadrupole interaction

In order to fully understand systems containing nitrogen atoms, it is necessary to determine the nitrogen hyperfine data in addition to the proton hyperfine data.[22] The nitrogen isotope of highest natural abundance (99.6%) is ^{14}N ($I_{14N} = 1$). ^{14}N ENDOR signals in fluid solution were first detected in 1970 by Leniart, Vedrine and Hyde.[23] It is possible to extract the ^{14}N hyperfine coupling constants from well resolved EPR spectra, but for a more accurate determination of the ^{14}N hyperfine coupling constant and the nuclear quadrupole data, simulation of ^{14}N ENDOR data is necessary.

Since the ^{14}N hyperfine couplings (A) are much larger than the field dependent nuclear Zeeman interactions (v_n), the spectra are centred at $A/2$ and split by $2v_n$, as shown in Figure 2.14. In strongly coupled Cu-N systems, such as [Cu(BOX)](OTf)$_2$ systems, overlap of ^1H and ^{14}N signals at low frequencies (X-band), can complicate the analysis of the spectra. This difficulty can be solved by using higher frequencies (for example Q-band), which also provide better orientation selection as discussed earlier.[8]
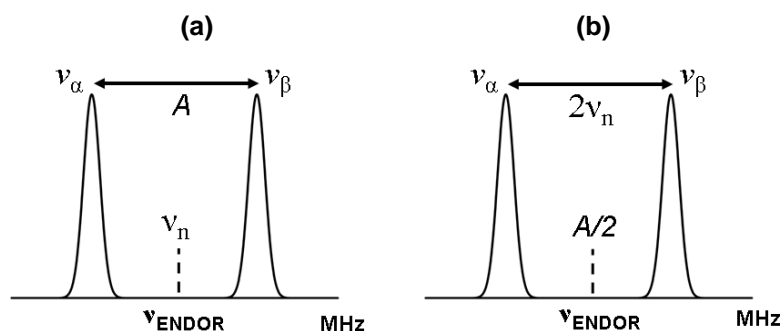
Figure 2.14 Nitrogen ENDOR spectrum showing two transitions (v_α and v_β) for (a) the weak coupling case: $|v_n| > |A/2|$ and (b) the strong-coupling case: $|v_n| < |A/2|$.

^{14}N produces characteristic quadrupole effects in hyperfine spectra, particularly in transition metal complexes. When $I > 1/2$, a strong interaction occurs between the electric quadrupole moment (Q) of the nucleus and the electric field gradients generated by the surrounding electron clouds. Q is a characteristic of the particular nucleus and provides a measurement of the deviation of the nuclear charge distribution from a spherical shape.[24] An 'elongated' nucleus has a positive Q and a 'flattened' nucleus a

negative Q. The coupling of Q with the electric field gradient of the sample is known as the *quadrupole interaction*.[8] This can have a substantial effect on the line shape of hyperfine spectra, as shown in Figure 2.15, and is therefore an important factor to consider.[8] No nuclear quadrupole effect will occur in a spherical situation or in highly symmetric paramagnets (*e.g.*, strictly octahedral or tetrahedral) because no electric field gradient will be present at the nucleus.[11] Likewise, no nuclear quadrupole effect will be seen for anisotropic paramagnets tumbling rapidly in solution due to the electric field gradient at the nucleus averaging to zero, but the effect may be visible in immobile paramagnets of lower symmetry.[11]
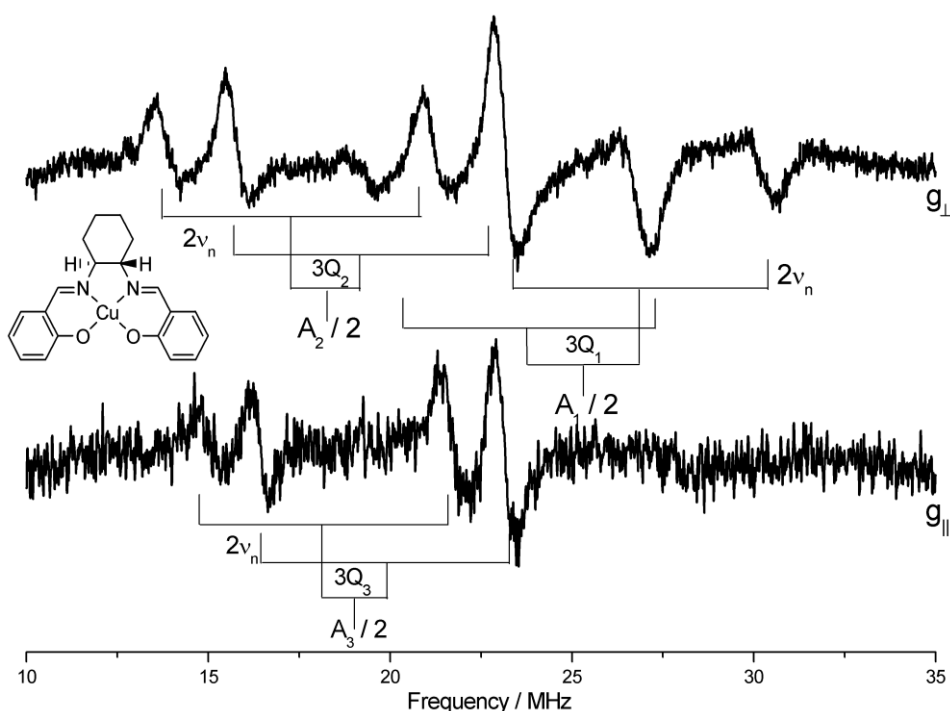
Figure 2.15 Nitrogen ENDOR spectra for a Cu(II) salen complex, recorded at $g_\perp$ and $g_\parallel$, highlighting the hyperfine and quadrupole coupings.[8,17]

The quadrupole Hamiltonian (H_Q) is expressed as:

$$H_Q = \mathbf{I} \cdot \mathbf{Q} \cdot \mathbf{I} \qquad [2.29]$$

where $\mathbf{I}$ is the nuclear spin vector operator and $\mathbf{Q}$ is the quadrupole tensor that is traceless and symmetric.

For first order high field approximations, the spin Hamiltonian (in the laboratory frame) becomes

$$H_Q \approx \tfrac{1}{2} Q_{zz}(3I^2_z - I(I+1)) \qquad [2.30]$$

The EPR selection rules, $\Delta M_S = \pm 1$ and $\Delta M_I = 0$, mean that quadrupole effects in first order are not usually observed in EPR spectra. However, these effects are readily observed in hyperfine spectra including ENDOR, HYSCORE (Hyperfine Sublevel

Correlation) and ESEEM (Electron Spin Echo Envelope Modulation), where $\Delta M_I = \pm1$ and $\Delta M_S = 0$.[8]

The nuclear quadrupole tensor has three principal values:

$$Q_{xx} = [-e^2qQ/4h)](1 - \eta) \qquad\qquad [2.31]$$

$$Q_{yy} = [-e^2qQ/4h)](1 + \eta) \qquad\qquad [2.32]$$

$$Q_{zz} = e^2qQ/2h \qquad\qquad [2.33]$$

where the asymmetry parameter η is equal to $(Q_{xx} - Q_{yy})/Q_{zz}$ with $|Q_{zz}| > |Q_{yy}| > |Q_{xx}|$, and Q is the coupling constant.[8] Since the quadrupole tensor **Q** is traceless, it is therefore determined only by the orientation and two other parameters, usually e^2qQ/h and η. The quadrupole coupling constants (e^2qQ/h) are dependent on both the properties of the nucleus (quadrupole tensor **Q**) and on the properties of the chemical bonds (electric field gradient eq).[22,25] In this thesis, A, Q, e^2qQ/h and η are reported for the ^{14}N ENDOR spectra.

2.4 Summary

Both CW-EPR and CW-ENDOR are powerful methods for the characterisation of paramagnetic systems in chemistry. An overview of the theory of these techniques has been presented. For EPR, the electron Zeeman, nuclear Zeeman, hyperfine interactions and *g*-matrix were firstly explained, before discussing the causes and effects of superhyperfine splitting, comparing the advantages of *X*- and *Q*-band frequencies, and evaluating the physical state of the sample. The ENDOR explanation began with the fundamentals of spin populations, which led to a description of the steady state ENDOR effect, orientation selective ENDOR and the point-dipole approximation. Finally, the quadrupole interaction was discussed, with particular focus on ^{14}N nuclei. When appropriate, the relevance of these topics to Cu(II) complexes has been explained.

However, a complete description of the physics and concepts behind the EPR technique is beyond the scope of this chapter. It should be noted that a number of text books describing the practicalities of EPR, the fundamental theory and the primary applications of the technique to different areas of chemistry, physics and biology are widely available, some of which are devoted to transition metal complexes.[1,4,8,11]

It is important also to acknowledge that great advances have been made in the fields of pulsed EPR and high-frequency EPR in the last 20 years. Pulsed EPR has provided experimentalists with an additional method to probe the paramagnetic system, particularly with the advanced hyperfine techniques of ENDOR, HYSCORE (Hyperfine Sublevel Correlation), ESEEM (Electron Spin Echo Envelope Modulation) and ELDOR

(Electron Electron Double Resonance).[26] Due to the increased absolute sensitivity of high-frequency EPR, it is a particularly useful technique for studying systems where the number of paramagnets is inherently low.

Despite the increasing popularity of pulsed and high frequency ENDOR, *X*-band and *Q*-band CW-EPR and CW-ENDOR continue to be indispensible techniques in the field of EPR, and are excellent tools to study asymmetric transition metal catalysts.

2.5 References

1   Pilbrow, J. R. *Transition Ion Electron Paramagnetic Resonance*; 1st ed.; Oxford Science Publications, Oxford University Press, **1990**.

2   Murphy, D. M.; Farley, R. D. *Chemical Society Reviews,* **2006**, *35*, 249.

3   Carter, E.; Murphy, D. M. In *Spectroscopic Properties of Inorganic and Organometallic Compounds: Volume 40*; The Royal Society of Chemistry: **2009**; Vol. 40, p 355.

4   Weil, J. A.; Bolton, J. R.; Wertz, J. E. *Electron Paramagnetic Resonance: Elementary Theory and Practical Applications*; John Wiley & Sons, Inc., **1994**.

5   Gerlach, W.; Stern, O. *Z. Phys,* **1921**, *8*.

6   Uhlenbeck, G. E.; Goudsmit, S. *Naturwissenschaften,* **1925**, *13*.

7   Zavoisky, E. *J. Phys. U.S.S.R.,* **1945**, *211*, 245.

8   Brustolon, M.; Giamello, E. *Electron Paramagnetic Resonance: A Practitioner's Toolkit*; John Wiley & Sons, Inc., **2009**.

9   Rieger, P. H. *Electron Spin Resonance: Analysis and Interpretation*; RSC Publishing, **2007**.

10   *Continuous Wave EPR, http://www.bruker-biospin.cn.whatisepr.html*, **accessed 06/12/10**.

11   F. E. Mabbs; Collison, D. *Electron Paramagnetic Resonance of d Transition Metal Compounds*; Elsevier Science Publishers B.V.: Amsterdam, **1992**; Vol. 16.

12   Mabbs, F. E. *Chemical Society Reviews,* **1993**, *22*, 313.

13   Pilbrow, J. R.; Lowrey, M. R. *Reports on Progress in Physics,* **1980**, *43*, 433.

14   Giugliarelli, G.; Cannistraro, S. *Chemical Physics,* **1985**, *98*, 115.

15   Peisach, J.; Blumberg, W. E. *Archives of Biochemistry and Biophysics,* **1974**, *165*, 691.

16   Murphy, D. M.; Fallis, I. A.; Carter, E.; Willock, D. J.; Landon, J.; Van Doorslaer, S.; Vinck, E. *Physical Chemistry Chemical Physics,* **2009**, *11*, 6757.

17   Murphy, D. M.; Caretti, I.; Carter, E.; Fallis, I. A.; Göbel, M. C.; Landon, J.; Doorslaer, S. V.; Willock, D. J. *Inorganic Chemistry,* **2011**, *50*, 6944.

18   Finazzo, C.; Calle, C.; Stoll, S.; Van Doorslaer, S.; Schweiger, A. *Physical Chemistry Chemical Physics,* **2006**, *8*, 1942.

19   Hoffman, B. M.; Martinsen, J.; Venters, R. A. *Journal of Magnetic Resonance,* **1984**, *59*, 110.

20   Hurst, G. G.; Henderson, T. A.; Kreilick, R. W. *Journal of the American Chemical Society,* **1985**, *107*, 7294.

21   Henderson, T. A.; Hurst, G. C.; Kreilick, R. W. *Journal of the American Chemical Society,* **1985**, *107*, 7299.

22   Kurreck, H.; Kirste, B.; Lubitz, W. *Electron Nuclear Double Resonance Spectroscopy of Radicals in Solution: Application to Organic and Biological Chemistry*; VCH Publishers, Inc., **1988**.

23   Leniart, D. S.; Vedrine, J. C.; Hyde, J. S. *Chemical Physics Letters,* **1970**, *6*, 637.

24   Townes, C. H.; Dailey, B. P. *Journal of Chemical Physics,* **1949**, *17*, 782.

25   Lucken, E. A. C. *Nuclear Quadrupole Coupling Constants*; Academic Press: New York, **1969**.

26   Schweiger, A.; Jeschke, G. *Principles of Pulse Electron Paramagnetic Resonance*; Oxford University Press, **2001**.

Chapter 3

Experimental section

3.1 Introduction

This chapter will provide information on the chemicals used and the synthetic methods followed in the main results and discussion chapters 4, 5 and 6. The specifications and conditions used for the EPR and ENDOR spectrometers are also given.

3.2 Chemicals and syntheses

All manipulations of air and moisture sensitive species were performed under an atmosphere of dinitrogen using standard Schlenk and glove-box techniques. Solvents were dried by passing through an alumina drying column incorporated into a MBraun SPS800 solvent purification system, except in the case of tetrahydrofuran (abbreviated hereafter to THF), which was dried over potassium and distilled under argon. Solvents used in anaerobic reactions were degassed and stored under argon in Teflon valve ampoules. All other solvents and reagents were purchased from commercial suppliers and used as received, unless otherwise stated.

3.2.1 Experimental details for Chapter 4

The BOX ligand labelled (**1**) in Scheme 3.1, (−)-2,2′-isopropylidenebis[(4S)-4-phenyl-2-oxazoline], CAS no. 131457-46-0 (*Sigma Aldrich*), was used as received.
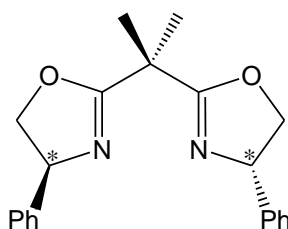
Ligand **1**

Scheme 3.1 Schematic illustration of (**1**), (−)-2,2′-isopropylidenebis[(4S)-4-phenyl-2-oxazoline].

Variable ratio studies: The variable ratios studies using ligand (**1**) with Cu(OTf)$_2$ and with CuCl$_2$, were performed *in-situ*.[1] To a 10 mL round bottom flask containing a magnetic stirring bar was added Cu(OTf)$_2$ (0.01 mmol) and ligand (**1**). THF (1 mL) was added, and the reaction mixture was stirred for 1 hour. The amount of ligand used was calculated for the required metal:ligand ratios; 1:0, 1:0.5, 1:1, 1:2 and 1:6. This method was also adopted for the variable ratio study using CuCl$_2$ (0.01 mmol)

but using dichloromethane (abbreviated hereafter to DCM) (1 mL) instead of THF for improved solubility.

[Cu(II)(1a)]: In order to ensure than only one complex was formed, the heteroleptic [Cu(II)(**1a**)] complex was isolated as a solid, as described by Jørgensen *et al.*[2] In a Schlenk tube, Cu(OTf)$_2$ (0.05 mmol) and the bis(oxazoline) ligand (0.05 mmol) were charged with dry THF (1 mL), and the reaction mixture was stirred for 2 hours. The catalyst solution was left under a gentle flow of N$_2$ for several days, until the solvent had evaporated and the solid was recovered.

[Cu(II)(1b)]: The homoleptic complex, [Cu(II)(**1b**)], was synthesised *in-situ* by stirring (**1**) (0.06 mmol) with Cu(OTf)$_2$ (0.01 mmol) in THF (1 mL) for 4 hours at room temperature. HR ES-MS was performed for [Cu(II)(**1b**)], found (calc. for C$_{42}$H$_{44}$CuN$_4$O$_4$): 731.2635 (731.2659). Whilst homoleptic complexes of this type have been isolated, none have been crystallographically characterised.[3]

[Cu(II)(1c)]: The heteroleptic complex [Cu(II)(**1c**)] was isolated as a solid as described by Jørgensen *et al.*,[2] and described above for [Cu(II)(**1a**)]. CuCl$_2$ and ligand (**1**) were used to synthesise [Cu(II)(**1c**)]. The solvent used was DCM.

3.2.2 Experimental details for Chapter 5

The BOX ligands labelled (**2**), 2,2′-methylenebis[(4*S*)-4-phenyl-2-oxazoline], CAS no. 132098-59-0 (*Sigma Aldrich*), and (**3**), 2,2′-isopropylidenebis[(4*S*)-4-*tert*-butyl-2-oxazoline], CAS no. 131833-93-7 (*Sigma Aldrich*), in Scheme 3.2, were used as received.

Scheme 3.2 Schematic illustration of (**2**), 2,2′-methylenebis[(4*S*)-4-phenyl-2-oxazoline],and (**3**), 2,2′-isopropylidenebis[(4*S*)-4-*tert*-butyl-2-oxazoline].

[Cu(II)(2a-c)] and [Cu(II)(3a-c)]: These complexes were synthesised *in-situ* as described in Section 3.2.1 for the similar complexes [Cu(II)(**1a-c**)].

[Cu(II)(3d)]: The heteroleptic complex [Cu(II)(**3d**)] was synthesised according to the method of Evans *et al.*[4] A flame-dried round bottom flask with magnetic stirrer was charged with [Cu(II)(**3c**)] (0.10 mmol) and AgSbF$_6$ (0.20 mmol) in an inert

atmosphere (N$_2$) glove-box. The flask was brought out of the glove-box, and 1 mL of dry DCM was added via syringe. The mixture was stirred in the dark for 3 hours to produce a green solution with a white AgCl precipitate, which was filtered off.

3.2.3 Experimental details for Chapter 6

PhI=NTs: The synthesis of PhI=NTs (p-CH$_3$C$_6$H$_4$SO$_2$N=IPh), was performed according to the method of Yamada *et al.*[5] (Diacetoxyiodo)benzene (3.20 g, 10 mmol) was added to a stirred mixture of p-toluenesulfonamide (1.71 g, 10 mmol), potassium hydroxide (1.40 g, 25 mmol) and methanol (abbreviated hereafter to MeOH) (40 mL), ensuring that the reaction mixture was kept below 283 K. The resulting yellow coloured solution was stirred for three hours at room temperature. The reaction mixture was then poured into a large excess of iced water to precipitate a yellow coloured solid on standing overnight, which was recrystallised from MeOH to give N-tosyliminophenyliodinane (60–70% yield). ^{1}H NMR (d^6-DMSO): δ 7.73-7.16 (m, 9H, Ph), 2.37 (s, 3H, Me).

Aziridination reaction: The general method adopted for the aziridination reaction was described by Hutchings *et al.*[6] Styrene (1.0 mmol), PhI=NTs (1.5 mmol) and [Cu(II)(**1a**)] (0.15 mmol) were stirred together in acetonitrile (abbreviated hereafter to AcN) or MeOH (2.5 cm^3) at room temperature. The reaction was stirred in air and portions of the reaction mixture were extracted at various time intervals. Any variations to this method are stated alongside the resulting EPR spectra.

3.3 Spectroscopic measurements

3.3.1 EPR and ENDOR

For CW-EPR measurements, the copper complexes [Cu(II)(**1a-c**)], [Cu(II)(**2a-c**)] and [Cu(II)(**3a-d**)] (*ca.* 7x10^{-3} M) were dissolved in a 1:1 mixture of THF:DCM. This solvent system gave the optimum glass quality and all complexes were soluble at this level in either THF or DCM.

For CW-ENDOR and pulsed ENDOR measurements, the heteroleptic copper complexes [Cu(II)(**1a,c**)] (*ca.* 4x10^{-2} M for ENDOR) were dissolved in either d^8-THF:d^2-DCM, or d^3-AcN:d^2-DCM while the homoleptic complex [Cu(II)(**1b**)] was dissolved in d^3-AcN:d^2-DCM. The homoleptic complex [Cu(II)(**2b**)] (*ca.* 4x10^{-2} M for ENDOR) was dissolved in d^8-THF:d^2-DCM, as was the heteroleptic complex [Cu(II)(**3c**)] (*ca.* 4x10^{-2} M for ENDOR). The choice of solvent considerably affected the solubility, where higher concentrations were required for the CW-ENDOR

measurements.

All *X*-band CW-EPR spectra were recorded on a Bruker EMX spectrometer operating at 100 kHz field modulation and equipped with a high sensitivity *X*-band cavity (ER 4119HS). The spectra were recorded at a microwave power of 10 mW at 140 K.

The *Q*-band CW-ENDOR spectra were recorded at 10 K on a CW Bruker ESP 300E series spectrometer equipped with an ESP360 DICE ENDOR unit, operating at 12.5 kHz field modulation in a *Q*-band ENDOR cavity (Bruker ER 5106 QT-E). The ENDOR spectra were obtained using 8 dB *rf* power from an ENI A-300 *rf* amplifier and 80 or 250 kHz *rf* modulation depth and 1 mW microwave power. ^{1}H ENDOR spectra were recorded at high modulation frequency (200-250 kHz) and low modulation frequency (50-80 kHz) as standard procedure, since high modulation optimises large couplings of low intensities whilst low modulation is useful for smaller couplings of stronger intensities.

The *X*-band pulsed EPR/ENDOR spectra were recorded on a Bruker Elexsys E580 spectrometer equipped with a liquid Helium cryostat from Oxford Inc. The spectra were taken at 10 K, with a repetition rate of 333 kHz. The pulse sequence π-T-π/2-τ-π-τ-echo was used for the Davies ENDOR measurements, using *mw* pulse lengths of t_π = 256 ns, $t_{\pi/2}$ = 128 ns, and an interpulse time τ of 800 ns. An *rf* π pulse of variable frequency and a length of 18 μs was applied during time T of 20 μs.

EPR simulations were performed using the Sim32 software,[7] and ENDOR simulations were performed using the Easyspin package, along with the Matlab interface.[8]

3.3.2 UV-Vis

UV-Vis data was acquired in solution with a Perkin Elmer Lambda 900 at room temperature.

3.3.3 NMR

NMR samples were prepared in Wilmad 5 mm NMR tubes. NMR spectra were recorded on Bruker Advance DPX 400, 500, 600. NMR spectra are quoted in ppm and were referenced internally relative to the residual protic solvent (^{1}H) resonances.

3.3.4 Mass Spectra

Mass spectra were recorded on a Waters LCT Premier XE or Waters GCT Premier mass spectrometer by the mass spectrometry service at the School of Chemistry, Cardiff University.

3.4 DFT calculations

The EPR parameters were calculated *via* spin-unrestricted density functional computations using the ORCA package[9-12] on the reported crystal structures of [Cu(II)(**1a**)][1] and [Cu(II)(**1c**)][2]. The computations were performed with the B3LYP functional. Basis sets with significant flexibility in the core region were used (ORCA basis sets 'CoreProp' (CP(III))[13] for copper, and a Barone basis set 'EPRII'[14] for the hydrogen atoms).

3.5 References

1   Evans, D. A.; Burgey, C. S.; Paras, N. A.; Vojkovsky, T.; Tregay, S. W. *Journal of the American Chemical Society,* **1998**, *120*, 5824.

2   Thorhauge, J.; Roberson, M.; Hazell, R. G.; Jorgensen, K. A. *Chemistry - A European Journal,* **2002**, *8*, 1888.

3   Lowenthal, R. E.; Abiko, A.; Masamune, S. *Tetrahedron Letters,* **1990**, *31*, 6005.

4   Evans, D. A.; Barnes, D. M.; Johnson, J. S.; Lectka, T.; von Matt, P.; Miller, S. J.; Murry, J. A.; Norcross, R. D.; Shaughnessy, E. A.; Campos, K. R. *Journal of the American Chemical Society,* **1999**, *121*, 7582.

5   Yamada, Y.; Yamamoto, T.; Okawara, M. *Chemistry Letters,* **1975**, 361.

6   Taylor, S.; Gullick, J.; McMorn, P.; Bethell, D.; Page, P. C. B.; Hancock, F. E.; King, F.; Hutchings, G. J. *Journal of the Chemical Society-Perkin Transactions 2,* **2001**, 1714.

7   Spalek, T.; Pietrzyk, P.; Sojka, Z. *Journal of Chemical Information and Modeling,* **2005**, *45*, 18.

8   Stoll, S.; Schweiger, A. *Journal of Magnetic Resonance,* **2006**, *178*, 42.

9   Neese, F. *The Journal of Chemical Physics,* **2001**, *115*, 11080.

10   Neese, F. *The Journal of Physical Chemistry A,* **2001**, *105*, 4290.

11   Neese, F. *The Journal of Chemical Physics,* **2003**, *118*, 3939.

12   Neese, F. *The Journal of Chemical Physics,* **2005**, *122*, 034107.

13   *This basis is based on the TurboMole DZ basis developed by Ahlrichs and co-workers and obtained from the basis set library under ftp.chemie.uni-karlsruhe.de/pub/basen, R. Ahlrichs and co-workers (unpublished).*

14   Barone, V. *Recent Advances in Density Functional Methods*; World Scientific Publ. Co.: Singapore, **1996**.

Chapter 4

Influence of counterions on the structure of (−)-2,2′-isopropylidene-bis[(4*S*)-4-phenyl-2-oxazoline] copper(II) complexes; An EPR and ENDOR investigation

4.1 Introduction

The applications of copper-bis(oxazoline) complexes (hereafter abbreviated to [Cu(BOX)]), in catalysis were discussed earlier in Chapter 1. [Cu(BOX)] complexes are used in a vast array of asymmetric reactions, including the Diels-Alder reaction,[1-10] cyclopropanation,[11-14] and aziridination.[15-17] The chiral BOX ligand is coordinated to a suitable Cu(II) salt, and currently most of the catalysis work involving Lewis metal based BOX complexes have utilised TfO^- ($TfO^- = CF_3SO_3^-$) or SbF_6^- counterions. The choice of counterion is reported to have a large influence on the resulting enantioselectivities and product yields. In the current chapter, a detailed characterisation of the paramagnetic [Cu(II)(BOX)] complexes (shown in Scheme 4.1) will be described using EPR and ENDOR spectroscopy, with specific emphasis on the influence of the counterion (TfO^- or Cl^-) on the structure of the complex in solution.
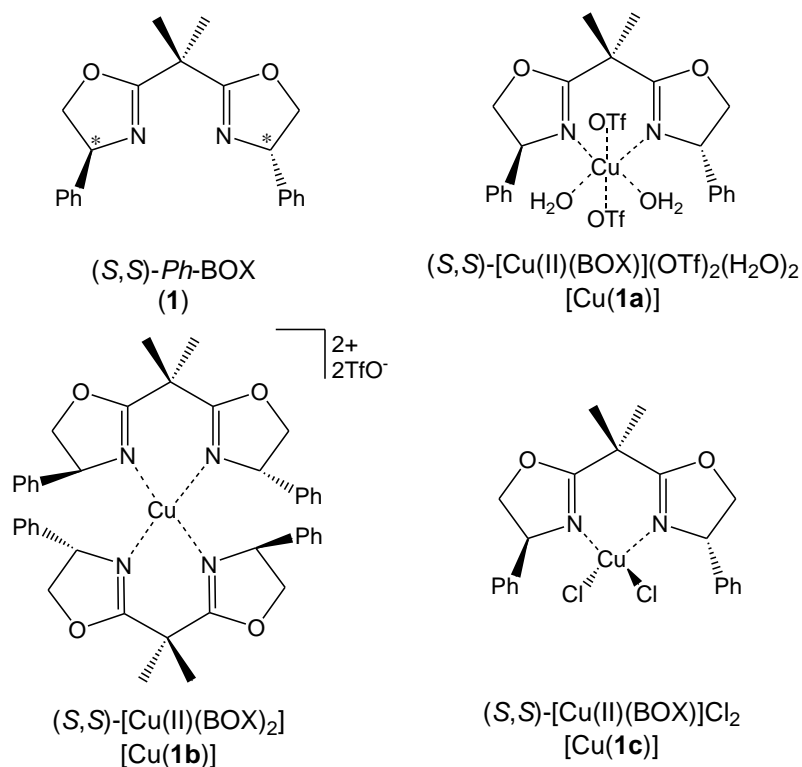
Scheme 4.1 Schematic illustration of the [Cu(II)(**1a-c**)] complexes as identified by EPR/ENDOR.

For the BOX catalysed enantioselective aziridination reaction, Evans et al.,[12,18] demonstrated that triflates and hexafluorophosphates form efficient catalysts with Cu(I), whilst halides, cyanides, acetates and perchlorates were inefficient. For the Diels-Alder reaction, Fraile et al.,[19] noted a significant decrease in selectivity in the reaction of styrene with ethyl diazoacetate when triflate counterions were replaced by chlorides. They later postulated that the choice of counterion can affect the nature of the reaction mechanism, leading to undesired side-reactions that are non-asymmetric, resulting in lower enantiomeric excess (ee).[20] As highlighted by Bolm et al.,[21] although the choice of counterion has been discussed by several research groups and related to several asymmetric reactions, an understanding of the background to these observations is limited.

Furthermore, it is well known that the geometry of the [Cu(II)(BOX)] complex, which is heavily dependent on the counterion, affects the catalysis.[22] For example, when triflate is utilised as the counterion, the X-ray crystal structure of the resulting [Cu(II)(BOX)] complex, [Cu(II)(**1a**)], reveals a Jahn-Teller distorted octahedral complex with TfO$^-$ coordinated in an axial position and water coordinated in the equatorial plane.[23] By contrast, when $CuCl_2$ is employed as the starting salt, the resulting complex, [Cu(II)(**1c**)], exhibits a distorted square-planar geometry with two chloride counterions coordinated to the metal centre at ~33° out of the copper-ligand plane.[8] The presence of the coordinating water molecules affects the direction of approach of substrates to the metal centre, resulting in differences in enantioselectivity.

Despite the importance of the counterion in modulating the catalytic activity, few experimental techniques can probe such influences in solution. For paramagnetic Cu(II) based BOX complexes, EPR and the related hyperfine techniques such as ENDOR, are an ideal method to examine any structural or electronic perturbations to the metal complex caused by the different counterions. A limited number of papers have been reported on the CW-EPR spectra of [Cu(II)(BOX)] complexes, and these primarily focused on the oxidation state of the Cu(II) ion, rather than the role of the counterion.[10,21,24-27] One of the first groups to recognise how advanced EPR techniques can be used to probe these counterion (TfO$^-$, SbF$_6^-$, Cl$^-$, Br$^-$) effects for the structurally similar Cu(II)-bis(sulfoximine) complexes in the Diels–Alder reaction was Bolm and Gescheidt.[21,28] A combination of paramagnetic techniques, including CW-EPR, free induction decay (FID) detected EPR, pulsed ENDOR and hyperfine sublevel correlation (HYSCORE) were used in their investigations into the counterion effect.[21] The EPR spectra of the copper-bis(sulfoximine) complexes showed significant differences

depending on the starting Cu(II)-salt (CuCl$_2$, CuBr$_2$, Cu(OTf)$_2$ and CuCl$_2$/AgSbF$_6$). Upon subsequent addition of a substrate molecule, such as N-(1-oxoprop-2-en-1-yl)oxazolidin-2-one, changes were observed in the spectra, with distinct behaviour noted for the different counterions, showing again how EPR can be successfully used to monitor such reactions.[21] In complexes with counterions displaying the highest stereoselectivity (TfO$^-$ and SbF$_6^-$), the counterions shifted their position to enable substrate interactions, whilst Cl$^-$ and Br$^-$ remained coordinated in the same equatorial positions.

It is also important to probe the structural and electronic differences between the heteroleptic complexes ([Cu(II)(**1a**)] and [Cu(II)(**1c**)]), and the homoleptic complex ([Cu(II)(**1b**)]). This is important because in most cases, the metal based catalysts are prepared *in-situ* by mixing the metal salt and BOX ligands prior to catalysis. This may result in the formation of the heteroleptic or homoleptic complexes, depending on the reaction conditions, reactivity of the metal ions and ligand structure.[29] An excess of the BOX ligand clearly increases the likelihood of the formation of a homoleptic complex.

Hager *et al.*,[30] have explored the dynamics between metal-ligand 1:1 complexes and metal-ligand 1:2 complexes. After performing a competitive experiment in which the yields and % *ee* were recorded, they reported that the metal-ligand 1:2 complex is catalytically inactive. These complexes required prolonged reaction times, and significantly lower yields were observed as a result. Indeed Le Roux *et al.*,[31] highlighted the necessity for controlled synthetic conditions (*i.e.*, slow addition of ligand to metal, under dilute metal concentrations) to prevent the formation of homoleptic complexes. Attempts have therefore been made to increase the steric bulk of the BOX ligand in order to prevent formation of the homoleptic species, whereas the current work reveals a change in counterion may also achieve a similar result.[31]

This chapter therefore aims to present a thorough EPR and ENDOR investigation of complexes [Cu(II)(**1a-c**)]. It is firstly vital to fully characterise these complexes before considering their catalytic behaviour, in order to appreciate any changes that might occur to the spectra upon substrate addition. The BOX ligand **1** has been chosen for this study because of its commercial availability and wide range of applications. Two counterions which are known to produce very different catalytic results have been investigated; TfO$^-$, which is known to form [Cu(II)(BOX)] complexes resulting in high enantioselectivities, and the other, Cl$^-$, which produces poor catalytic results. Both heteroleptic ([Cu(II)(**1a,c**)]) and homoleptic ([Cu(II)(**1b**)]) complexes have been studied in order to recognise the possible consequences of synthesising the

complexes *in-situ* and to further understand the effect of the choice of counterions on the coordination of one or two BOX ligands to the Cu(II) metal centre.

4.2 Experimental

Full details of the experimental methods were given in Chapter 3, hence only a brief description is given here.

The complexes [Cu(II)(**1a-c**)] were prepared according to literature methods,[8,23] by reacting $Cu(OTf)_2$ or $CuCl_2$ with (**1**) in tetrahydrofuran or dichloromethane (abbreviated hereafter to THF/DCM) respectively). A metal:ligand ratio of 1:1 was used to synthesise the heteroleptic complexes [Cu(II)(**1a,c**)], whilst a ratio of 1:6 was used to synthesise the homoleptic complex [Cu(II)(**1b**)].

For CW- and pulsed EPR/ENDOR measurements, the heteroleptic copper complexes [Cu(II)(**1a,c**)] (*ca.* 7×10^{-3} M for EPR, *ca.* 4×10^{-2} M for ENDOR) were dissolved in either d^8-THF:d^2-DCM or d^3-acetonitrile (abbreviated hereafter to AcN):d^2-DCM, while the homoleptic complex [Cu(II)(**1b**)] was dissolved in d^3-AcN:d^2-DCM. For *X*-band CW-EPR, protic solvents were used. The choice of solvent considerably affected the solubility, where higher concentrations were required for the CW-ENDOR measurements.

All *X*-band EPR spectra were recorded on a Bruker EMX spectrometer equipped with a high sensitivity *X*-band cavity (ER 4119HS). The *Q*-band CW-ENDOR spectra were recorded at 10 K on a CW Bruker ESP 300E series spectrometer equipped with an ESP360 DICE ENDOR unit, in a *Q*-band ENDOR cavity (Bruker ER 5106 QT-E). The *X*-band pulsed EPR/ENDOR spectra were recorded on a Bruker Elexsys E580 spectrometer equipped with a liquid Helium cryostat from Oxford Inc.

4.3 Results and discussion

4.3.1 CW-EPR of [Cu(II)(*1a-c*)]

As mentioned in Section 4.1, the [Cu(II)(BOX)] complexes are most conveniently prepared by simply stirring a suitable Cu(II) salt with the required BOX ligand in solution. The solvent and the Cu(II):BOX ratio is then critical in order to form the desired [Cu(II)(BOX)] complex. This can be easily monitored by EPR spectroscopy, as shown in Figure 4.1. A solution of ligand (**1**) in THF:DCM (1:1) was stirred with $Cu(OTf)_2$ for 1 hour, and the resulting profile of the EPR spectra changes considerably as more of the $Cu(OTf)_2$ progressively coordinates with the BOX ligand (**1**). Figure 4.1a

shows the initial EPR spectrum of $Cu(OTf)_2$ in the absence of (**1**), while Figure 4.1b-e shows the resulting spectra after addition of increasing amounts of (**1**).
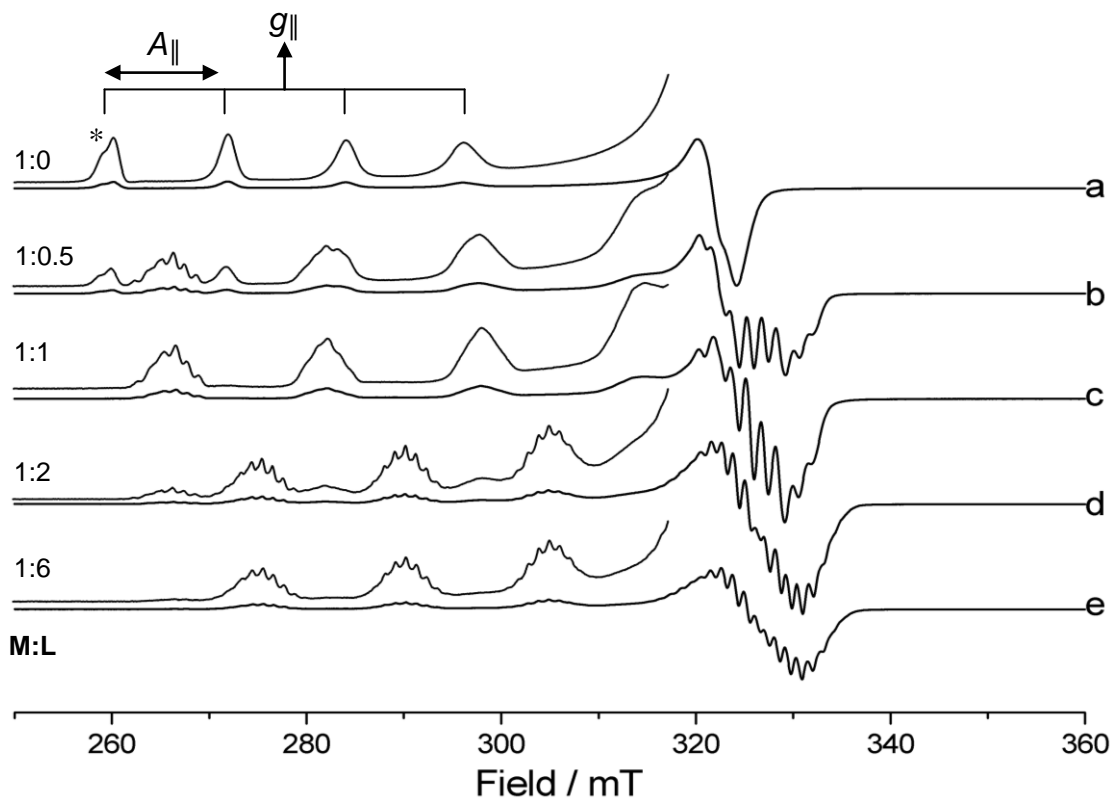
Figure 4.1 *X*-band CW-EPR spectra (140 K) of a) $Cu(OTf)_2$ in THF:DCM (1:1), containing increasing Cu(II):BOX (**1**) ratios (M:L); b) 1:0.5, c) 1:1, d) 1:2 and e) 1:6.

Figure 4.1a is typical of a system possessing axial symmetry; $g_{xx} = g_{yy} \neq g_{zz}$ and $A_{xx} = A_{yy} \neq A_{zz}$, as described in Section 2.2.5. The spin Hamiltonian parameters for this spectrum have been deduced through simulation of the spectrum, as discussed later. It was found that $g_1 = g_2 = 2.083$, $g_3 = 2.412$, $A_1 = A_2 = 13$ MHz, and $A_3 = 403$ MHz. To put these values into context, the four peaks in the parallel region of this spectrum are each separated by a distance of 403 MHz (labelled $A_{\parallel}$), and they are centred about a *g*-value of 2.412 (labelled $g_{\parallel}$). The four peaks in the perpendicular region, centred about a *g*-value of 2.083, cannot be distinguished as they are separated by only 13 MHz. Looking specifically at the peak labelled with an asterisk, both copper isotopes are evident (^{63}Cu and ^{65}Cu). As explained in Section 2.2.6, the difference of around 7% in the nuclear magnetic moments of ^{63}Cu and ^{65}Cu results in a broadening of the lines due to the larger hyperfine splitting of ^{65}Cu as a result of its larger g_n.[32] The slight shoulder which is visible to the left of this peak, is therefore the lowest field component of the ^{65}Cu hyperfine pattern.

The pronounced nitrogen superhyperfine couplings observed in Figures 4.1b-e, are clearly indicative of Cu(II) coordination to (**1**). At a Cu(II):BOX ratio of 1:0.5, a mixture of both Cu(II)(OTf)$_2$ and a Cu(II) coordinated BOX complex is observed (Figure 4.1b). At a Cu(II):BOX ratio of 1:1, a well resolved EPR spectrum is obtained, indicative of the formation of a single [Cu(II)(BOX)] complex. Superhyperfine splitting was explained in Section 2.2.6, and Figure 2.5b (Chapter 2) illustrated the intensities of nitrogen superhyperfine patterns for two equivalent nitrogen nuclei; 1:2:3:2:1. This is observed in Figure 4.1c, in which two nitrogen nuclei are clearly coordinated to the Cu(II) centre. For particularly well resolved spectra, more than five peaks may be visible, and this is due to the presence of two copper isotopes coordinating to two equivalent nitrogen nuclei. Finally, as the Cu(II):BOX ratio is increased (*i.e.,* 1:2 and 1:6, Figures 4.1d,e), the shape of the spectra changes further, indicative of the formation of a second [Cu(II)(BOX)] type complex ([Cu(II)(**1b**)]). In this complex, four nitrogen nuclei are coordinated to the Cu(II) centre, and therefore $2nI + 1 = 9$ lines are expected. It is however difficult to distinguish all of these lines, particularly in the perpendicular region, due to the broadness of the lines.
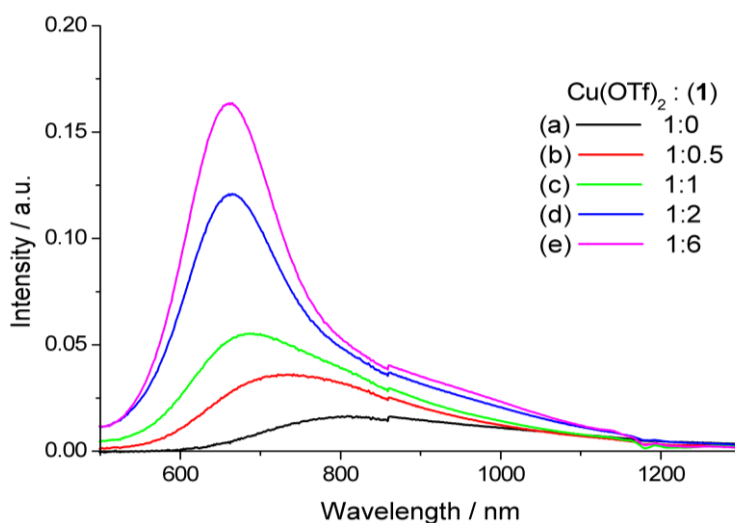
Figure 4.2 UV-vis spectra recorded in THF of a) Cu(OTf)$_2$, containing increasing Cu(II):BOX (**1**) ratios; b) 1:0.5, c) 1:1, d) 1:2 and e) 1:6.

The formation of the complexes [Cu(II)(**1a-b**)] in solution can also be followed by a shift of the metal centred *d-d* band in the UV-vis spectrum, although it can be difficult to determine detailed structural features of Cu(II) complexes from UV-vis spectra alone, due to their flexible coordination geometry and the common presence of several species in equilibrium.[33] These factors can affect the wavelengths, shapes and intensities of the absorption bands.[33] To record the UV-vis spectra shown in Figure 4.2,

Cu(OTf)$_2$ was mixed with the equivalent amount of BOX ligand in a THF solution to form homogeneous solutions. The *X*-band CW-EPR of these samples were shown in Figure 4.1. The heteroleptic [Cu(II)(**1a**)] complex exhibited a peak at 684 nm, which is smaller in wavelength than the peak at 798 nm recorded for Cu(OTf)$_2$. Excess ligand resulted in a peak at 661 nm, resulting from the homoleptic [Cu(II)(**1b**)] complex. A distinctive pattern is observed; with increasing addition of BOX ligand, the peak shifts to a smaller wavelength, highlighted in Table 4.1. The shoulder which is evident at 860 nm is an artefact from the spectrometer.

Table 4.1 Experimental λ_{max} values for the UV-vis spectra shown in Figure 4.2.

Cu(II)(OTf)$_2$: (1)	λ_{max} / nm
1:0	798
1:0.5	731
1:1	684
1:2	663
1:6	661
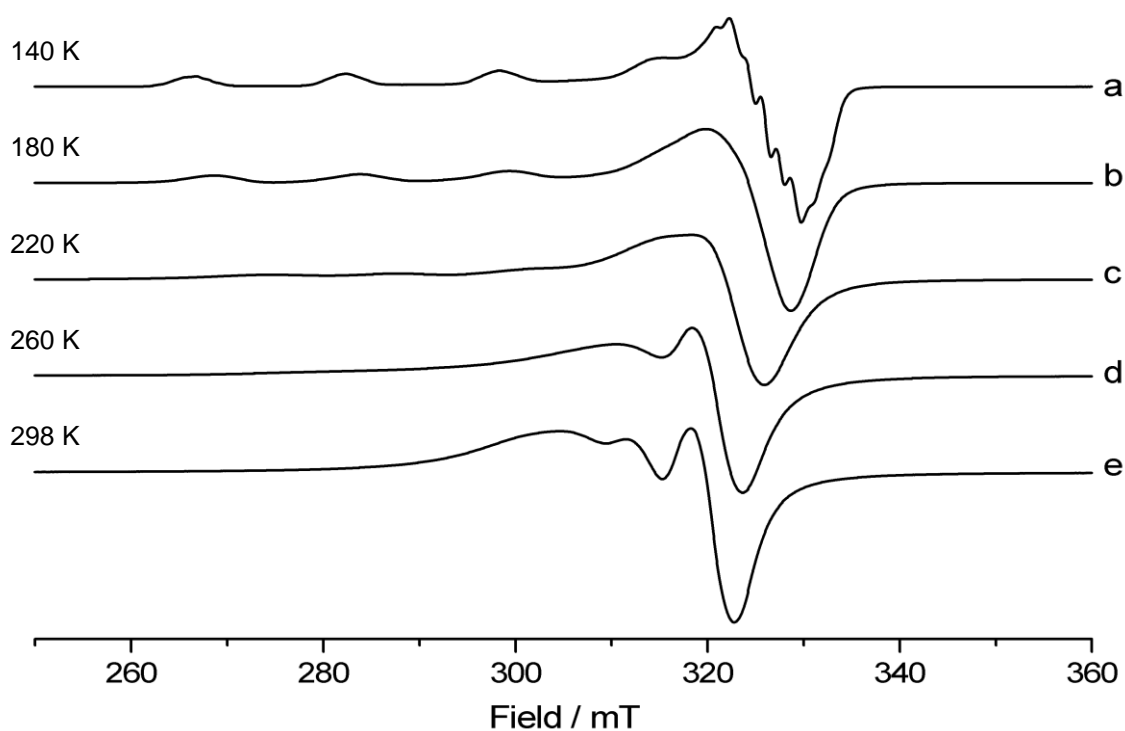
Figure 4.3 *X*-band CW-EPR spectra of [Cu(II)(**1a**)] in THF:DCM (1:1) recorded at temperatures of a) 140, b) 180, c) 220, d) 260 and e) 298 K.

Figure 4.3 shows a variable temperature study of [Cu(II)(**1a**)] recorded at ~40 K intervals from 140 K up to room temperature. At 140 K, the frozen solution consists of a random collection of paramagnets, and this spectrum therefore has a largely axial

profile. As the temperature is increased, the faster tumbling rates of the complexes mean that the four hyperfine lines in the parallel region become indistinguishable, and the spectra recorded at the highest temperatures in fluid solution are therefore of quasi-isotropic symmetry. Information which is valuable to the study of [Cu(II)(BOX)] complexes, such as $g_{1,2,3}$, $A_{1,2,3}$ and superhyperfine resolution is lost when EPR spectra are recorded at room temperature. The EPR spectra presented in this thesis have therefore been recorded at 140 K. It should be noted however that finding a_{iso} and g_{iso} can sometimes be useful to check the assignments of $A\perp$ and $g\perp$.
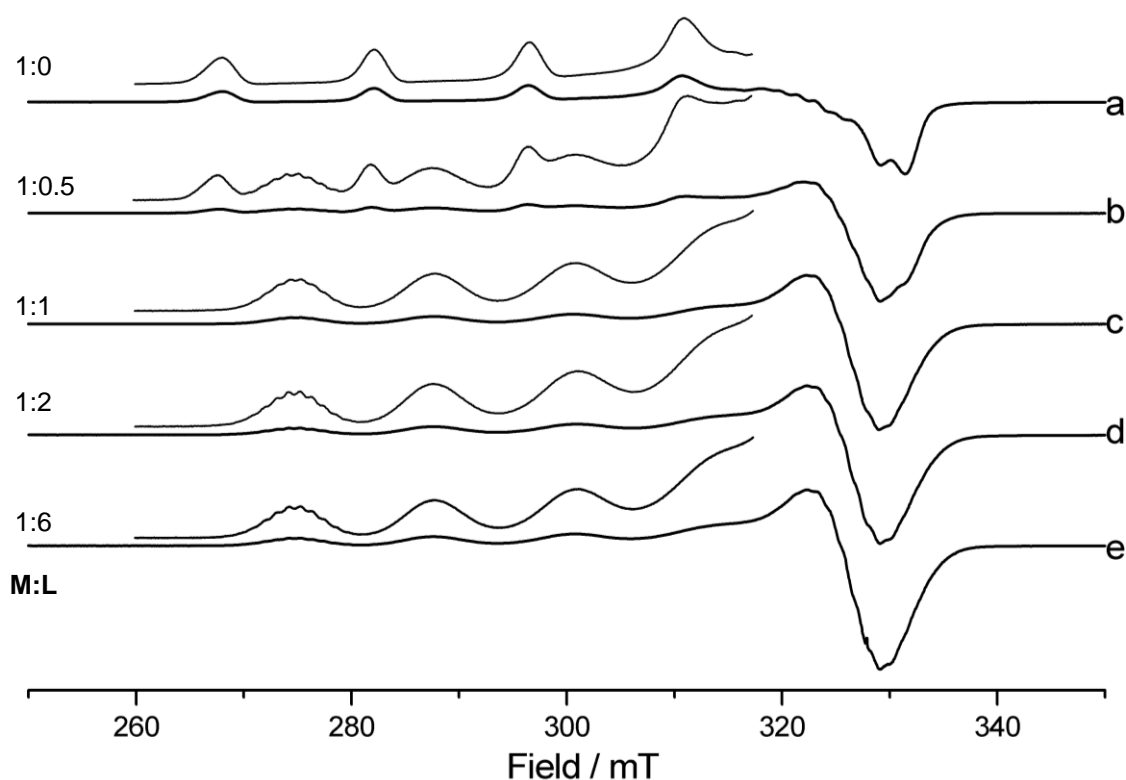
Figure 4.4 *X*-band CW-EPR spectra (140 K) of a) CuCl$_2$ dissolved in DCM:THF (1:1), containing increasing Cu(II):BOX (**1**) ratios (M:L); b) 1:0.5, c) 1:1, d) 1:2 and e) 1:6.

A similar series of EPR spectra to that shown in Figure 4.1 can be observed for the CuCl$_2$ salt after reacting with (**1**) in DCM; see Figure 4.4. Like Cu(OTf)$_2$, (Figure 4.1a), the EPR spectrum of CuCl$_2$ also shows axial symmetry (Figure 4.4a). Simulation of this spectrum (see later) gave the spin Hamiltonian values of $g_1 = g_2 = 2.061$, $g_3 = 2.316$, $A_1 = A_2 = 55$ MHz, and $A_3 = 458$ MHz. At a Cu(II):BOX ratio of 1:0.5, a mixture of both the starting copper salt, CuCl$_2$, and a Cu(II) coordinated BOX complex is again observed (Figure 4.4b). At a Cu(II):BOX ratio of 1:1, only one species is evident; the shift in the spectrum, and the superhyperfine resolution, are both indicative of the formation of a single [Cu(II)(BOX)] complex. In the case of CuCl$_2$, unlike Cu(OTf)$_2$, increasing the Cu(II):BOX ratio further (Figure 4.4d,e) does not lead to any changes in

the shape of the spectrum. In order to understand the structure of the [Cu(II)(BOX)] complexes responsible for the spectra shown in Figures 4.1b-e and 4.4b-e, additional Q-band EPR spectra were performed to aid in the simulations and analysis of the spin Hamiltonian parameters (Figure 4.5).

The Q-band CW-EPR spectra for Cu(OTf)$_2$ and CuCl$_2$ containing different ratios of Cu(II):BOX ligand are given in Figure 4.5 while the corresponding X-band data is given in Figure 4.6, along with the spectra of the starting Cu(OTf)$_2$ and CuCl$_2$ salts for comparison. Since the g-strain effect (explained in Section 2.2.5) is larger at Q-band compared to X-band frequency, the resolution of the hyperfine splitting is lost in the $g_{1,2}$ region of the spectrum, but the advantages of Q-band include improved g-value resolution and better angular selection for ENDOR (refer to Section 2.2.7). The spin Hamiltonian parameters were extracted by simulation of both the X- and Q-band data, and the resulting parameters are listed in Table 4.2.
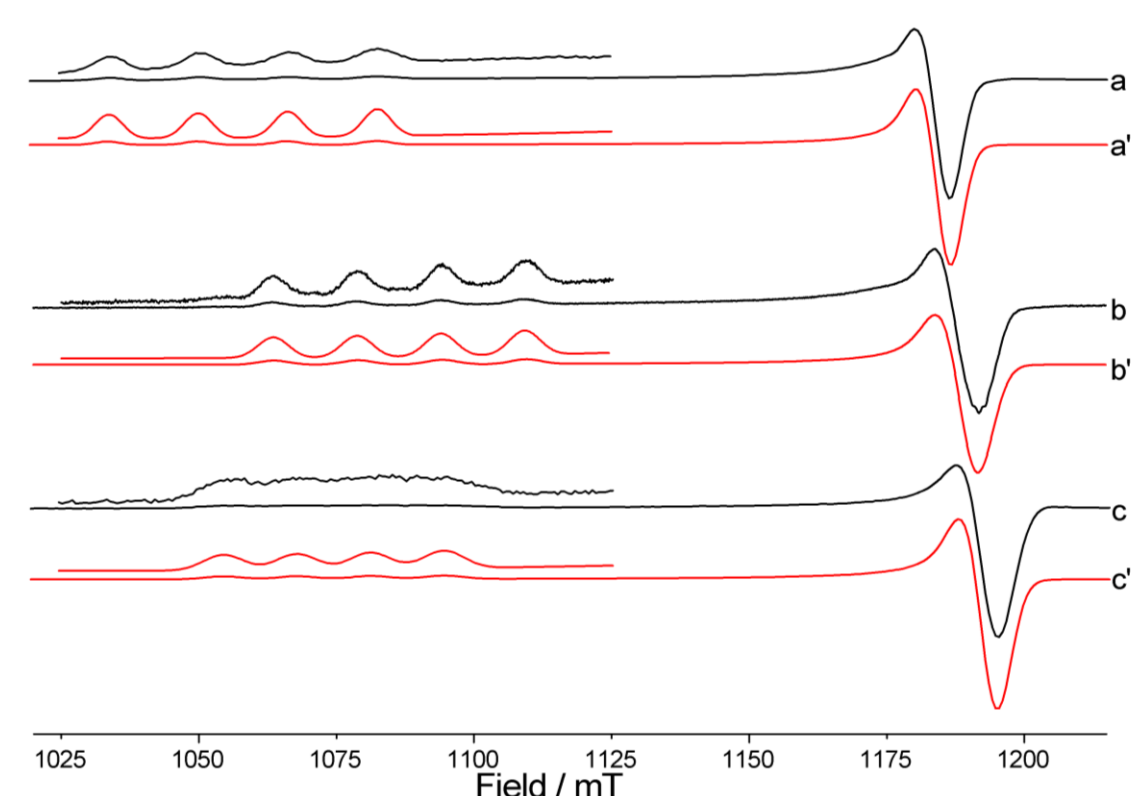
Figure 4.5 Q-band CW-EPR spectra (50 K) of a) [Cu(II)(**1a**)] (Cu(II):BOX ratio 1:1, in THF:DCM), b) [Cu(II)(**1b**)] (Cu(II):BOX ratio 1:6, in AcN:DCM), and c) [Cu(II)(**1c**)] (Cu(II):BOX ratio 1:1, in THF:DCM), The corresponding simulations are given in a'-c' (red line). The expanded parallel region is also shown.

As mentioned above, the g and A^{Cu} tensors for the Cu(OTf)$_2$ and CuCl$_2$ salts are both axially symmetric, and they are largely consistent with previous reports,[33,34] (it should be noted that the profile of these spectra are heavily solvent dependent). These g and A^{Cu} values, given in Table 4.2, are typical for solvated Cu(II) ions. The EPR

spectrum of $CuCl_2$ (Figure 4.6d) contains a series of additional lines in the perpendicular region, which arise from the superhyperfine couplings to weakly interacting solvent molecules.
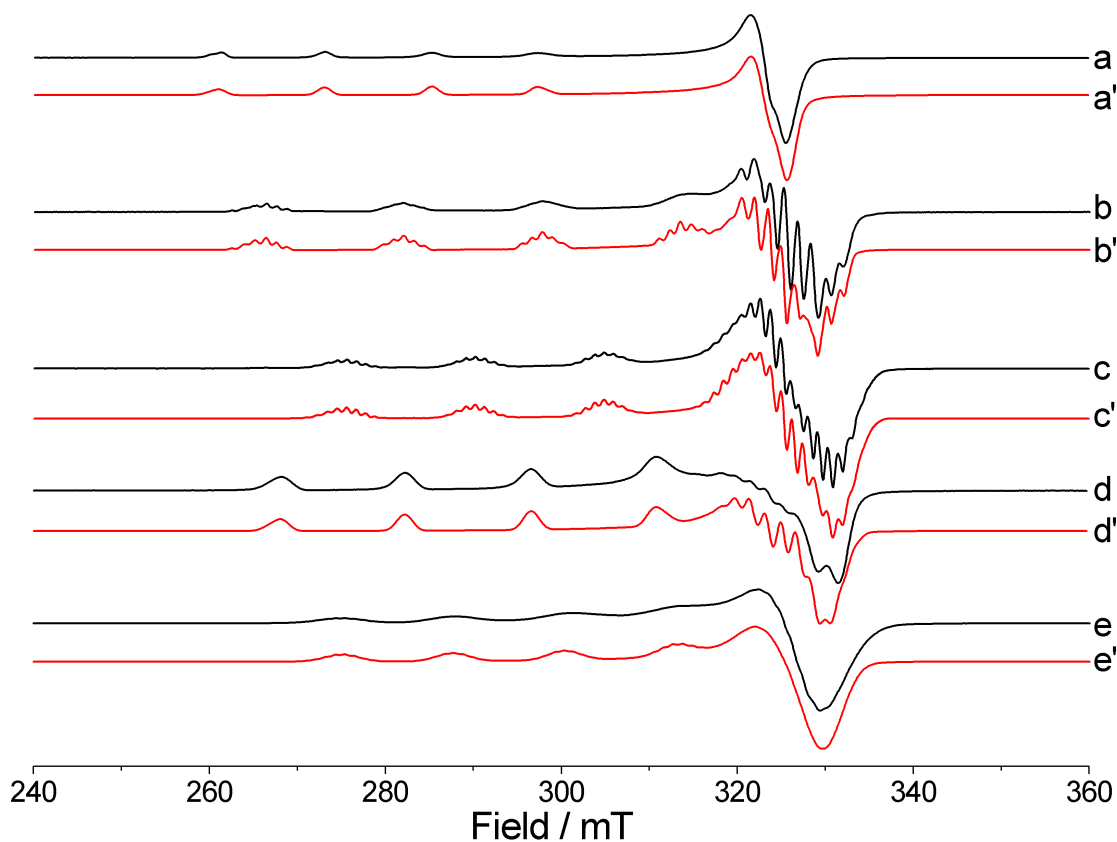
Figure 4.6 *X*-band CW-EPR spectra (140 K) of a) Cu(OTf)$_2$, b) [Cu(II)(**1a**)] (Cu(II):BOX ratio 1:1), c) [Cu(II)(**1b**)] (Cu(II):BOX ratio 1:6), d) CuCl$_2$ and e) [Cu(II)(**1c**)] (Cu(II):BOX ratio 1:1) dissolved in 1:1 THF:DCM. The corresponding simulations are given in a'- e' (red line).
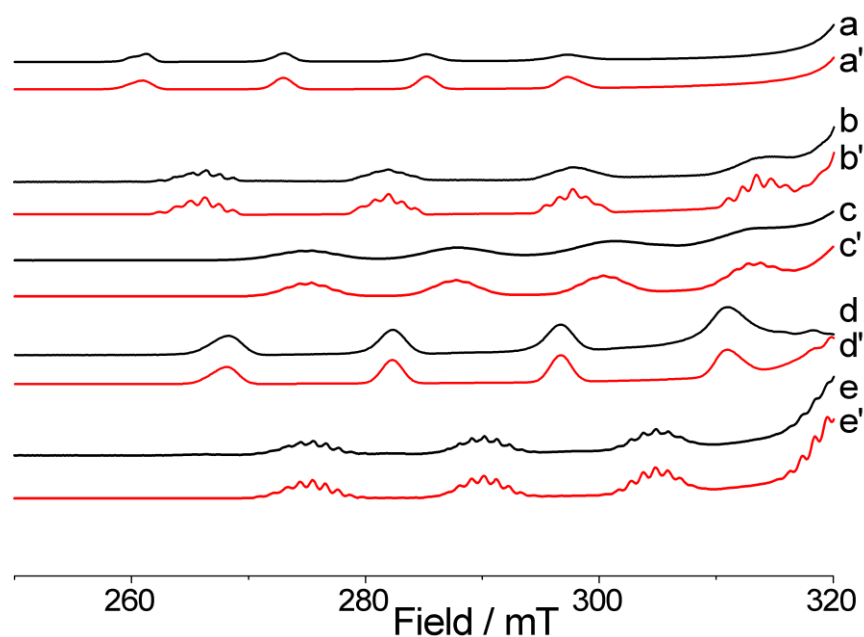
Figure 4.7 *X*-band CW-EPR spectra (140 K) of a) Cu(OTf)$_2$, b) [Cu(II)(**1a**)] (Cu(II):BOX ratio 1:1), c) [Cu(II)(**1b**)] (Cu(II):BOX ratio 1:6), d) Cu(Cl)$_2$ and e) [Cu(II)(**1c**)] (Cu(II):BOX ratio 1:1) dissolved in 1:1 THF:DCM. The corresponding simulations are given in a'- e' (red line). Only the parallel region is shown here to highlight the superhyperfine splitting.

Table 4.2 Experimental (and calculated) g and A^{Cu} spin Hamiltonian parameters for the [Cu(II)(BOX)] complexes [Cu(II)(**1a-c**)] dissolved in THF:DCM.

Complex	$^a g_1$	$^a g_2$	$^a g_3$	$^b A_1$	$^b A_2$	$^c A_3$	^{d}Solvent	^{e}Ref.
Cu(OTf)$_2$	2.083	2.083	2.412	13	13	403	A	T.w.
	-	-	2.44	-	-	372	B	33
CuCl$_2$	2.061	2.061	2.316	55	55	458	A	T.w.
	2.05	2.05	2.34	-	-	336	C	34
[Cu(**1a**)]	2.064	2.073	2.313	15	15	507	A	T.w.
DFT	*2.069*	*2.073*	*2.209*	*-33*	*-45*	*-867*		
[Cu(**1b**)]	2.054	2.063	2.254	26	29	461	A	T.w.
[Cu(**1c**)]	2.057	2.057	2.280	33	33	396	A	T.w.
DFT	*2.062*	*2.064*	*2.204*	*-76*	*-82*	*-765*		

All A values given in MHz; [(a)] ±0.004; [(b)] ±3 MHz; [(c)] ±6 MHz. [(d)]Solvent A: 50% THF, 50% DCM; solvent B = MeOH, solvent C = 58% toluene, 38% chloroform, 4% ethanol. [(e)]T.w. = this work.

The EPR spectra of the [Cu(II)(BOX)] complexes were simulated using slightly rhombic g and A^{Cu} tensors (see Table 4.2). The resolved copper hyperfine splittings are further split due to the hyperfine interaction with two equivalent ^{14}N nuclei in Figure 4.6-7b,e and four equivalent ^{14}N nuclei in Figure 4.6-7c. The g values used in the simulation were extracted more accurately from the Q-band spectra (Figure 4.5). Although the $g_{1,2}$ regions of the X-band spectra are particularly complex, since the Cu and ^{14}N hyperfine couplings are of similar magnitude, accurate ^{14}N couplings were determined *via* the ENDOR measurements (see later) and these parameters were used in the EPR simulations.

The g_3 / A_3 values of Cu(II) complexes possessing a $d_{x^2-y^2}$ or a d_{xy} ground state, are usually diagnostic of the coordinating environment.[32,35] Therefore the g_3 / A_3 values of 2.313 / 507 MHz and 2.280 / 396 MHz for the complexes responsible for Figure 4.6b,e respectively, coupled with the observed hyperfine splittings from two equivalent ^{14}N, are consistent with the presence of the heteroleptic complexes labelled [Cu(II)(BOX)](OTf)$_2$ and [Cu(II)(BOX)]Cl$_2$ (*i.e.,* [Cu(II)(**1a**)] and [Cu(II)(**1c**)] in Scheme 4.1). The altered g_3 / A_3 values of 2.254 / 461 MHz for the Cu(II) complex represented by Figure 4.6c, coupled with the four equivalent ^{14}N nuclei clearly resolved in the low field m_I = -3/2 Cu hyperfine line, are consistent with a coordinating environment bearing four equivalent nitrogens. This spectrum therefore provides evidence for the presence of the homoleptic complex [Cu(II)(BOX)$_2$] (*i.e.,* [Cu(II)(**1b**)]

in Scheme 4.1) in solution at the higher Cu(II):BOX ratios. Whilst homoleptic complexes of this type have been isolated, none have been crystallographically characterised.[11]

The spin Hamiltonian parameters determined for the two heteroleptic complexes [Cu(II)(**1a**)] and [Cu(II)(**1c**)] are notably different. This suggests that the counterions (TfO$^-$ and Cl$^-$) must remain coordinated to the Cu(II) centre in solution, in order to alter the observed spin Hamiltonian parameters. Indeed ENDOR spectroscopy reveals the presence of ^{19}F couplings from the TfO$^-$ groups, further confirming the presence of the counterion in the coordination sphere (discussed later). Moreover, the different *g*/*A* values for [Cu(II)(**1a**)] and [Cu(II)(**1c**)] may in part be accounted for by differences in the distortion around the Cu(II) centre caused by the bulky triflate ions relative to the chlorides.

The above EPR results therefore indicate that as the Cu(II):BOX ratio increases, the heteroleptic and subsequently homoleptic [Cu(II)(BOX)] complexes are formed, starting from the Cu(OTf)$_2$ salts (Figure 4.1). The analogous trend is not however observed starting from the CuCl$_2$ salt; regardless of the Cu(II):BOX ratio employed, the homoleptic complex is never formed even when (**1**) is present in excess (Figure 4.4). In other words, the more labile TfO$^-$ counterions are easily displaced when an excess of (**1**) is present in solution, whereas the Cl$^-$ counterions remain more strongly coordinated, preventing coordination of a second BOX ligand.

4.3.2 ^{14}N ENDOR of [Cu(II)(**1a-c**)]

In order to extract the hyperfine and nuclear quadrupole principal values of the ^{14}N nuclei from the bis(oxazoline) ligand, *X*-band Davies ENDOR and *Q*-band CW-ENDOR measurements were conducted. The ENDOR spectra were measured at multiple field positions, for the reasons explained in Section 2.3.4. The observed hyperfine (A_i) and quadrupolar (P_i) parameters are very similar to those reported for other Cu(II) centres bearing strongly coupled N$_4$ or N$_2$O$_2$ donor ligand sets (Table 4.3).[36,37] The experimental spectra and corresponding simulations at the two frequencies for the heteroleptic [Cu(II)(**1a**)] complex are shown in Figure 4.8 (the simulated parameters are listed in Table 4.3).
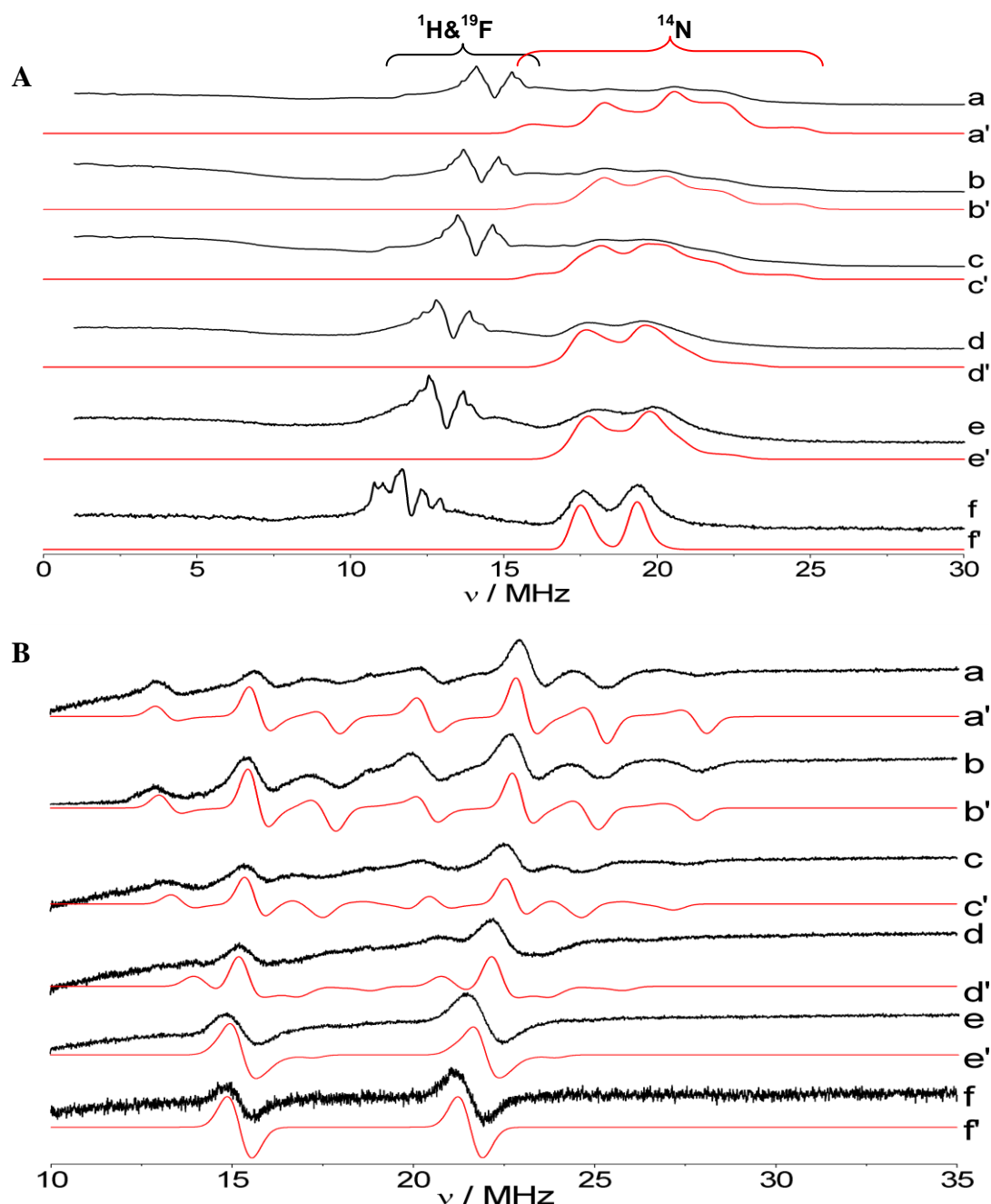
Figure 4.8 (A) *X*-band Davies ENDOR spectra (10 K) of [Cu(II)(**1a**)] recorded at the field positions a) 344.3, b) 334.5, c) 330.0, d) 313.0, e) 307.0 and f) 280.6 mT. (B) *Q*-band ^{14}N CW-ENDOR spectra (10 K) of [Cu(II)(**1a**)] recorded at the field positions a) 1180.4, b) 1176.9, c) 1159.7, d) 1124.4, e) 1080.0 and f) 1030.8 mT. The corresponding simulations (for ^{14}N only) are given in a' – f' (red line). All spectra recorded in THF:DCM (1:1).

The *X*-band Davies ENDOR spectra were obtained using soft microwave (*mw*) pulses and therefore contain overlapping contributions from ^{1}H and ^{19}F in addition to the strongly coupled ^{14}N nuclei (Figure 4.8A). Despite variations in the strength of the *mw* pulses (so-called hyperfine selective ENDOR), complete suppression of the ^{1}H peaks could not be achieved, so these spectra remain significantly overlapped.[38] Nevertheless the *X*-band Davies ENDOR spectra are important in order to observe the

largest ^{14}N couplings which can sometimes be difficult to detect *via* CW-ENDOR. The ^{14}N couplings are in fact extremely well resolved at *Q*-band (Figure 4.8B) enabling the angular selective data to be simulated more accurately (Table 4.3). The hyperfine and quadrupolar coupling from the [14]N ($I = 1$) nuclei in the [Cu(II)(**1a**)] complex was found to deviate slightly from axial symmetry and the largest principal axis was approximately directed to the copper ion.

The relevant ENDOR spectra for the [Cu(II)(**1b**)] complex are given in Figure 4.9, recorded at the perpendicular and parallel field positions. It is evident that this is a much weaker signal than for the equivalent spectra of [Cu(II)(**1a**)] (Figure 4.8Ba,f), and this is due to the greater electron distribution over the Cu(II) centre, due to the electron withdrawing effect of four coordinated nitrogen atoms as opposed to two coordinated nitrogen atoms in [Cu(II)(**1a**)]. Again, the hyperfine and quadrupolar coupling from the [14]N ($I = 1$) nuclei in the [Cu(II)(**1b**)] showed a slight deviation from axial symmetry.
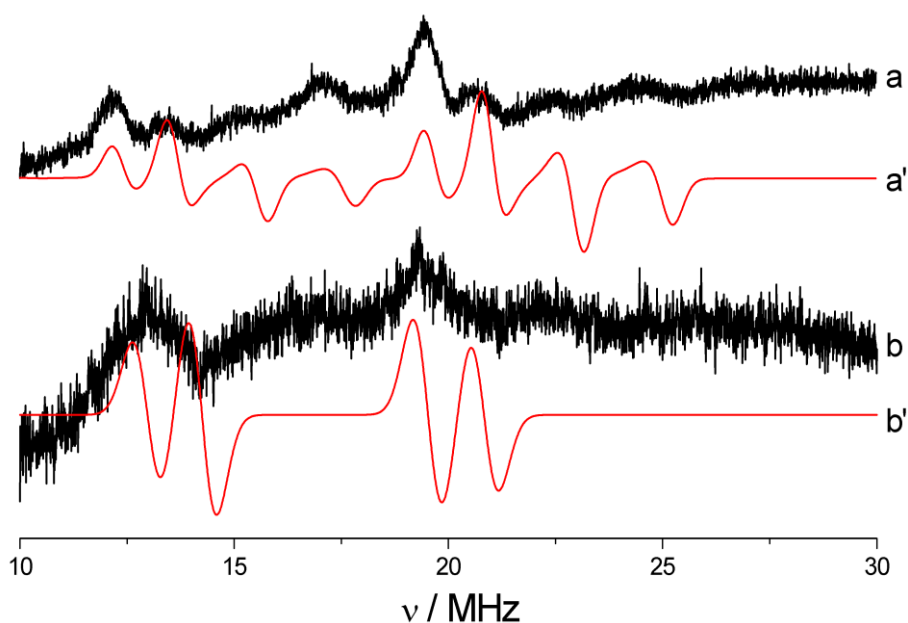
Figure 4.9 CW ^{14}N ENDOR spectra (10 K) of [Cu(II)(**1b**)] recorded at the field positions corresponding to a) $g = g_\perp$ and b) $g = g_\parallel$. The corresponding simulations are given in a' and b' (red line).

Finally, the *Q*-band ^{14}N CW-ENDOR spectra of [Cu(II)(**1c**)] are shown in Figure 4.10. There is again a small degree of rhombicity in the ^{14}N hyperfine and quadrupole parameters for this complex. Comparing the ^{14}N ENDOR spectra of this heteroleptic complex to the heteroleptic [Cu(II)(**1a**)], the change from TfO[-] to Cl^{-} has resulted in a decrease in the ^{14}N hyperfine values.
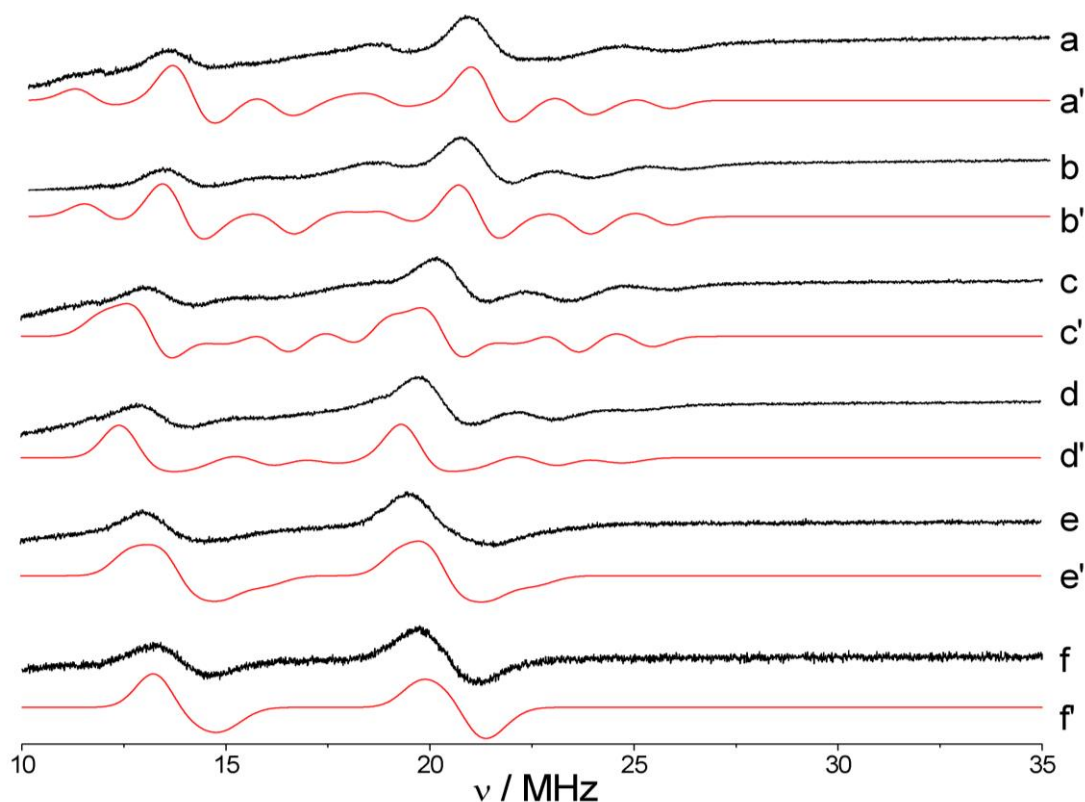
Figure 4.10 Q-band ^{14}N CW-ENDOR spectra (10 K) of [Cu(II)(**1c**)] recorded at the field positions a) 1189.2, b) 1179.2, c) 1159.2, d) 1130.6, e) 1073.5, and f) 1056.3 mT. The corresponding simulations are given in a' – f'.

Table 4.3 ^{14}N hyperfine and quadrupole parameters for bis(oxazoline) nitrogens in the [Cu(II)(**1a-c**)] complexes. For comparison the ^{14}N parameters for Cu(II) in an N_2O_2 (Cu-Salen)[36] and N_4 (Cu-porphyrin = CuPc)[37] coordinating ligand environment are also given.

Complex	$^{(a)}A_1$	A_2	A_3	$^{(b)}P_1$	P_2	P_3	$^{(c)}e^2qQ/h$	$^{(d)}\eta$
[Cu(Salen)]	50.5	37.4	38.5	-1.15	0.70	0.45	-2.3	0.2
[CuPc]	56.4	44.8	45.7	-0.79	0.82	0.03		
[Cu(**1a**)]	45.6	35.9	36.7	-0.87	0.97	-0.10	1.94	0.79
[Cu(**1b**)]	39.8	33.1	32.9	-0.57	0.52	0.05		
[Cu(**1c**)]	41.9	32.5	32.8	-0.72	0.99	-0.27	1.98	0.45

All values are given in MHz; $^{(a)}$ ±0.2 MHz; $^{(b)}$ ±0.1 MHz; $^{(c)}$ ±0.2 MHz; $^{(d)}$ ±0.1

Whilst the quadrupolar ^{14}N parameters are similar for the two heteroleptic complexes, [Cu(II)(**1a**)] and [Cu(II)(**1c**)], the hyperfine parameters are slightly different in each case. These differences in $^{N}A_i$ are consistent with the earlier variations noted in the $g/^{Cu}A$ values by EPR (Section 4.3.1) and again suggest a slightly different degree of distortion in the Cu(II)-N_2 plane. An even larger difference in hyperfine (A_i) and quadrupolar (P_i) parameters is observed between the homoleptic ([Cu(II)(**1b**)]) and heteroleptic ([Cu(II)(**1a**)]) complexes (Table 4.3). In particular, the $^{N}A_i$ and $^{N}P_i$

parameters are smaller in the homoleptic complex (Table 4.3), and this is entirely consistent with the redistribution of the unpaired spin density in the Cu(II)-N_4 complex compared to the Cu(II)-N_2 complex.

4.3.3 ^{1}H and ^{19}F ENDOR of [Cu(II)(1a-c)]

The hyperfine couplings to the proton and fluorine nuclei of the complexes were well resolved by ENDOR at Q-band. The spectra recorded at the principal turning points ($g=g_\parallel$ and $g=g_\perp$) for [Cu(II)(1a-c)] are shown in Figure 4.11. Owing to the similarities in v_n for ^{1}H and ^{19}F (i.e., $v_n(^1H) = 14.90218$, $v_n(^{19}F) = 14.02721$) at Q-band, the peaks appear at similar positions in the ENDOR spectra.
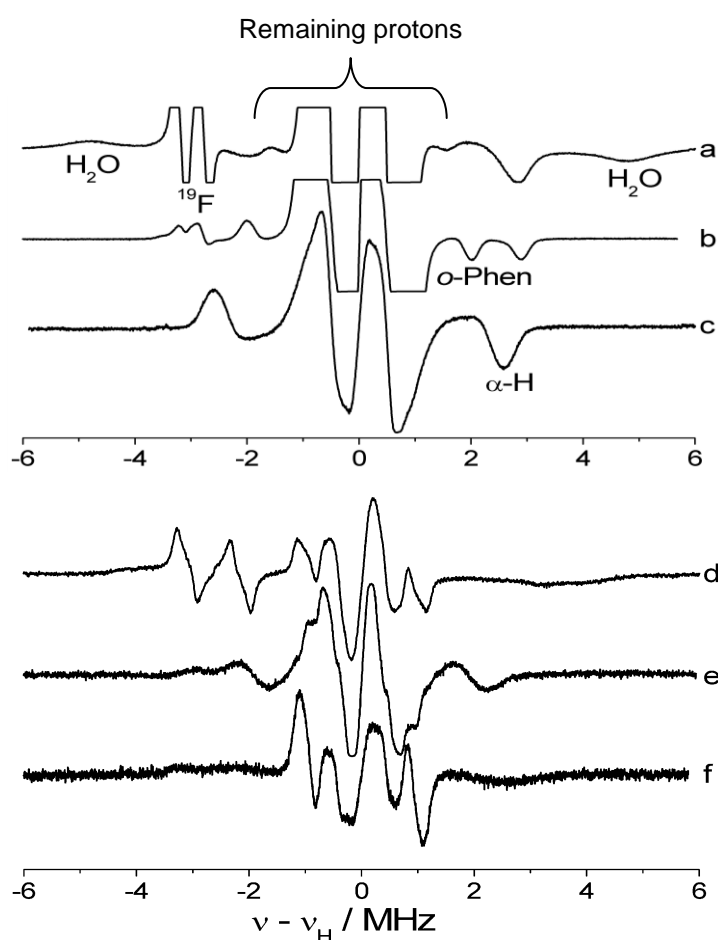
Figure 4.11 Q-band ^{1}H CW-ENDOR spectra (10 K) of a,d) [Cu(II)(1a)] (THF:DCM (1:1)), b,e) [Cu(II)(1b)] (AcN:DCM (1:1)) and c,f) [Cu(II)(1c)] (AcN:DCM (1:1)). The spectra were recorded at the field positions corresponding to: a,b,c) $g = g_\perp$ and d,e,f) $g = g_\parallel$.

The presence of a weakly coupled ^{19}F nucleus in [Cu(II)(1a)] is evident in Figure 4.11a,d, and this must arise from coordinated TfO$^-$ groups. By comparison, in the homoleptic complex [Cu(II)(1b)], only a matrix ^{19}F peak centred on v_n for fluorine, is observed (Figure 4.11b,e) and this emanates from remote (non-coordinated) TfO$^-$ ions

in the surrounding solvent. The small ^{19}F couplings in [Cu(II)(**1a**)] produced a well resolved spectrum which was simulated at multiple field positions in order to extract the ^{19}F hyperfine parameters (Figure 4.12, Table 4.5). The resulting ^FA hyperfine parameters are given in Table 4.5. Analysis of the ^FA data using a simple point-dipole approximation suggests a Cu...^{19}F distance of *ca.* 7.78 Å based on a dipolar coupling of 0.32 MHz. Furthermore the largest contribution to this coupling was observed along the $g=g_\parallel$ direction with an angle of $\theta_H=0°$ (angle between g_3 and B_r (where B_r is the resonance field value)), consistent with the TfO$^-$ groups coordinating along the axial position of the Cu(II) complex (orthogonal to the Cu-N$_2$ plane). This picture is in fact consistent with the crystal structure of [Cu(II)(**1**)](OTf)$_2$(H$_2$O)$_2$ reported by Evans *et al.*,[23] where the triflate groups were also oriented along the axial position. However the reported Cu...^{19}F distances varied from 4.834 – 6.049 Å in the crystal structure,[23] compared to the much longer 7.78 Å estimated by ENDOR. This large discrepancy must arise from the differences in counterion positioning in the solid state single crystal compared to the solvated complex in frozen solution, as measured by ENDOR; the presence of solvent molecules may then cause the Cu...TfO$^-$ distance to increase. The limitations of the point-dipole approximation is also likely to contribute towards this discrepancy.
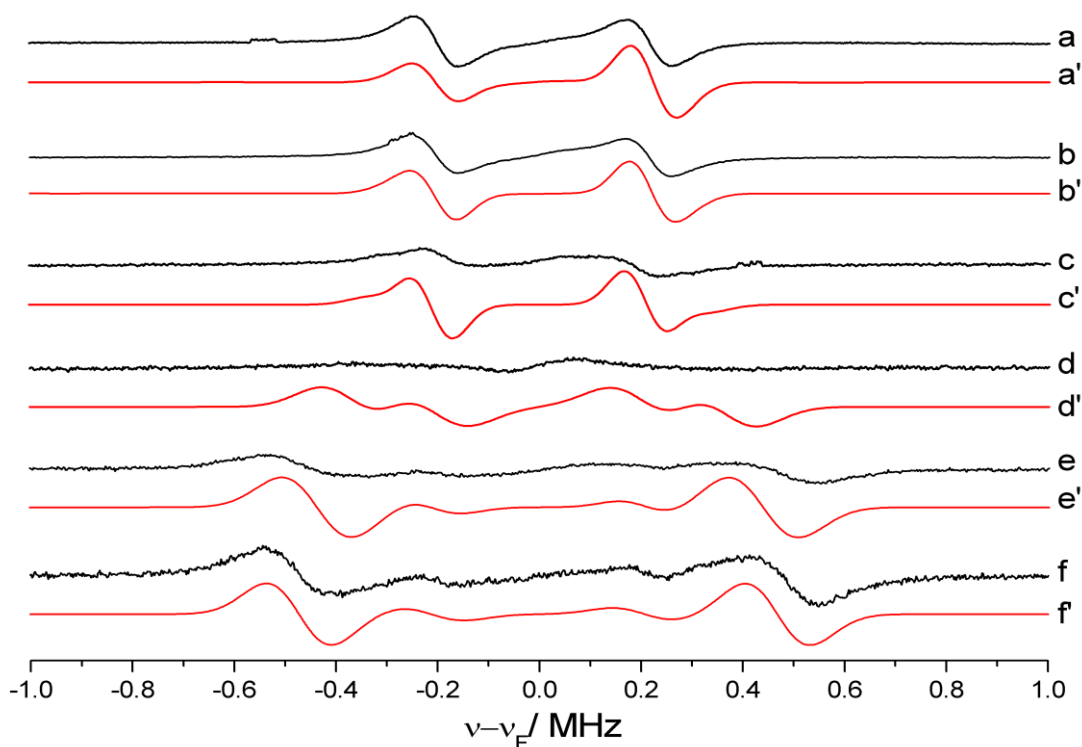
Figure 4.12 *Q*-band ^{19}F CW-ENDOR (10 K) of [Cu(II)(**1a**)] dissolved in THF:DCM (1:1) recorded at the field positions a) 1180.4, b) 1176.9, c) 1159.7, d) 1124.4, e) 1080.0 and f) 1030.8 mT. The corresponding simulations are given in a' – f' (red line).

A recent private communication by Umamaheswari *et al.*,[39] probed the [Cu(II)(*tert*-Bu-BOX)](OTf)$_2$ complex using a *tert*-butyl BOX ligand (2,2'-isopropylidenebis[(4*S*)-4-*tert*-butyl-2-oxazoline]). This communication aimed to explore the [Cu(II)(*tert*-Bu-BOX)](OTf)$_2$ catalysed stereoselective hetero Diels-Alder reaction between ethyl glyoxylate and cyclohexadiene. CW-EPR, pulsed EPR, ENDOR and HYSCORE were utilised to observe the step-by-step reaction. It is interesting to note that the ^{19}F hyperfine tensors calculated for that complex are very different to those calculated in this work for [Cu(II)(**1a**)] (shown in Table 4.5). Table 4.4 shows the findings of Umamaheswari *et al.*,[39] for the ^{19}F of the triflate counterions.

Table 4.4 Experimental and calculated ^{19}F EPR parameters used for the determination of the geometry of the [Cu(II)(*tert*-Bu-BOX)](OTf)$_2$ studied by Umamaheswari *et al.*[39]

	$A\perp$/ MHz		$A_\parallel$/MHz		A_{iso}/MHz	
	Exp.	Calc.	Exp.	Calc.	Exp.	Calc.
^{19}F1	-2.23	-1.04	7.16	5.63	0.9	1.42
^{19}F2	-2.30	-1.14	2.80	1.28	-0.6	-0.12

The Cu…^{19}F distances calculated by Umamaheswari *et al.*,[39] from their experimental EPR results using the point-dipole approximation were 3.08 Å and 3.77 Å. These are significantly different from the Cu…^{19}F distance of 7.78 Å for [Cu(II)(**1a**)]. This suggests that the orientation of the ^{19}F (TfO$^-$) is substantially different in these complexes, despite the only difference being the oxazoline ring substituent.

The crystal structure of [Cu(II)(**1**)](OTf)$_2$(H$_2$O)$_2$ (reported by Evans) notably contains two coordinated water molecules in the equatorial position.[23] This is also consistent with the current ENDOR data for [Cu(II)(**1a**)] which reveals the presence of strongly coupled protons, suggesting that there must be a large isotropic contribution to the hyperfine. These couplings are too large to arise from the ligand, due to there being a minimum of three bonds between the Cu(II) centre and the ligand protons. These large couplings must therefore originate from bound water molecules. A large coupling of *ca.* 10 MHz is observed in the experimental spectrum (Figure 4.11a; $g=g_\perp$ position) which was not observed in either the homoleptic complex [Cu(II)(**1b**)] or in the heteroleptic complex formed from the CuCl$_2$ salt, [Cu(II)(**1c**)] (Figure 4.11b,c; $g=g_\perp$ position). The preparation of complex [Cu(II)(**1a**)] was then performed under rigorous anhydrous and anaerobic conditions, in order to suppress or eliminate the H$_2$O derived peaks from the ENDOR spectra. The resulting ENDOR spectra at the perpendicular and parallel field positions are shown in Figure 4.13. Although a small suppression was observed, the

H$_2$O peaks could not be completely eliminated. This indicates that [Cu(II)(**1**)](OTf)$_2$ prepared 'on the bench' using commercially available Cu(OTf)$_2$, is always likely to contain some coordinated water in solution. It should also be noted that additional proton peaks can be observed in both spectra; this is due to the use of protic THF rather than deuterated THF due to restrictions resulting from the anaerobic conditions of this experiment.
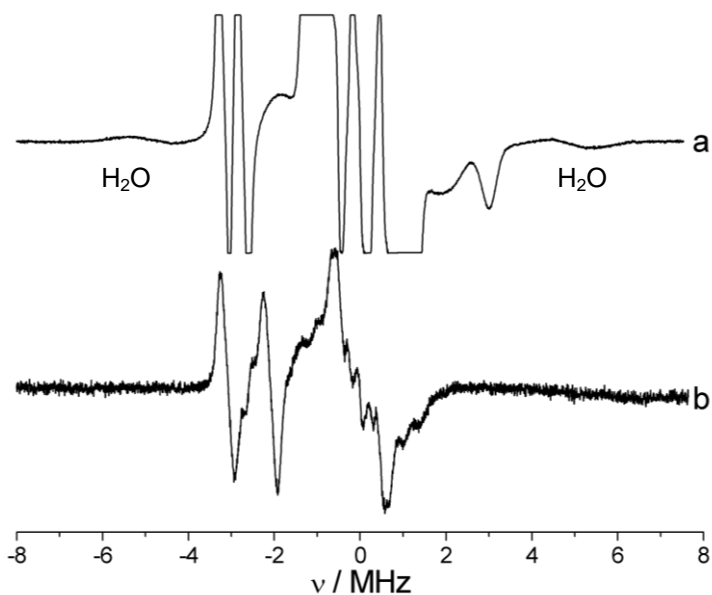
Figure 4.13 Q-band ^{1}H CW-ENDOR spectra (10 K) of [Cu(II)(**1a**)] synthesised *in-situ* and recorded in dry protic THF:d^2-DCM (1:1). The spectra were recorded in anaerobic conditions at the field positions corresponding to: a) $g = g_\perp$ and b) $g = g_\parallel$.

The large couplings assigned to the bound water molecules in Figure 4.11a (also evident in Figure 4.13), were simulated at multiple field positions and the resulting angular selective simulations are given in Figure 4.14. Owing to the close proximity of the H$_2$O to the Cu(II) centre (Cu…H$_{H_2O}$ distance of 2.410 Å from the crystal structure), a large a_{iso} contribution is expected (Table 4.5). Furthermore, analysis of the experimental hyperfine tensor suggests a Cu…H$_{H_2O}$ distance of 2.52 Å ($A_{dipolar}$ = 11 MHz), which is in reasonable agreement with the crystal structure.

The remaining proton couplings observed in the ENDOR spectra (Figures 4.11 and 4.14) arise from the BOX ligand nuclei. In particular the nearest neighbour protons which interact with Cu(II) arise from the α-H at the asymmetric carbon of the BOX ring (labelled * in Scheme 4.1), with a Cu…α-H$_{BOX}$ distance of 3.185 Å, and from the *ortho*-^{1}H of the phenyl ring, with a Cu…*o*-H$_{phenyl}$ distance of 4.001 Å (X-ray distances). These two protons are most likely responsible for the observed couplings at A_1 = 3.0 MHz and

5.9 MHz in Figure 4.11a-c. The principal hyperfine values for the α-H are given in Table 4.5, with an estimated Cu…α-H$_{BOX}$ distance of 3.18 Å, in good agreement with the X-ray data. Unfortunately, owing to the overlapping features with the more remote protons from the BOX ligand, a reliable estimation of the $A_{2,3}$ components of the o-H$_{phenyl}$ is not possible, hence the large difference in Cu…o-H$_{phenyl}$ distances between the ENDOR data versus the X-ray data (Table 4.5).
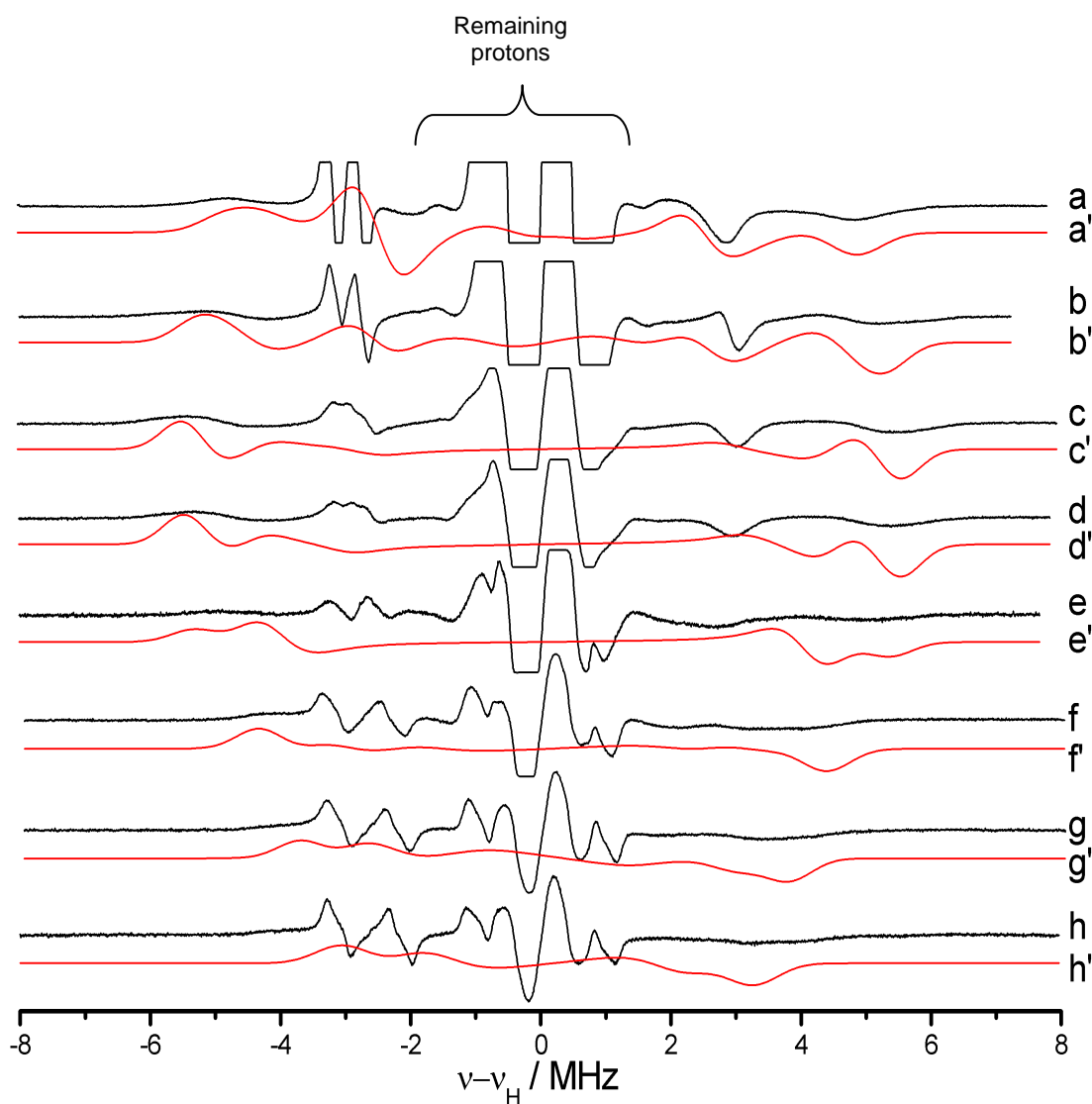
Figure 4.14 Q-band ^{1}H CW-ENDOR (10 K) of [Cu(II)(**1a**)] dissolved in THF:DCM (1:1) recorded at the field positions a) 1180.4, b) 1170.2, c) 1159.7, d) 1138.0, e) 1124.4, f) 1080.0, g) 1051.1 and h) 1030.8 mT. The corresponding simulations (showing only the H$_2$O peaks) are given in a' – h' (red line).

Table 4.5 ^{1}H and ^{19}F principal hyperfine values for [Cu(II)(**1a**)]. The DFT calculated parameters are also given.

		$^aA_1$	$^aA_2$	$^bA_3$	a_{iso}	$'\alpha$	$'\beta$	$^c\gamma$	$A_\parallel$	R / Å ENDOR	R / Å X-ray
^{19}F		0.49	0.49	0.98	0.65			0	0.32	7.78	4.834
^{1}H$_2$O	Expt	-10.8	-5.02	8.6	-2.41	20	38	0	11.01	2.52	2.410
	DFT	-12.01	+9.11	-5.82	-2.90	20	30	20			
α-^{1}H	Expt	-2.1	-1.7	5.9	0.7	11	63	34	5.20	3.18	3.185
	DFT	-1.98	-0.97	5.57	0.87	11	63	34			
o-^{1}H$_{Phen}$	Expt	-3.0	-1.20^d	1.20^d	-1.0	0	11	0	2.20	4.36	4.001
	DFT	2.47	-1.31	-1.19	-0.01	-21.0	38	24			

All values are given in MHz; [a] ±0.2 MHz; [b] ±0.1 MHz; [c] ± 10º; [d] ±0.5 MHz.

4.3.4 DFT calculations

The spin Hamiltonian parameters were also calculated for the [Cu(II)(**1a**)] and [Cu(II)(**1c**)] complex in order to compare to the experimental data. The calculations were performed using the ORCA package,[40-43] using the atomic coordinates from the reported crystal structures of [Cu(II)(**1**)](OTf)$_2$(H$_2$O)$_2$[23] and [Cu(II)(**1**)](Cl)$_2$.[8] Images of the X-ray structures are shown in Figure 4.15.[8,23]
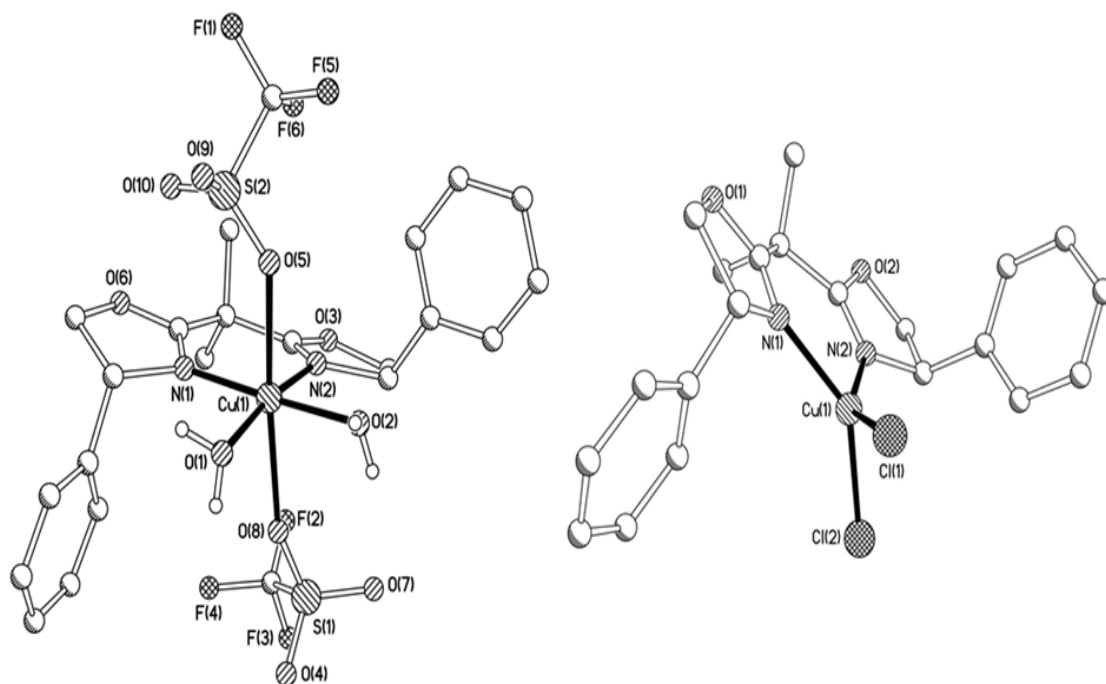
Figure 4.15 Molecular structures of [Cu(II)(**1**)](OTf)$_2$(H$_2$O)$_2$ and [Cu(II)(**1**)]Cl$_2$ complexes. H atoms omitted for clarity.

The relevant EPR parameters are listed in Tables 4.2 and 4.5. Current state-of-the-art DFT methods still struggle to reproduce accurately the *g* and metal hyperfine values for the transition metal ions,[44] hence the discrepancy between the experimental and calculated g/^{Cu}A values in Table 4.2. Nevertheless, the general trends are in good agreement with each other. In particular the decrease in g_3 and A_3 observed experimentally upon complex formation is satisfactorily reproduced in the computations. Indeed, the structure of the [Cu(II)(**1**)](Cl)$_2$ complex used in the calculation was found to have a slight twisted arrangement around the Cu-N$_2$Cl$_2$ plane, in agreement with the earlier EPR observations.

Ligand hyperfine parameters are more reliably determined by DFT, particularly for weakly coupled protons (Table 4.5). As expected, the coordinated H$_2$O molecules are predicted to produce the largest couplings, and these values are in good agreement with the experimental ENDOR data. The α-H and *ortho*-phenyl protons of the BOX

ligand also produce appreciable hyperfine couplings (Table 4.5). Although the $A_{1,2}$ couplings of these protons could not be confidently extracted from the powder ENDOR spectra, the largest calculated A_1 component agrees well with the experimental values (Table 4.5).

4.4 Conclusion

In the current chapter, a detailed EPR and ENDOR investigation of a series of heteroleptic and homoleptic copper-bis(oxazoline) complexes, labelled [Cu(II)(**1a-c**)], has been presented. The geometry of the hetereoleptic complexes [Cu(II)(**1a**)] and [Cu(II)(**1c**)] is dependent on the choice of counterion used in the synthesis, since different $g/^{Cu}A$ parameters are observed by EPR. The geometry is closely linked to the resulting catalytic activity, and this work reveals the potential of EPR to study such complexes in solution. The homoleptic complex [Cu(II)(**1b**)] was only formed using an excess of the BOX ligand (**1**) in the presence of the Cu(OTf)$_2$ salt; the CuCl$_2$ salt prevented the coordination of a second bis(oxazoline) ligand. The hyperfine technique of ENDOR enabled the hyperfine and quadrupole parameters of the surrounding nuclei to be determined. Significant differences were observed in the ^NA values for [Cu(II)(**1a**)] and [Cu(II)(**1c**)], consistent with the more distorted arrangement in the latter complex, whereas smaller ^NA and ^NP values were detected for [Cu(II)(**1b**)] attributed to the redistributed spin density in the homoleptic complex. Well resolved ^{19}F couplings in [Cu(II)(**1a**)] confirmed the presence of coordinated TfO$^-$ counterions along the axial direction, while strong ^{1}H couplings from bound water molecules along the equatorial direction were also observed for this complex. These results reveal how the inner- and indeed outer-sphere coordination environment of [Cu(II)BOX] complexes, of relevance to catalysis, can be studied by EPR and ENDOR in the 'solvated' environment where counterion effects are still manifested.[45]

4.5 References

1   Evans, D. A.; Miller, S. J.; Lectka, T. *Journal of the American Chemical Society,* **1993**, *115*, 6460.

2   Johannsen, M.; Anker Jørgensen, K. *Journal of the Chemical Society, Perkin Transactions 2,* **1997**, 1183.

3   Evans, D. A.; Miller, S. J.; Lectka, T.; Von Matt, P. *Journal of the American Chemical Society,* **1999**, *121*, 7559.

4   Evans, D. A.; Barnes, D. M.; Johnson, J. S.; Lectka, T.; Von Matt, P.; Miller, S. J.; Murry, J. A.; Norcross, R. D.; Shaughnessy, E. A.; Campos, K. R. *Journal of the American Chemical Society,* **1999**, *121*, 7582.

5   Evans, D. A.; Johnson, J. S.; Burgey, C. S.; Campos, K. R. *Tetrahedron Letters,* **1999**, *40*, 2879.

6   Evans, D. A.; Johnson, J. S.; Olhava, E. J. *Journal of the American Chemical Society,* **2000**, *122*, 1635.

7   Aggarwal, V. K.; Jones, D. E.; Martin-Castro, A. M. *European Journal of Organic Chemistry,* **2000**, *2000*, 2939.

8   Thorhauge, J.; Roberson, M.; Hazell, R. G.; Jorgensen, K. A. *Chemistry - A European Journal,* **2002**, *8*, 1888.

9   Landa, A.; Richter, B.; Johansen, R. L.; Minkkilä, A.; Jørgensen, K. A. *The Journal of Organic Chemistry,* **2006**, *72*, 240.

10   Tanaka, S.; Tada, M.; Iwasawa, Y. *Journal of Catalysis,* **2007**, *245*, 173.

11   Lowenthal, R. E.; Abiko, A.; Masamune, S. *Tetrahedron Letters,* **1990**, *31*, 6005.

12   Evans, D. A.; Woerpel, K. A.; Hinman, M. M.; Faul, M. M. *Journal of the American Chemical Society,* **1991**, *113*, 726.

13   Harm, A. M.; Knight, J. G.; Stemp, G. *Tetrahedron Letters,* **1996**, *37*, 6189.

14   Fernández, M. J.; Fraile, J. M.; García, J. I.; Mayoral, J. A.; Burguete, M. I.; García-Verdugo, E.; Luis, S. V.; Harmer, M. A. *Topics in Catalysis,* **2000**, *13*, 303.

15   Evans, D. A.; Faul, M. M.; Bilodeau, M. T.; Anderson, B. A.; Barnes, D. M. *Journal of the American Chemical Society,* **1993**, *115*, 5328.

16   Langham, C.; Piaggio, P.; McMorn, P.; Willock, D. J.; Hutchings, G. J.; Bethell, D.; Lee, D. F.; Bulman Page, P. C.; Sly, C.; Hancock, F. E.; King, F. *Chemical Communications,* **1998**, 1601.

17   Langham, C.; Bethell, D.; Lee, D. F.; McMorn, P.; Bulman Page, P. C.; Willock, D. J.; Sly, C.; Hancock, F. E.; King, F.; Hutchings, G. J. *Applied Catalysis A: General,* **1999**, *182*, 85.

18   Evans, D. A.; Woerpel, K. A.; Scott, M. J. *Angewandte Chemie,* **1992**, *104*, 439.

19   Fraile, J. M.; García, J. I.; Mayoral, J. A.; Tarnai, T. *Journal of Molecular Catalysis A: Chemical,* **1999**, *144*, 85.

20   Fraile, J. M.; García, J. I.; Mayoral, J. A. *Coordination Chemistry Reviews,* **2008**, *252*, 624.

21   Bolm, C.; Martin, M.; Gescheidt, G.; Palivan, C.; Stanoeva, T.; Bertagnolli, H.; Feth, M.; Schweiger, A.; Mitrikas, G.; Harmer, J. *Chemistry - A European Journal,* **2007**, *13*, 1842.

22   Jørgensen, K. A.; Johannsen, M.; Yao, S.; Audrain, H.; Thorhauge, J. *Accounts of Chemical Research,* **1999**, *32*, 605.

23   Evans, D. A.; Burgey, C. S.; Paras, N. A.; Vojkovsky, T.; Tregay, S. W. *Journal of the American Chemical Society,* **1998**, *120*, 5824.

24   Evans, D. A.; Kozlowski, M. C.; Burgey, C. S.; MacMillan, D. W. C. *Journal of the American Chemical Society,* **1997**, *119*, 7893.

25   Alonso, P. J.; Fraile, J. M.; García, J.; García, J. I.; Martínez, J. I.; Mayoral, J. A.; Sánchez, M. C. *Langmuir,* **2000**, *16*, 5607.

26   Traa, Y.; Murphy, D. M.; Farley, R. D.; Hutchings, G. J. *Physical Chemistry Chemical Physics,* **2001**, *3*, 1073.

27   Caplar, V.; Raza, Z.; Roje, M.; Tomisic, V.; Horvat, G.; Pozar, J.; Piantanida, I.; Zinic, M. *Tetrahedron,* **2004**, *60*, 8079.

28   Bolm, C.; Martin, M.; Gescheidt, G.; Palivan, C.; Neshchadin, D.; Bertagnolli, H.; Feth, M.; Schweiger, A.; Mitrikas, G.; Harmer, J. *Journal of the American Chemical Society,* **2003**, *125*, 6222.

29   Ghosh, A. K.; Mathivanan, P.; Cappiello, J. *Tetrahedron: Asymmetry,* **1998**, *9*, 1.

30   Hager, M.; Wittmann, S.; Schätz, A.; Pein, F.; Kreitmeier, P.; Reiser, O. *Tetrahedron: Asymmetry,* **2010**, *21*, 1194.

31   Le Roux, E.; Merle, N.; Tornroos, K. W. *Dalton Transactions,* **2011**, *40*, 1768.

32   Pilbrow, J. R. *Transition Ion Electron Paramagnetic Resonance*; 1st ed.; Oxford Science Publications, Oxford University Press, **1990**.

33   Niklas, N.; Alsfasser, R. *Dalton Transactions,* **2006**, 3188.

34   Gersmann, H. R.; Swalen, J. D. *The Journal of Chemical Physics,* **1962**, *36*, 3221.

35   Peisach, J.; Blumberg, W. E. *Archives of Biochemistry and Biophysics,* **1974**, *165*, 691.

36   Murphy, D. M.; Caretti, I.; Carter, E.; Fallis, I. A.; Göbel, M. C.; Landon, J.; Doorslaer, S. V.; Willock, D. J. *Inorganic Chemistry,* **2011**, *50*, 6944.

37   Finazzo, C.; Calle, C.; Stoll, S.; Van Doorslaer, S.; Schweiger, A. *Physical Chemistry Chemical Physics,* **2006**, *8*, 1942.

38   Schweiger, A.; Jeschke, G. *Principles of Pulse Electron Paramagnetic Resonance*; Oxford University Press, **2001**.

39   Umamaheswari, V.; Cias, P.; Poppl, A.; Kaupp, M.; Gescheidt, G., *Ligand Spheres in asymmetric hetero Diels-Alder reactions catalyzed by Cu(II) box complexes: Experiment and Modeling (private communication).*

40   Neese, F. *The Journal of Chemical Physics,* **2001**, *115*, 11080.

41   Neese, F. *The Journal of Physical Chemistry A,* **2001**, *105*, 4290.

42   Neese, F. *The Journal of Chemical Physics,* **2003**, *118*, 3939.

43   Neese, F. *The Journal of Chemical Physics,* **2005**, *122*, 034107.

44   Neese, F. *Journal of Biological Inorganic Chemistry,* **2006**, *11*, 702.

45   Owen, M. E.; Carter, E.; Hutchings, G. J.; Ward, B. D.; Murphy, D. M. *Dalton Transactions,* **2012**, *41*, 11085.

Chapter 5

Investigation of the structure of further Cu(II)-bis(oxazoline) derivatives by EPR/ENDOR spectroscopy

5.1 Introduction

Towards the end of the 20th century, bis(oxazoline) (BOX) ligands became so popular for catalysis that some became commercially available. Examples of BOX ligands which are available to purchase are (-)-2,2'-isopropylidenebis[(4S)-4-phenyl-2-oxazoline] (**1**), 2,2'-methylenebis[(4S)-4-phenyl-2-oxazoline] (**2**), and 2,2'-isopropylidenebis[(4S)-4-*tert*-butyl-2-oxazoline (**3**) (shown in Scheme 5.1). These are therefore amongst the most widely studied BOX ligands as reported in the literature (see Chapter 1). A detailed investigation on the role of counterions affecting the structure of Cu(II) complexes of ligand (**1**), as revealed by EPR and ENDOR, was discussed in Chapter 4. Therefore the focus of this chapter will be to examine the structures of the Cu(II) complexes formed with ligands (**2**) and (**3**). A summary of the structures identified by EPR/ENDOR in this chapter are given in Scheme 5.2.
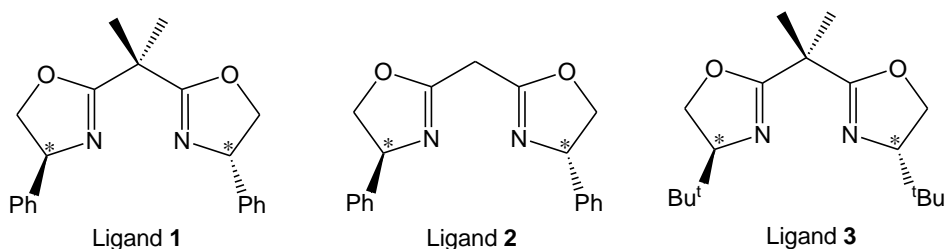
Scheme 5.1 Structures of ligands (**1**), (**2**) and (**3**).

The structure of the BOX ligand is an important factor to be considered when selecting the most suitable ligand for a particular catalytic reaction. As stated in Chapter 1, variations to the bridging carbon atom between the two oxazoline rings have been explored, with adjustments made to the nature, size and flexibility of this backbone.[1] In ligands **1** and **3**, the bridging backbone between the oxazoline rings consists of one carbon coordinated to two methyl groups but in ligand **2** the methyl groups are replaced by protons. Figure 1.5 (Chapter 1) illustrated other variations of bis(oxazoline) ligands, for example ligands in which the oxazoline rings are directly coordinated with no bridging atoms and ligands in which the oxazoline rings are bridged with a pyridine molecule.[1,2]

Another structural variation commonly made to the BOX architecture is to change the substituents at the chiral carbons (labelled with asterisks in Scheme 5.1).

Ligands **1** and **2** are phenyl (Ph) substituted, whilst **3** has tertiary (*tert-*) butyl substituents. Other groups which have been used as substituents are CH$_2$Ph and *i*-Pr, as illustrated earlier in Figure 1.5.[2] It has been shown that the substituents on the oxazoline rings have a direct effect on the stereoselectivity of the catalytic reaction.[3-5]

(S,S)-[Cu(II)(BOX)](OTf)$_2$(H$_2$O)$_2$ [Cu(**2a**)]

(S,S)-[Cu(II)(BOX)$_2$] [Cu(**2b**)]

(S,S)-[Cu(II)(BOX)](Cl)$_2$ [Cu(**2c**)]

(S,S)-[Cu(II)(BOX)](OTf)(H$_2$O)$_2$ [Cu(**3a**)]

(S,S)-[Cu(II)(BOX)$_2$] [Cu(**3b**)]

(S,S)-[Cu(II)(BOX)](Cl)$_2$ [Cu(**3c**)]

(S,S)-[Cu(II)(BOX)](H$_2$O)$_2$ [Cu(**3d**)]
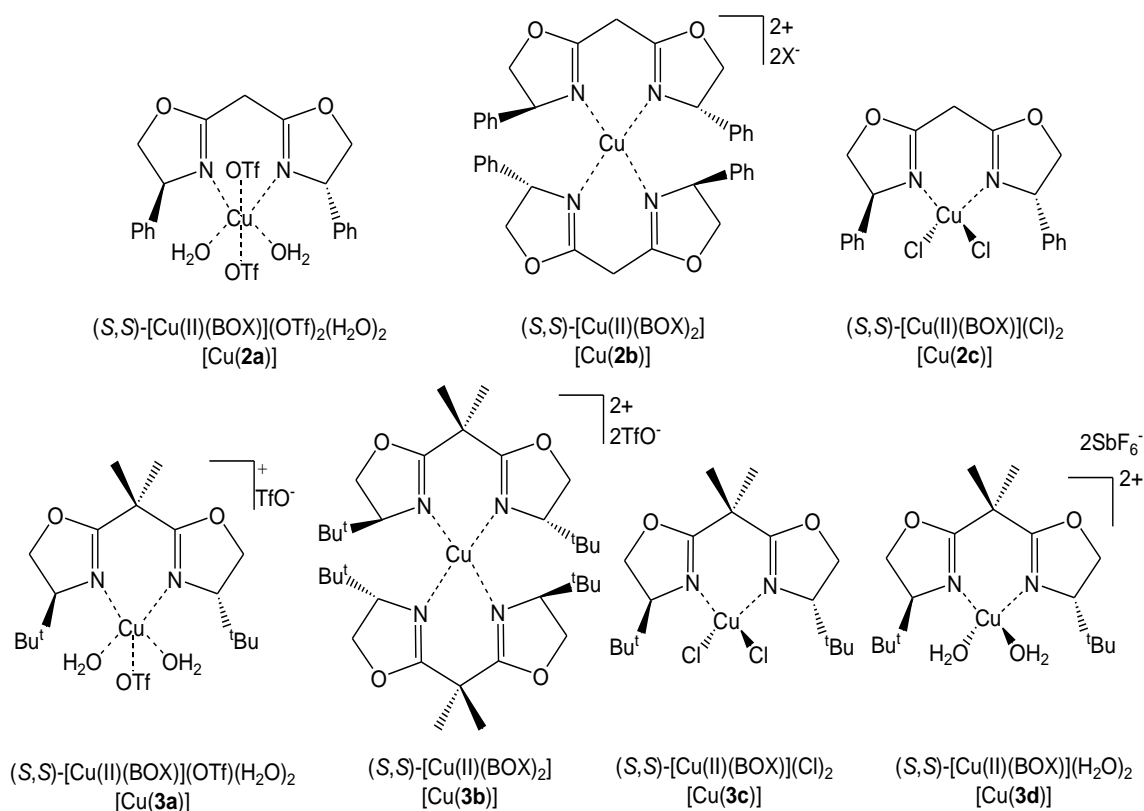
Scheme 5.2 Schematic illustration of the [Cu(II)(**2a-c**)] and [Cu(II)(**3a-d**)] complexes as identified by EPR/ENDOR. For [Cu(**2b**)], X$^-$ = TfO$^-$ or Cl$^-$. The crystal structures reported by Evans *et al.*,[6,7] of [Cu(**3a**)] and [Cu(**3d**)] suggest that counterion/H$_2$O coordination is as illustrated in this Scheme.

In 1995 Johannsen *et al.*,[3] showed that [Cu(II)(BOX)] complexes are very useful in the catalysis of glyoxylate esters with dienes, giving valuable hetero-Diels-Alder and ene products. They found that the absolute chemistry of the reaction is mostly dependent on the phenyl ring substituents. When using a BOX ligand with a *tert*-butyl substituent at the chiral centre, the product of the hetero-Diels-Alder reaction was of the opposite stereochemistry to that of the reaction catalysed with a Ph-BOX ligand.[3] It was proposed that this was due to a geometrical change at the copper atom. The authors suggested that when using the *tert*-butyl-BOX derivative, a planar reaction intermediate was formed, whereas the reaction intermediate had a tetrahedral arrangement at the metal centre when the Ph-BOX was used.[3] Different reaction substrates gave better *ee* results depending on the BOX ligand used. For the *tert*-butyl substituted ligand, methyl

glyoxylate gave the highest *ee* in the hetero-Diels-Alder and ene reactions, whilst for the Ph substituted ligand, isopropyl glyoxylate gave the highest *ee*. Evans *et al*.,[4] reported similar findings in 1999, and endeavoured to fully understand and rationalise this reversal in selectivity. X-ray crystallography was utilised to explore the differences in coordination chemistry between the hydrated Cu(II) complexes of the Ph- and *tert*-butyl- substituted BOX ligands, with SbF_6^- counterions.[4] The most notable difference was in the distortion of the coordinated water molecules. In the *tert*-butyl-substituted bis(aquo) complex, the ligated water molecules were positioned at an average angle of 33º away from the oxazoline substituents, whilst in the analogous Ph-substituted complex, the water molecules were found to tilt towards the oxazoline substituents at an average angle of 9º. They emphasised that this distortion is independent of the counterion and that similar results were found with triflate counterions.[4] Balta *et al*.,[5] also investigated the effect of Ph versus *tert*-butyl substituents, but their work involved computational techniques (DFT), to study the Claisen rearrangement of aliphatic allyl vinyl ethers in the presence of [Cu(II)(BOX)] complexes. They proposed that the enantioselectivity of the *tert*-butyl [Cu(II)(BOX)] complex in this reaction originates from the steric interactions between the substrate and the catalyst, whilst this has less influence on the Ph substituted [Cu(II)(BOX)] complex due to a higher sensitivity to solvent effects.

In addition to differences in enantioselectivities, significant differences in reaction times have been reported, depending on the choice of oxazoline ring substituent.[8] For example, Evans *et al*.,[8] recorded substantial differences in the required reaction times of hetero-Diels-Alder reactions of crotonyl phosphonate and ethyl vinyl ether for dihydropropan synthesis. It was noted that the reaction catalysed by the *tert*-butyl substituted [Cu(II)(BOX)](OTf)$_2$ complex required 48 hours at -78ºC for complete conversion, whilst the Ph substituted complex required only 4 hours at the same temperature.[8]

Hutchings *et al*.,[9] observed changes in enantioselectivities when exploring the structure of the BOX ligand in the homogeneous catalysed aziridination reaction, taking into account both the backbone structure and the choice of substituent. Table 5.1 summarises their findings for ligands **1**, **2** and **3** (Scheme 5.1) using Cu(OTf)$_2$ as the metal salt and PhI=NTs as the nitrene donor. Their results show that the best yield and enantioselectivity are obtained using ligand **1**, with poor enantioselectivities recorded using both ligands **2** and **3**.

Table 5.1 Yields and enantioselectivities measured by Hutchings *et al.*,[9] in the homogeneous [Cu(II)(BOX)] catalysed aziridination of styrene, with PhI=NTs as the nitrene source.

Ligand	Yield / %	*ee* / %
1	91	73
2	14	28
3	78	13

The counterion has also been shown to have a pronounced effect on activity. In addition to TfO⁻ and Cl⁻ counterions, SbF_6^- has been used as the Cu(II) counterion with ligand **3** (see [Cu(II)(**3d**)], Scheme 5.2) in the current chapter. Evans *et al.*,[10] reported a 20-fold increase in reactivity and superior enantioselection using cationic [Cu(II)(BOX)](SbF_6)$_2$ compared to the triflate counterparts in the enantioselective Diels-Alder reaction. In their investigation of the structurally similar [Cu(II)(bis(sulfoximine))] complexes, Bolm *et al.*,[11] recorded EPR spectra of the (*S,S*)-bis(sulfoximine) structure shown in Scheme 5.3 below.
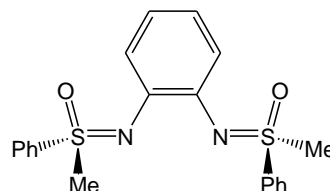
Scheme 5.3 Structure of the (*S,S*)-bis(sulfoximine) ligand investigated by Bolm *et al.*[11]

As part of their investigations into bis(sulfoximine) catalysed Diels-Alder reactions, Bolm *et al.*,[11] recorded CW-EPR spectra of the [Cu(II)(bis(sulfoximine))](X$_2$) complexes with various counterions, X = TfO⁻, SbF_6^-, Cl⁻ and Br⁻. Interestingly, they found that the spectra, where X = TfO⁻ and SbF_6^-, were very similar with resolved copper hyperfine splittings along g_z. The EPR spectra of the complexes in which X = Cl⁻, Br⁻ on the other hand, had very different profiles to X = TfO⁻, SbF_6^- and in that case the spectra were almost isotropic in nature.[11] Investigations in the current chapter, using SbF_6^- as the counterion, will enable similar comparisons to be made for [Cu(II)(**3**)] complexes.

This chapter will therefore present EPR and ENDOR studies of [Cu(II)(BOX)] complexes based on ligands **2** and **3** (Scheme 5.2). The effect of the structural differences in these ligands, compared to ligand **1** (presented in Chapter 4), will be explored. In doing so, the effect of changing the substituent on the chiral carbon of the oxazoline ring will be examined, as well as the replacement of the methyl groups on the bridging carbon with protons. The effect of changing the metal:ligand ratio, which was subject to an in-depth investigation in Chapter 4, will again be considered in

[Cu(II)(BOX)] complexes of ligands **2** and **3**. The counterion effect will also be systematically examined, with a comparison of X = TfO⁻, Cl⁻ and SbF₆⁻.

5.2 Experimental

Full details of the experimental methods used to prepare the Cu(II) complexes shown in Scheme 5.2 were given in Chapter 3, and only a brief description will be given here.

The heteroleptic complexes [Cu(II)(**2a,c**)] and [Cu(II)(**3a,c**)] were prepared according to literature methods,[12] by reacting Cu(OTf)₂ or CuCl₂ in THF/DCM with (**2**) or (**3**) respectively. The homoleptic complexes, [Cu(II)(**2b**)] and [Cu(II)(**3b**)], were synthesised by stirring (**2**) or (**3**) with Cu(OTf)₂/CuCl₂ in THF/DCM for 1 hour at room temperature. [Cu(**3d**)] was prepared under inert atmosphere in the dark, according to literature methods.[7]

For CW- and pulsed EPR/ENDOR measurements, the copper complexes [Cu(II)(**2a-c**)] and [Cu(II)(**3a-d**)] (*ca.* 7x10⁻³ M for EPR, *ca.* 4x10⁻² M for ENDOR) were dissolved in d⁸-THF:d²-DCM For *X*-band CW-EPR, protic solvents were used. All *X*-band EPR spectra were recorded on a Bruker EMX spectrometer equipped with a high sensitivity *X*-band cavity (ER 4119HS). The *Q*-band CW-ENDOR spectra were recorded at 10 K on a CW Bruker ESP 300E series spectrometer equipped with an ESP360 DICE ENDOR unit, in a *Q*-band ENDOR cavity (Bruker ER 5106 QT-E). The pulsed *X*-band EPR/ENDOR spectra were recorded on a Bruker Elexsys E580 spectrometer equipped with a liquid Helium cryostat from Oxford Inc.

5.3 Results and Discussion

5.3.1 CW-EPR of [Cu(II)(**2a-c**)]

As with ligand (**1**), the [Cu(II)(BOX)] complexes synthesised using ligand (**2**) can be prepared easily by stirring a suitable Cu(II) salt with the required BOX ligand in solution at room temperature. As illustrated in Chapter 4, the Cu(II):BOX ratio is critical in forming the desired complex. A solution of ligand (**2**) was stirred with Cu(OTf)₂ in a 1:1 ratio of metal:ligand. Figure 5.1a shows the resulting EPR spectrum. The ligand, (**2**), was then added in a 6-fold excess to the solution of the Cu(OTf)₂ salt (Figure 5.1b). Addition of a 6-fold excess of the ligand to a CuCl₂ solution gave a spectrum (Figure 5.1c) that appears to be identical to Figure 5.1b. Ligand (**2**) was also added to a CuCl₂ solution in a 1:1 ratio. The resulting EPR spectrum is shown in Figure 5.1d.
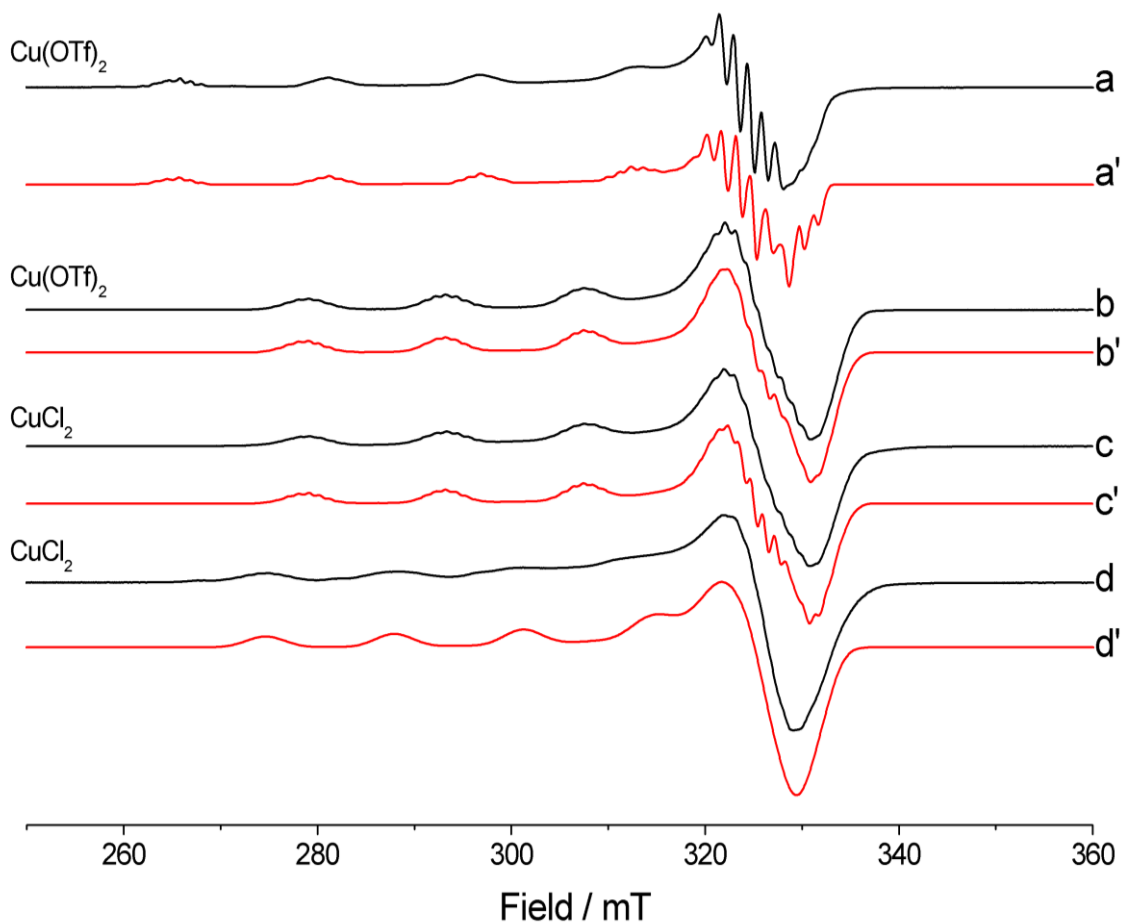
Figure 5.1 *X*-band CW-EPR spectra (140 K) of a) [Cu(II)(**2a**)], b) [Cu(II)(**2b**)], c) [Cu(II)(**2b**)] and d) [Cu(II)(**2c**)] dissolved in THF:DCM (1:1). The corresponding simulations are given in a'-d' (red line). The copper salt used in the synthesis of each complex is noted on the left.
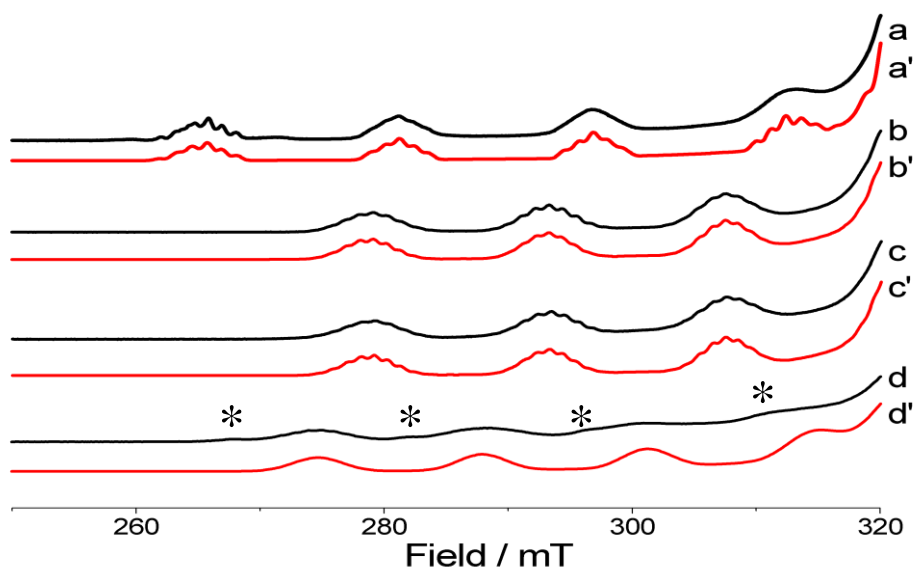
Figure 5.2 *X*-band CW-EPR spectra (140 K) of a) [Cu(II)(**2a**)], b) [Cu(II)(**2b**)] (synthesised from Cu(OTf)$_2$), c) [Cu(II)(**2b**)] (synthesised from CuCl$_2$) and d) [Cu(II)(**2c**)], dissolved in THF:DCM (1:1). The corresponding simulations are given in a'-d' (red line). The asterisks (*) highlight the presence of an additional hyperfine pattern (assigned to excess CuCl$_2$).

The first spectrum shown in Figure 5.1a exhibits a largely axial profile. Four absorptions are visible in the parallel region of the spectrum, as expected since $I = 3/2$. The pronounced superhyperfine couplings observed (Figure 5.2a) are a direct result of the coordination of ligand **2** to the Cu(II) centre. In this synthesis, a 1:1 metal:ligand ratio was used, and so it can be proposed that this complex must be assigned to the heteroleptic [Cu(II)(**2a**)] species (see Scheme 5.2). The simulation of this spectrum is shown in Figure 5.1a', and again in Figure 5.2a'. Simulation of this spectrum suggests slight rhombicity, with $g_1 \neq g_2 \neq g_3$. The spin Hamiltonian parameters are $g_1 = 2.064$, $g_2 = 2.073$ and $g_3 = 2.318$, whilst $A_1 = A_2 = 15$ MHz and $A_3 = 503$ MHz (Table 5.2). The distribution and splittings of the nitrogen superhyperfine couplings are in agreement with the expectations for a heteroleptic [Cu(II)(BOX)] complex, for which five lines with an intensity pattern of 1:2:3:2:1 are expected, as explained in Section 2.2.6 (Chapter 2). In order to simulate the nitrogen superhyperfine splittings, the same parameters as previously determined by ^{14}N ENDOR for the analogous [Cu(II)(**1a**)] complex, were used (Section 4.3.2). These values provide a satisfactory fit for the nitrogen superhyperfine splittings in the *X*-band EPR spectra. For [Cu(II)(**1a**)], simulation of ^{1}H ENDOR data revealed the presence of strongly coupled protons originating from water molecules bound to the Cu(II) centre (Section 4.3.3). This was in agreement with the crystal structure of [Cu(II)(**1a**)] reported by Evans, which shows two water molecules coordinated in the equatorial position.[12] Similar coordination of water molecules to the Cu(II) centre can be assumed in the structurally similar [Cu(II)(**2a**)] as this complex was prepared "on the bench" using commercially available $Cu(OTf)_2$. $Cu(OTf)_2$ is hygroscopic and it is very difficult to completely eliminate the presence of water.

After reacting an excess of the ligand with the triflate salt, a further change in the shape of the spectrum is evident (Figure 5.1b), indicative of the formation of the homoleptic complex [Cu(II)(**2b**)], as revealed by the change in nitrogen superhyperfine. Interestingly, performing the same reaction using $CuCl_2$ instead of $Cu(OTf)_2$, resulted in an identical EPR spectrum (Figure 5.1c) which has been simulated using exactly the same parameters (Figure 5.1c', Table 5.2), implying that the homoleptic complex [Cu(II)(**2b**)] can be synthesised using either $Cu(OTf)_2$ or $CuCl_2$ as the starting salt. This was not the case using ligand (**1**), where even a 1:20 ratio of $CuCl_2$:ligand **1** gave exclusively the EPR spectrum of the heteroleptic complex [Cu(II)(**1a**)] (Section 4.3.1). This suggests that removal of the electron donating methyl groups on the bridging

carbon affects the electron distribution around the Cu(II) centre and facilitates the formation of the homoleptic species.

Finally, Figure 5.1d (with the expanded parallel region shown in Figure 5.2d) shows the EPR spectrum assigned to the heteroleptic [Cu(II)(**2c**)] complex. The linewidths are considerably broader in this spectrum and no superhyperfine splitting can be resolved. Close inspection of Figure 5.2d reveals an additional hyperfine pattern (labelled *), which can be assigned to excess starting $CuCl_2$ salt ($g_1 = g_2 = 2.061$, $g_3 = 2.316$, $A_1 = A_2 = 55$ MHz and $A_3 = 458$ MHz). Despite this, there is a definite shift in the simulated peaks (Figures 5.1d' and 5.2d') from $CuCl_2$, which provides clear evidence of the formation of this heteroleptic complex.

5.3.2 CW-EPR of [Cu(II)(*3a-d*)]

Ligand (**3**) has also been used to synthesise a similar series of analogous [Cu(II)(BOX)] complexes by stirring a suitable Cu(II) salt with the appropriate ligand in solution. A solution of ligand (**3**) was stirred with $Cu(OTf)_2$ in a 1:1 ratio of metal:ligand. Figure 5.3a shows the resulting EPR spectrum. The ligand, (**3**), was then added in a 6-fold excess to $Cu(OTf)_2$ (Figure 5.3b). Addition of ligand (**3**) to $CuCl_2$ in a 1:1 ratio gave the EPR spectrum shown in Figure 5.3c. A further reaction was then performed in which isolated [Cu(II)(**3c**)] (synthesised in DCM) was stirred for 3 hours in an inert atmosphere with $AgSbF_6$, and in the absence of light, according to the method of Evans *et al.*[7] Figure 5.3d shows the EPR spectrum of the resulting solution.

For the group of [Cu(II)(BOX)] complexes formed using ligand **3**, the linewidths were too broad to reveal any superhyperfine resolution (Figure 5.3). The line broadening of this series of complexes, in comparison to those synthesised using ligands **1** and **2**, could be a result of the slower tumbling rate of the [Cu(II)(**3**)] complexes due to the bulkiness of the *tert*-butyl substituents of the oxazoline rings in comparison to the Ph substituents in ligands **1** and **2**.[13] Since the effective molar volume (V_{eff}) of ligands **1**, **2** and **3** should all be closely similar, it is perhaps unlikely that diverse tumbling rates are responsible for the differences in the quality of the spectra. Instead this broadening effect could also be due to bad glass, the *g*-strain effect or different relaxation rates.
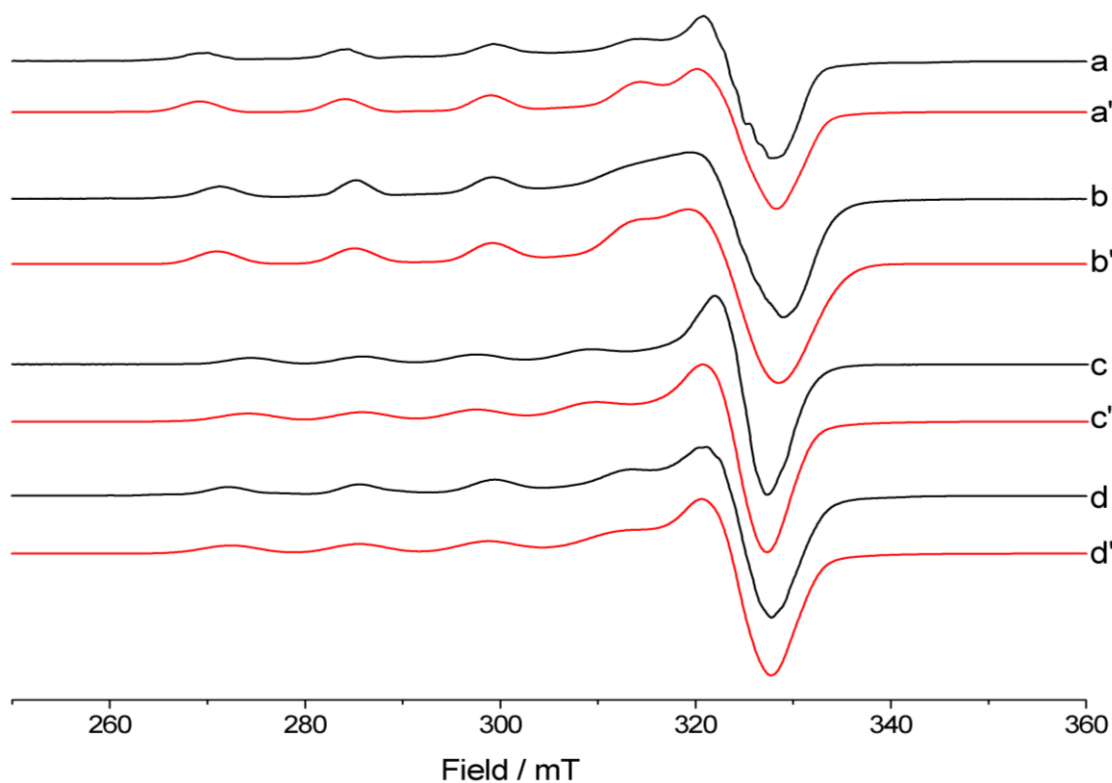
Figure 5.3 *X*-band CW-EPR spectra (140 K) of a) [Cu(II)(**3a**)], b) [Cu(II)(**3b**)], c) [Cu(II)(**3c**)] and d) [Cu(II)(**3d**)] dissolved in THF:DCM (1:1). The corresponding simulations are given in a'-d' (red line).

Despite the lack of superhyperfine resolution, the spin Hamiltonian parameters found by simulation are indicative of Cu(II) coordination to (**3**). The *g*-values have decreased and the ^{Cu}A-values have increased in comparison to those of the starting metal salt, Cu(OTf)$_2$. This trend was observed previously with the analogous [Cu(II)(**1a**)] and [Cu(II)(**2a**)] complexes. The complex synthesised using a 1:1 metal:ligand ratio (Figure 5.3a) can therefore be assigned to the heteroleptic [Cu(II)(**3a**)] complex. Due to the moisture sensitive nature of the Cu(OTf)$_2$ starting salt, the coordination of water molecules to the Cu(II) centre can again be assumed. The crystal structure of [Cu(II)(**3**)(OTf)(H$_2$O)$_2$][OTf] has previously been reported by Evans *et al*.,[6] revealing a distorted square pyramidal geometry, with one triflate ligand bound weakly to the metal centre in the apical position (Cu-OTf 2.624 Å) and the other fully dissociated (Cu-OTf 3.667 Å). The reported crystal structure suggests that the two water molecules occupy the equatorial positions and are distorted by approximately 26° out of the plane of the ligand.[6] The EPR spectrum (Figure 5.3a) does not provide sufficient evidence to confirm that the nature of the interaction between the Cu(II) centre with water molecules / triflate ligands is the same in the solvated complex (in frozen solution) as in the solid state single crystal.[6]

After reacting a six-fold excess of the ligand with the triflate salt, a further change in the spectrum is evident (Figure 5.3b), indicative of the formation of the homoleptic complex [Cu(II)(**3b**)], with two bis(oxazoline) ligands bound to the Cu(II) centre. The spectrum shown in Figure 5.3c was recorded after reacting an equivalent amount (1:1 molar ratio) of ligand **3** with $CuCl_2$ in solution. This has therefore been assigned to the heteroleptic complex [Cu(II)(**3c**)], with only one bis(oxazoline) ligand coordinated to the metal centre. In the case of $CuCl_2$, increasing the Cu(II):BOX ratio further did not lead to any changes to the shape of the spectrum.

It was therefore found that with both ligands **1** and **3**, the homoleptic complex cannot be synthesised when using $CuCl_2$ as the starting salt. When considering this effect earlier for ligand **1** (Section 4.3.1) it was deduced that the stronger coordination of the Cl^- counterion in comparison to the TfO^- counterion, prevented the formation of a homoleptic complex. An important similarity between ligands **1** and **3** is the presence of two methyl groups on the bridging carbon between the oxazoline rings. Using ligand **2**, which has two protons (as opposed to two methyl groups) on the bridging carbon, it proved possible to synthesise the homoleptic complex using both $Cu(OTf)_2$ and $CuCl_2$ starting salts. This suggests that backbone substitution is key. Methyl groups can behave as electron donors by inductive effect, thus pushing electrons towards the Cu(II) centre. Removal of the methyl groups could therefore result in less electron density being localised around the Cu(II) centre. This appears to weaken the interaction between the Cu(II) centre and the chloride groups, thus facilitating the formation of the homoleptic complex, [Cu(II)(**2b**)].

Another interesting point to note is that the decrease in g_3 and A_3 from the heterlopetic complex to the homoleptic complex with ligand **3** is significantly smaller than that seen for ligands **1** and **2**. From [Cu(II)(**1a**)] to [Cu(II)(**1b**)], there is a decrease of 0.100 in g_3 and 46 MHz in A_3. Significant differences in the g and A values are also evident going from [Cu(II)(**2a**)] to [Cu(II)(**2b**)], with a decrease of 0.088 in g_3 and 62 MHz in A_3. However, for the analogous complexes synthesised using ligand **3**, the decrease in g_3 is only 0.005 and only 26 MHz in A_3. This smaller degree of change is likely to be due to limitations resulting from the bulkiness of the *tert*-butyl ligand.

Finally, the EPR spectrum shown in Figure 5.3d has been assigned to the heteroleptic [Cu(II)(**3d**)] complex. Displacement of the Cl^- counterions with SbF_6^-, following the method of Evans *et al.*,[7] had a large impact on the A_3 parameter, changing from 365 MHz for [Cu(II)(**3c**)] to 433 MHz for [Cu(II)(**3d**)] (Table 5.2). The crystal structure of [Cu(II)(**3**)](SbF_6)$_2$(H_2O)$_2$ has also been reported by Evans and co-workers.[7]

This crystal structure suggests that upon exposure to atmospheric moisture, water is introduced to $[Cu(II)(\mathbf{3})](SbF_6)_2$ to form $[Cu(II)(\mathbf{3})](SbF_6)_2(H_2O)_2$ which exhibits distorted square planar geometry. The authors propose that the SbF_6^- counterions are not coordinated to the metal centre but that both water molecules are coordinated and are displaced at an average angle of 33º out of the Cu(II)-ligand plane.[7] Water coordination can be assumed in this work because although the reaction was performed under dinitrogen, the resulting product was exposed to atmospheric moisture.

As described in the introduction (Section 5.1), Bolm et al.,[11] investigated similar bis(sulfoximine) complexes (Figure 5.1), and found that the EPR spectra, when X = TfO$^-$ and SbF$_6^-$, were very similar, but different to the spectrum when X = Cl$^-$. In the current results for BOX ligand **3**, the values for $g_{1,2,3}$ and $A_{1,2}$ are of similar magnitude in complexes $[Cu(II)(\mathbf{3a})]$, $[Cu(II)(\mathbf{3c})]$ and $[Cu(II)(\mathbf{3d})]$, when X = TfO$^-$, Cl$^-$ and SbF$_6^-$ respectively. However, the A_3 values are very different for these complexes. For X = TfO$^-$, $A_3 = 469$ MHz, for X = Cl$^-$, $A_3 = 365$ MHz and for X = SbF$_6^-$, $A_3 = 433$ MHz. Taking into consideration these A_3 values, it is evident that the spectra when X = TfO$^-$ and SbF$_6^-$ are more similar than the spectrum when X = Cl$^-$, reflecting the findings of Bolm et al.[11] It is possible that this is partially due to the water coordination in $[Cu(II)(\mathbf{3a,d})]$.

Table 5.2 Experimental g and A^{Cu} spin Hamiltonian parameters for the [Cu(II)(BOX)] complexes [Cu(II)(**2a-c**)] and [Cu(II)(**3a-d**)] in THF:DCM (1:1).

Complex	$^a g_1$	$^a g_2$	$^a g_3$	$^b A_1$	$^b A_2$	$^c A_3$
Cu(OTf)$_2$	2.083	2.083	2.412	13	13	403
CuCl$_2$	2.061	2.061	2.316	55	55	458
[Cu(**2a**)]	2.064	2.073	2.318	15	15	503
^{d}[Cu(**2b**)]	2.054	2.063	2.230	26	29	441
^{e}[Cu(**2b**)]	2.054	2.063	2.230	26	29	441
[Cu(**2c**)]	2.054	2.063	2.274	26	29	414
[Cu(**3a**)]	2.064	2.073	2.297	15	15	469
[Cu(**3b**)]	2.066	2.066	2.292	15	15	443
[Cu(**3c**)]	2.066	2.066	2.297	15	15	365
[Cu(**3d**)]	2.066	2.066	2.291	15	15	433

All A values given in MHz; ^{a} ±0.004; ^{b} ±3 MHz; ^{c} ±6 MHz. ^{d} = complex synthesised using Cu(OTf)$_2$. ^{e} = complex synthesised using CuCl$_2$.

5.3.3 ^1H and ^{14}N CW-ENDOR of [Cu(II)(**2b**)]

As well as recording *X*-band CW-EPR spectra, ENDOR spectroscopy has also been utilised to probe the effect of changing the structure of the BOX ligand. In the current section, *Q*-band CW-ENDOR has been used to investigate the structure of the homoleptic complex [Cu(II)(**2b**)]. In order to understand further the effect of changing the carbon backbone architecture by removing the methyl group substituents on the bridging carbon, this ENDOR data has been compared with that of the analogous homoleptic complex, [Cu(II)(**1b**)].

Figure 5.4 shows the *Q*-band EPR spectrum of [Cu(II)(**2b**)] (synthesised from Cu(OTf)$_2$) with the corresponding simulation and roadmap. The roadmap illustrates the orientation dependence with respect to the change in applied magnetic field direction, as discussed in Section 2.3.4. From this EPR spectrum, an angular selective ^1H ENDOR study was performed, as shown in Figures 5.5 and 5.6. The ENDOR spectra showing hyperfine couplings to the proton nuclei of complex [Cu(II)(**2b**)] were recorded in CW mode. Pulsed ENDOR data was also recorded for complex [Cu(II)(**2b**)] but unfortunately this data did not provide further insight into the system and so has not been shown for brevity.
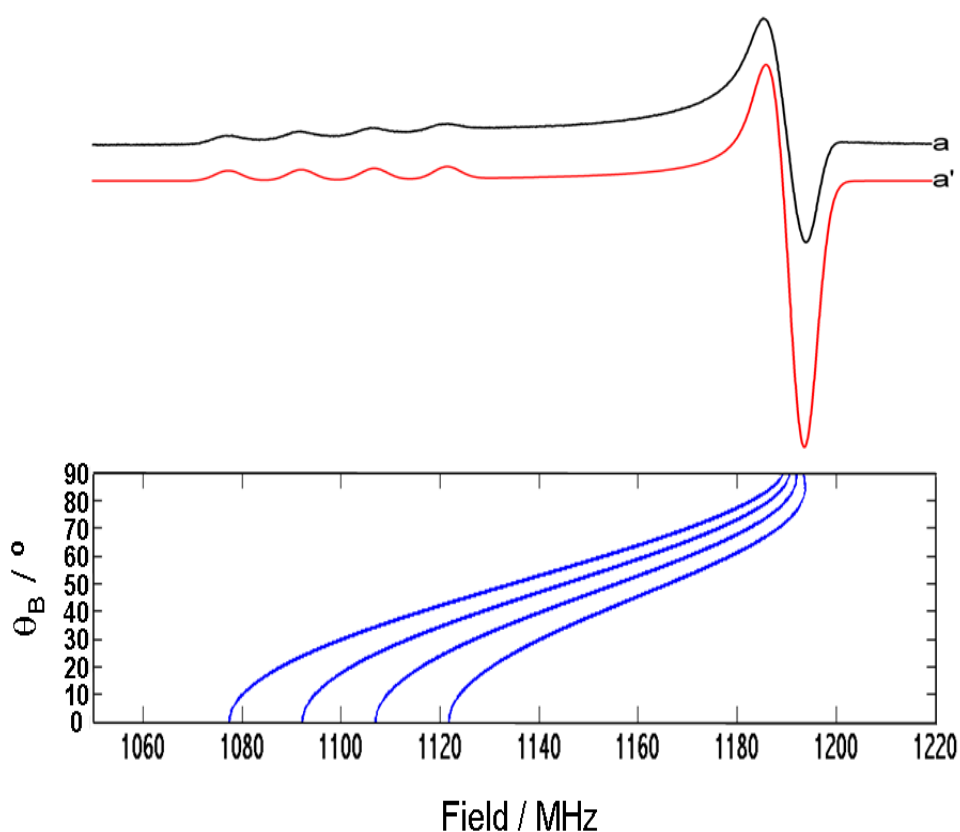
Figure 5.4 *Q*-band CW-EPR spectra (50 K) of a) [Cu(II)(**2b**)] dissolved in THF:DCM (1:1). The corresponding simulation is given in a' (red line) and the corresponding roadmap shown in blue.

The CW-ENDOR spectra were recorded at both high modulation, of 200-250 kHz (Figure 5.5), and at lower modulation, of 80-100 kHz (Figure 5.6). The high modulation frequency is particularly useful for large couplings of low intensity, whilst low modulation is more appropriate for smaller couplings of higher intensity. Recording the spectra at both these modulation frequencies therefore ensures that the data is optimised for both large and small couplings. Figure 5.7 shows the ^{1}H ENDOR spectra recorded at the principal turning points ($g = g_{\parallel}$ and $g = g\perp$). These are shown along with the corresponding spectra for [Cu(II)(**1b**)] in order to enable comparisons to be made between these complexes.
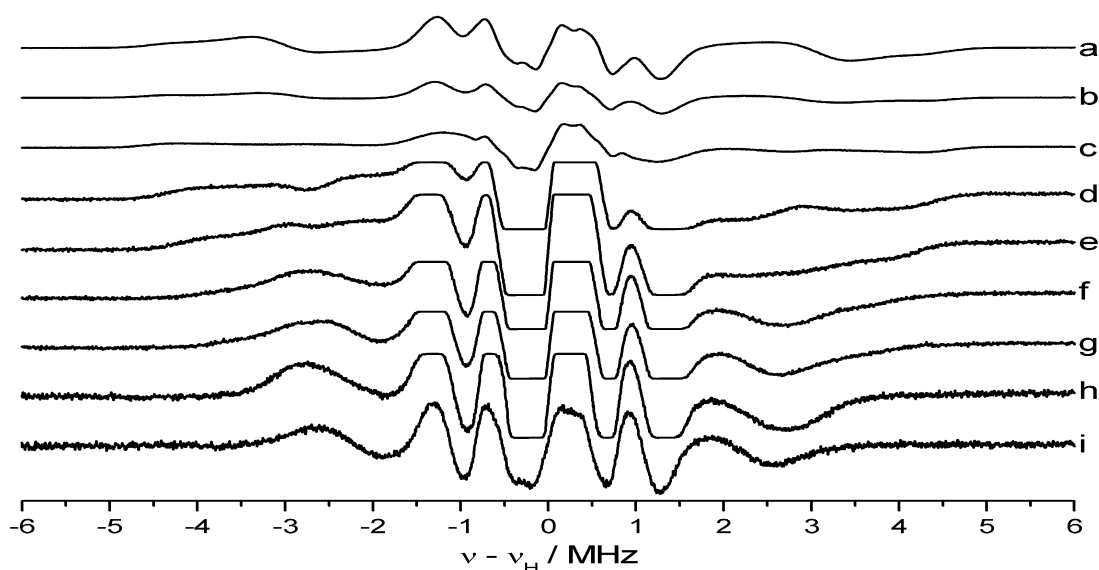
Figure 5.5 Q-band ^{1}H CW-ENDOR (10 K, 200-250 kHz) of [Cu(II)(**2b**)] dissolved in d[8]-THF: d[2]-DCM (1:1) recorded at the field positions a) 1189.7, b) 1185.1, c) 1166.8, d) 1146.3, e) 1136.0, f) 1125.6, g) 1121.1, h) 1098.2 and i) 1077.6 mT.
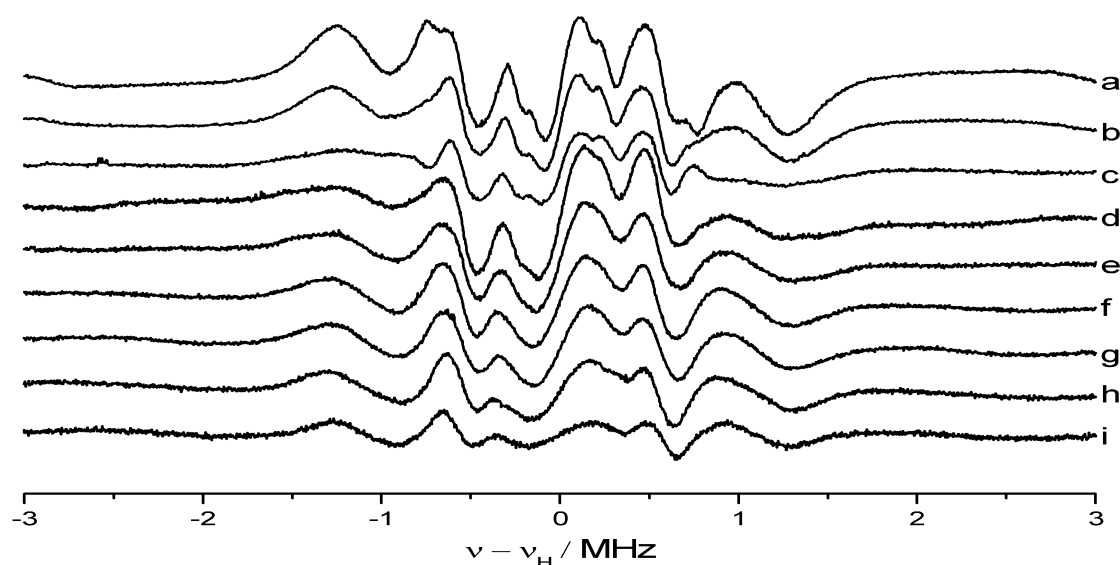
Figure 5.6 Q-band ^{1}H CW-ENDOR (10 K, 80-100 kHz) of [Cu(II)(**2b**)] dissolved in d[8]-THF: d[2]-DCM (1:1) recorded at the field positions a) 1189.7, b) 1185.1, c) 1177.1, d) 1146.3, e) 1136.0, f) 1125.6, g) 1121.1, h) 1098.2 and i) 1077.6 mT.
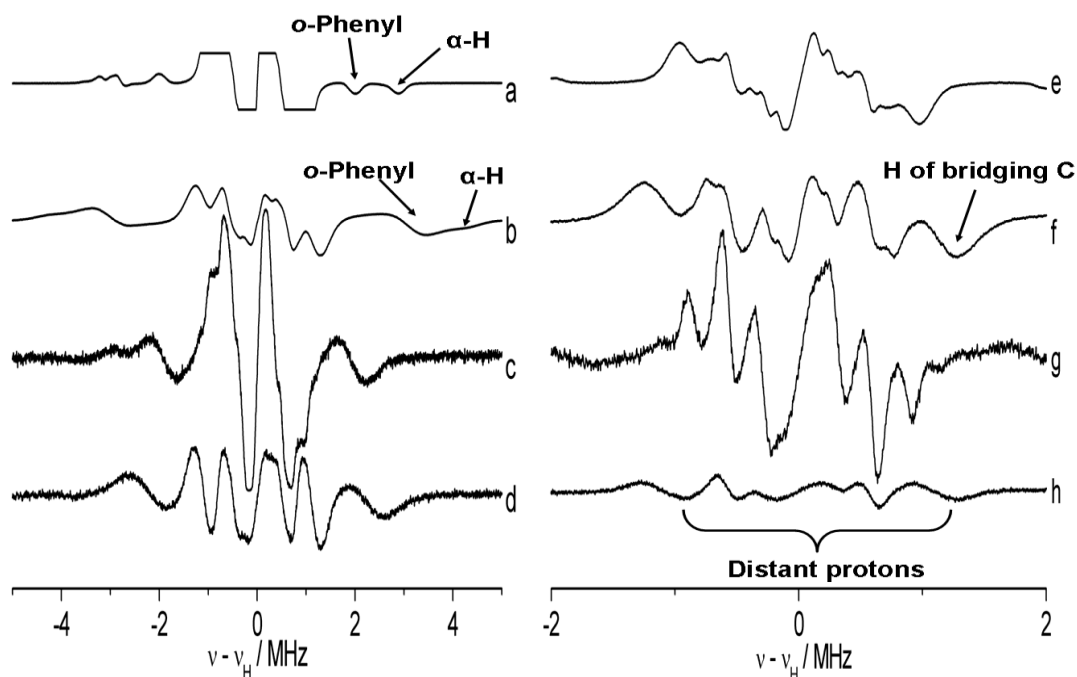
Figure 5.7 Q-band ^{1}H CW-ENDOR spectra (10 K) of a,c,e,g) [Cu(II)(**1b**)] (1:1 d^3-AcN:d^2-DCM), and b,d,f,h) [Cu(II)(**2b**)] (1:1 d^8-THF: d^2-DCM). The spectra were recorded at the field positions corresponding to: a,b,e,f) $g = g_\perp$ and c,d,g,h) $g = g_\parallel$. The spectra on the left (a-d) were recorded at high modulation (200-250 kHz) whilst those on the right (e-h) were recorded at low modulation (80-100 kHz).

Focusing firstly on the high modulation spectra, the coupling observed at $A_1 = 3.0$ MHz in Figure 5.7a ([Cu(II)(**1b**)]) was assigned to the o-phenyl protons, whilst the larger coupling of 5.9 MHz was assigned to the α-protons of the oxazoline rings (Section 4.3.3). It is interesting to note that these couplings have shifted significantly in Figure 5.7b, the spectrum for the analogous [Cu(II)(**2b**)]. In this spectrum, a larger coupling of around 8.5 MHz is evident. This large coupling actually consists of two broad peaks. The coupling of the inner peaks is around 6.9 MHz. It can be suggested that these couplings are also due to the o-phenyl ($A_1 \approx 6.9$ MHz) and α-H ($A_1 \approx 8.5$ MHz). The increase in coupling in comparison to the analogous peaks for [Cu(II)(**1b**)] is likely to be caused by the change in electron distribution around the Cu(II) centre as a direct result of replacement of the methyl groups on the bridging carbon with proton groups. Although simulation of these couplings has proven to be difficult, the magnitude of the couplings is comparable to literature values. For example, Carter *et al.*,[14] have recorded ^{1}H ENDOR of a [Cu(II)(en)$_2$](OTf)$_2$ complex (en = 1,2-diaminoethane). Here, $A_1 = 5.70$ MHz for the axial positioned methine protons of the carbon backbone. For the single crystal ENDOR spectrum of [Cu(salen)], Kita *et al.*,[15] identified two distinct sites for the imine proton, with $A_1 = 18.43$ MHz and 18.64 MHz (the angle between g_z and A_3, $\theta_H = 90°$).

It should also be noted here that there is a change in the g and A values for the parallel region for [Cu(II)(**1b**)] in comparison to [Cu(II)(**2b**)], as found from simulation of the EPR data. For [Cu(II)(**1b**)], $g_3 = 2.254$, whilst for [Cu(II)(**2b**)], $g_3 = 2.230$. Similarly, for [Cu^{II}(**1b**)], $A_3 = 461$ MHz, whilst for [Cu(II)(**2b**)], $A_3 = 441$ MHz. These differences in the EPR spin Hamiltonian parameters are consistent with the differences seen in the ENDOR data of these two complexes.

The next largest coupling is labelled in the low modulation spectrum, Figure 5.7f, which has a magnitude of ~2.6 MHz. This coupling has been assigned to the protons of the bridging backbone carbons. There is no equivalent coupling evident for [Cu(II)(**1b**)] as the protons of the methyl groups are further away from the Cu(II) centre. From the low modulation spectra (Figure 5.7e-h), it can be seen that the peaks with the smallest couplings (less than 2 MHz) are very similar in both the [Cu(II)(**1b**)] and [Cu(II)(**2b**)] complexes. This is not surprising, as it is likely that these peaks arise from the *meta*- and *para*- protons of the phenyl rings, as well as the remaining protons of the oxazoline ring. These protons (which arise in both complexes) are less likely to be affected by electronic changes due to the change in the bridging carbon substituent, due to their greater distance from the Cu(II) centre.

Although simulation of these ^{1}H CW-ENDOR spectra has proven to be extremely difficult, this comparison of the spectra of [Cu(II)(**1b**)] and [Cu(II)(**2b**)] (Figure 5.7) highlights that any structural changes to the BOX ligand has a large impact on the electronic distribution of the resulting complexes, and this is reflected in the differences in their ENDOR spectra.

The ^{14}N Q-band CW-ENDOR was also recorded for [Cu(II)(**2b**)], and again this has been compared to [Cu(II)(**1b**)] (Figure 5.8). As was found in the data for [Cu(II)(**1b**)] (Figure 4.9, Section 4.3.2), the ^{14}N ENDOR for [Cu(II)(**2b**)] is weak in intensity. However, it can be seen from both the perpendicular spectra (Figure 5.8a-b) and the parallel spectra (Figure 5.8c-d) that the ^{14}N absorptions occur at different resonant frequencies in [Cu(II)(**2b**)] in comparison to [Cu(II)(**1b**)]. This again emphasises that replacement of the methyl groups of the bridging carbon with protons significantly influences the resulting spin density of the [Cu(II)(BOX)] complexes. As mentioned earlier, alkyl groups (-CH$_3$) are well known electron donating groups by inductive effects. Therefore in [Cu(II)(**1b**)], more electron spin will be localised on ^{14}N, resulting in larger couplings in comparison to [Cu(II)(**2b**)], as seen in Figure 5.8. In [Cu(II)(**2b**)], which has no methyl groups on the carbon backbone, less electron spin is localised on ^{14}N. As a result, more spin is available for delocalisation onto the BOX

ligand, which accounts for the larger *o*-phenyl and α-H couplings observed in Figure 5.7. The substituent of the bridging carbon may affect the catalytic reaction, as demonstrated in a recent report by Lebel *et al.*[16] The authors considered the effect of the bridging carbon substituent in the Cu(I)-bis(oxazoline) catalysed enantioselective aziridination of 4-nitrostyrene. Modification of the bridging substituents of the ligand was found to affect the catalysis.[16] Small substituents (such as protons) or a cyclopropane ring on the bridging carbon atoms, which increase the N=C-C=N angle and the bite angle of the ligand, were found to decrease the % *ee* of the reaction.[16]
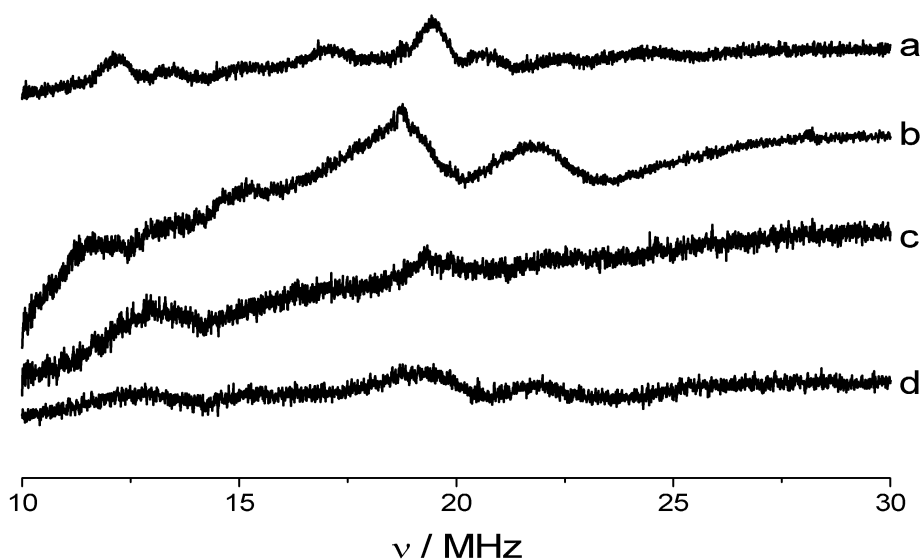
Figure 5.8 *Q*-band ^{14}N ENDOR spectra (10 K) of a,c) [Cu(II)(**1b**)] and b,d) [Cu(II)(**2b**)] recorded at field positions corresponding to: a,b) $g = g_\perp$ and c,d) $g = g_\parallel$.
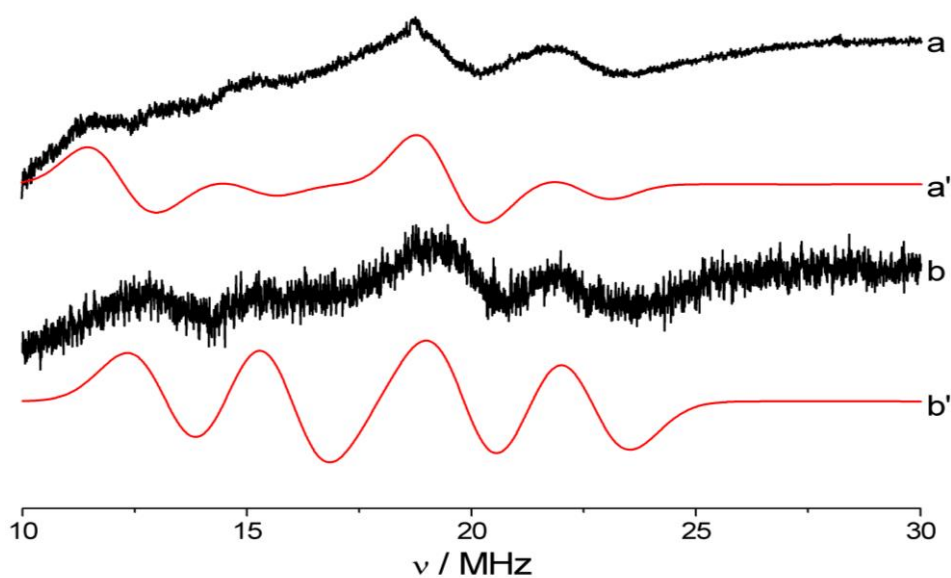
Figure 5.9 *Q*-band ^{14}N ENDOR spectra (10 K) of [Cu(II)(**2b**)] recorded at field positions corresponding to: a) $g = g_\perp$ and b) $g = g_\parallel$. The corresponding simulations are shown in a'-b' (red line).

Table 5.3 ^{14}N hyperfine and quadrupole parameters for bis(oxazoline) nitrogens in the [Cu(II)(**1b**)] and [Cu(II)(**2b**)] complexes.

Complex	$^{(a)}A_1$	A_2	A_3	$^{(b)}P_1$	P_2	P_3
[Cu(**1b**)]	39.8	33.1	32.9	-0.57	0.52	0.05
[Cu(**2b**)]	34.5	31.5	35.9	-1.3	0.32	0.98

All values are given in MHz; $^{(a)}$ ±0.6 MHz; $^{(b)}$ ±0.3 MHz.

Having compared the ^{14}N ENDOR spectra of [Cu(II)(**1b**)] with [Cu(II)(**2b**)], the relevant spectra with the corresponding simulations are given in Figure 5.9, recorded at the perpendicular and parallel field positions. Due to the weak intensity of the signal, simulation was difficult, thus compromising the accuracy of the simulation parameters. However, the values obtained for [Cu(II)(**2b**)] (Table 5.3) do show smaller A_1 and A_2 values in comparison to [Cu(II)(**1b**)], for reasons explained above. Like [Cu(II)(**1b**)], the hyperfine and quadrupolar coupling from the ^{14}N ($I = 1$) nuclei in the [Cu(II)(**2b**)] deviates from axial symmetry.

5.3.4 Pulsed ENDOR of [Cu(II)(3c)]

Pulsed EPR and ENDOR can also be used to probe the structure of Cu(II) complexes. Figure 5.10a shows the CW-EPR spectrum of [Cu(II)(**3c**)] whilst 5.10b is the corresponding field swept echo detected (FSED) pulsed EPR spectrum. CW-EPR produces a first derivative of the absorption spectrum due to technical reasons involving the use of magnetic field modulation and narrow-band phase-sensitive detection. CW-EPR often enables spectra with optimum resolution to be recorded with high sensitivity.[17] However, it can be beneficial to record FSED-EPR in addition to CW-EPR because a FSED-EPR spectrum measures the absorption signal directly, by measuring the transient signal which is created by a sequence of microwave pulses with fixed time intervals and variable external magnetic field.[17] This direct method of measuring the spectrum can provide improved resolution in comparison to the CW technique for EPR spectra with very broad lines.[17] Simulation of the X-band CW-EPR was shown in Figure 5.3c', with the hyperfine values listed in Table 5.2.
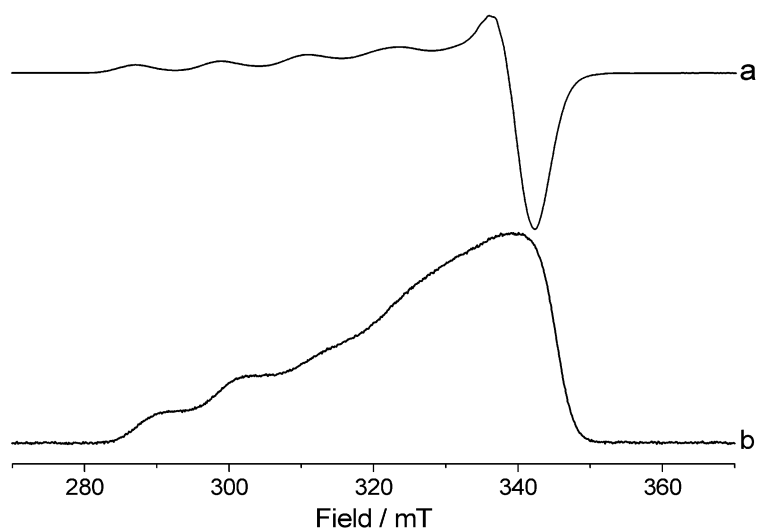
Figure 5.10 *X*-band EPR spectra (140 K) of [Cu(II)(**3c**)] recorded in a) CW mode and b) field swept echo detected (FSED) pulsed mode.

After recording the *X*-band CW and FSED EPR spectra of [Cu(II)(**3c**)], as shown in Figure 5.10, it was then possible to record a series of pulsed ENDOR spectra at field positions corresponding to the principal turning points, as explained in Section 2.3.4. Figure 5.11 shows a series of nitrogen Davies ENDOR spectra. For reasons explained in Section 4.3.2, contributions from ^{1}H nuclei are present in addition to the strongly coupled ^{14}N nuclei (Figure 5.11). Due to the strong intensities of the ^{1}H signals, simulation of the ^{14}N peaks (without the corresponding *Q*-band ^{14}N CW-ENDOR) cannot be performed accurately due to the broadness of these signals making individual peaks too difficult to determine. However, since both the methyl groups on the carbon backbone and the *tert*-butyl groups on the chiral carbon of the oxazoline rings in [Cu(II)(**3c**)] are electron donating, the ^{14}N couplings are expected to be significantly larger for [Cu(II)(**3c**)] compared to [Cu(II)(**1c**)]. In order to compare the data, the ^{14}N *Q*-band CW-ENDOR data simulation shown previously in Figure 4.10 was re-simulated at *X*-band in absorption mode. This showed that the couplings for [Cu(II)(**1c**)] are evident at field positions of around 1.8 MHz larger than those of [Cu(II)(**3c**)]. This was unexpected, due to the electron donating effect of the *tert*-butyl groups in [Cu(II)(**3c**)] and suggests that the phenyl ring substituents are resulting in a slightly stronger Cu…^{14}N coordination.
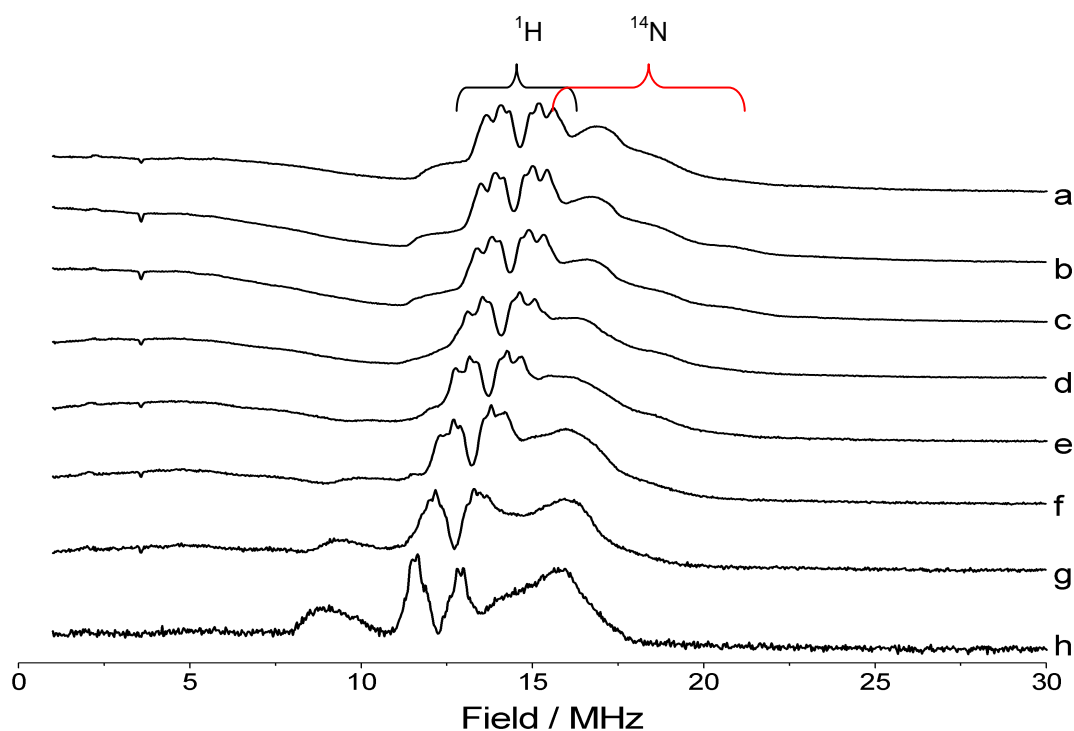
Figure 5.11 *X*-band Davies ENDOR spectra (10 K) of [Cu(II)(**3c**)] recorded at field positions of a) 343.1, b) 339.3, c) 336.5, d) 330.5, e) 321.5, f) 310.7, g) 298.6 and h) 286.7 mT.

5.4 Conclusion

This chapter has further investigated the effect of changing the metal to ligand ratio and changing the counterion of the [Cu(II)(BOX)] complexes. In Chapter 4, only X = TfO⁻ and Cl⁻ was studied whilst this chapter has delved further and also considered X = SbF₆⁻, a particularly useful counterion in the Diels-Alder reaction. Additionally, the effect of the structure of the BOX ligand has been examined; specifically the effect of the substituents on the bridging carbon between the oxazoline rings and the substituents on the chiral carbon of the oxazoline rings. A series of complexes based on ligand **2**, were first presented. It was found that when using ligand **2**, coordination of two BOX ligands to the Cu(II) centre was possible when using both Cu(OTf)₂ and CuCl₂ starting salts. When using ligands **1** and **3** however, only Cu(OTf)₂ enabled the formation of the homoleptic complex. This therefore suggests that the removal of the methyl groups has a direct influence on the electronic environment of the Cu(II) centre which facilitates the formation of the homoleptic complex. A series of spectra based on complexes synthesised using ligand **3** have also been presented. CW-ENDOR was used to probe the homoleptic complex, [Cu(II)(**2b**)], in order to further investigate the effect of the removal of the methyl groups from the bridging carbon. Larger *o*-phenyl and α-H couplings were observed in the ¹H ENDOR spectra of [Cu(II)(**2b**)] in comparison to [Cu(II)(**1b**)], which has methyl groups on the bridging carbon of the oxazoline rings. It

can be deduced that these larger couplings are a direct result of replacing the methyl groups (which are electron donating by inductive effects) with proton groups (which have less directing effect on the electron spin, making more electron density available for delocalisation around the ligand). Pulsed Davies ENDOR of the heteroleptic complex [Cu(II)(**3c**)], was recorded in order to explore the effect of replacing the phenyl groups with *tert*-butyl substituents. The strong intensities of the ^{1}H signals resulted in difficulty in determining individual ^{14}N peaks and therefore simulation could not be performed accurately. However, comparison of this data with ^{14}N CW-ENDOR of [Cu(II)(**1c**)] revealed that the couplings for [Cu(II)(**1c**)] are evident at field positions of around 1.8 MHz larger than those of [Cu(II)(**3c**)], suggesting that the phenyl ring substituents result in a slightly stronger Cu…^{14}N coordination than the *tert*-butyl substituents. In summary, the substituents on the chiral carbons of the oxazoline rings and on the bridging carbon backbone were found to affect the electron spin density of the resulting copper(II)-bis(oxazoline) structures.

5.5 References

1   McManus, H. A.; Guiry, P. J. *Chemical Reviews,* **2004**, *104*, 4151.

2   Ghosh, A. K.; Mathivanan, P.; Cappiello, J. *Tetrahedron: Asymmetry,* **1998**, *9*, 1.

3   Johannsen, M.; Joergensen, K. A. *The Journal of Organic Chemistry,* **1995**, *60*, 5757.

4   Evans, D. A.; Johnson, J. S.; Burgey, C. S.; Campos, K. R. *Tetrahedron Letters,* **1999**, *40*, 2879.

5   Balta, B.; Öztürk, C.; Aviyente, V.; Vincent, M. A.; Hillier, I. H. *The Journal of Organic Chemistry,* **2008**, *73*, 4800.

6   Evans, D. A.; Olhava, E. J.; Johnson, J. S.; Janey, J. M. *Angewandte Chemie International Edition,* **1998**, *37*, 3372.

7   Evans, D. A.; Peterson, G. S.; Johnson, J. S.; Barnes, D. M.; Campos, K. R.; Woerpel, K. A. *The Journal of Organic Chemistry,* **1998**, *63*, 4541.

8   Evans, D. A.; Johnson, J. S.; Olhava, E. J. *Journal of the American Chemical Society,* **2000**, *122*, 1635.

9   Taylor, S.; Gullick, J.; McMorn, P.; Bethell, D.; Bulman Page, P. C.; Hancock, F. E.; King, F.; Hutchings, G. J. *Topics in Catalysis,* **2003**, *24*, 43.

10   Evans, D. A.; Miller, S. J.; Lectka, T.; Von Matt, P. *Journal of the American Chemical Society,* **1999**, *121*, 7559.

11   Bolm, C.; Martin, M.; Gescheidt, G.; Palivan, C.; Stanoeva, T.; Bertagnolli, H.; Feth, M.; Schweiger, A.; Mitrikas, G.; Harmer, J. *Chemistry - A European Journal,* **2007**, *13*, 1842.

12   Evans, D. A.; Burgey, C. S.; Paras, N. A.; Vojkovsky, T.; Tregay, S. W. *Journal of the American Chemical Society,* **1998**, *120*, 5824.

13   Weil, J. A.; Bolton, J. R.; Wertz, J. E. *Electron Paramagnetic Resonance: Elementary Theory and Practical Applications*; John Wiley & Sons, Inc., **1994**.

14   Carter, E.; Hazeland, E. L.; Murphy, D. M.; Ward, B. D. *Dalton Transactions,* **2013**, DOI: 10.1039/C3DT51694F.

15   Kita, S.; Hashimoto, M.; Iwaizumi, M. *Inorganic Chemistry,* **1979**, *18*, 3432.

16   Lebel, H.; Parmentier, M.; Leogane, O.; Ross, K.; Spitz, C. *Tetrahedron,* **2012**, *68*, 3396.

17   Schweiger, A.; Jeschke, G. *Principles of Pulse Electron Paramagnetic Resonance*; Oxford University Press, **2001**.

Chapter 6

Probing the catalytic activity of a copper-bis(oxazoline) catalyst in an asymmetric aziridination reaction; An EPR investigation

6.1 Introduction

In chapters 4 and 5, EPR/ENDOR spectroscopy was used to study the structures of various copper-bis(oxazoline) complexes. Differences in the choice of counterion, substituents on the bridging carbon and the oxazoline rings, and in the number of ligands coordinated to the Cu(II) centre were investigated. Characterisation of these [Cu(II)(BOX)] complexes provides a foundation for the use EPR/ENDOR to further investigate the catalytic activity. Heteroleptic [Cu(BOX)](X)$_2$ complexes can catalyse a range of different reactions, including the Diels-Alder, cyclopropanation and aziridination reactions, thus earning them the title of 'privileged catalysts', as described in Section 1.4.

In this chapter, the [Cu(II)(**1a**)] (structure shown in Scheme 6.1) catalysed asymmetric aziridination reaction of styrene will be followed using EPR. The concept of asymmetric catalysis was previously explained in Section 1.3. In principle, EPR and ENDOR are powerful techniques that can assist in the analysis of privileged chiral catalysts, as demonstrated in recent publications by the Murphy group. The work presented in the current chapter relates to other EPR/ENDOR investigations of *privileged* chiral catalysts, for example based on the salen and Schiff ligands.[1-4] For example, the mode of chiral interactions between single enantiomers of methyl benzylamine with salen complexes containing either cobalt(II) or copper(II) centres, and between asymmetric expoxides with the VO(II) vanadyl analogue have been investigated.[1,2,4] Analysis of the EPR/ENDOR spectra in these investigations highlighted the importance of very weak outer-sphere interactions in influencing the stereoselectivities of enantioselective homogeneous catalysis. Hydrogen bonding, dipole-dipole, electrostatic and steric interactions were all found to play a key role in directing stereoselectivity through controlling the orientation of the substrate and stabilising the transition state, and these studies demonstrate the ability of ENDOR to detect these weak outer-sphere interactions.[1,2,4]
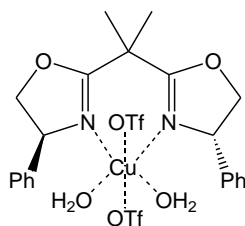
Scheme 6.1 Structure of the *privileged* chiral catalyst, [Cu(II)(**1a**)].

Aziridines are members of the saturated nitrogen heterocycle family on which a range of highly regio- and stereoselective ring opening reactions can be performed due to the high ring-strain energy.[5] For example, the ring opening of aziridine can be used to synthesise larger heterocycles.[5] Synthesis of aziridines is therefore of interest to chemists, and ring-closing reactions are commonly utilised for this purpose. Aziridine itself was first prepared from 2-chloroethylamine in 1888 in a ring-closing reaction, as shown in Scheme 6.2.[5]
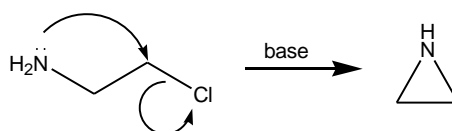
Scheme 6.2 The synthesis of aziridine by a ring-closing reaction.[5]

Another method for aziridine synthesis is the aziridination of alkenes (*e.g.,* styrene). This occurs through nitrene transfer to the double bond, using a 'nitrene' source such as [N-(*p*-tolylsulfonyl)imino]phenyliodinate (PhI=NTs) (Scheme 6.5). This reaction was discussed in detail in Section 1.6.1 and is again illustrated in Scheme 6.3.
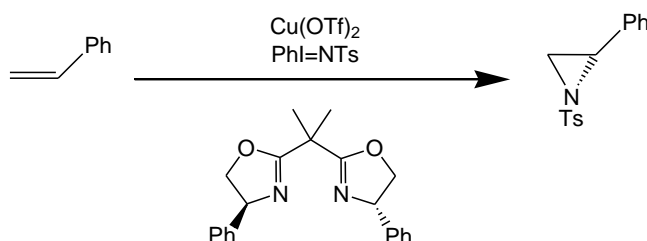
Scheme 6.3 Reaction scheme for the [Cu(BOX)](OTf)$_2$ catalysed aziridination of styrene (TfO$^-$ = CF$_3$SO$_3^-$, PhI=NTs = *p*-CH$_3$C$_6$H$_4$SO$_2$N=IPh)

Various mechanisms for the copper-catalysed alkene aziridination have been previously suggested in the literature and some of these were discussed in Section 1.6.1. It has been proposed by Jacobsen *et al.*,[6] that the Cu(I)-diimine catalysed reaction proceeds through a [L*Cu=NTs]$^+$PF$_6^-$ intermediate (using Cu(I)PF$_6$ as the starting salt) in a redox mechanism. Jacobsen *et al.*,[6] have also suggested an alternative in which the copper complex functions as a Lewis acid catalyst, although there is more supporting

evidence for their proposed redox mechanism. In the Lewis acid catalysis mechanism, the PhI is covalently attached to the active intermediate. On the basis of UV-Vis studies using Cu(I) and Cu(II) bis(oxazoline) complexes, Evans *et al.*,[7] argued that copper is in the +2 oxidation state when it functions as a catalyst, with PhI=NTs behaving as an oxidant for Cu(I). Díaz-Requejo and co-workers[8] also suggest the catalytically active species to be Cu(II). The pre-catalyst Tp'Cu(C$_2$H$_4$) (Tp' = hydridotris(3,5-dimethyl-1-pyrazolyl)borate) was investigated in combination with PhI=NTs and a series of *para*-substituted styrenes.[8] Their results suggest that the intermediate species which attacks styrene has some electrophilic character. It is proposed that this intermediate is a paramagnetic copper nitrene species, which behaves as an electrophilic, nitrogen-centred radical.[8] This intermediate structure is illustrated in Scheme 6.4.

$$\left[\overset{\oplus}{Tp'Cu}=\overset{..}{N}Ts \longleftrightarrow Tp'\overset{\oplus}{Cu}=\overset{.}{N}Ts \right]$$

Scheme 6.4 Paramagnetic copper nitrene intermediate, proposed by Díaz-Requejo *et al.*[8]

The aim of this chapter is therefore to gain a deeper understanding of the role of the copper catalyst in this reaction, and to further probe the reaction mechanism. EPR will be used for the first time in an effort to decipher the mechanistic details of the catalytic cycle. The interaction of substrates with the Cu(II) centre, any changes to the metal coordination number or any changes to the metal geometry during the course of the reaction will be monitored by EPR. This chapter will focus on utilising *X*-band CW-EPR, which provides valuable information on the **g** tensor and central metal hyperfine. It should be noted however that ENDOR is also a valuable technique for unravelling the catalytic mechanisms of homogeneous asymmetric catalysts based on paramagnetic transition metal complexes.[9] ENDOR is particularly useful for investigating the mode of chiral transfer between substrate and ligand, through the detection of weak inner- and outer-sphere substrate-ligand interactions.[9] Using a combination of advanced EPR techniques can provide qualitative and quantitative information on the composition, as well as providing a deeper understanding of the structure and bonding of the active site throughout the catalytic cycle.[9] Isolation and identification of the paramagnetic reaction intermediates can even be achieved in some cases.[9]

In this investigation, EPR will firstly be used to analyse the interaction of [Cu(II)(**1a**)] with the addition of a single substrate, including pyridine, iodobenzene, (diacetoxyiodo)benzene, PhI=NTs and styrene. This is the first step towards understanding the aziridination reaction which involves the addition of both styrene and PhI=NTs. After exploring the effect of individual substrate addition, the progress of the

aziridination reaction itself will be investigated by recording the EPR spectra at different time intervals after substrate addition. Integration of the EPR signals can provide insights into any change in the concentration of paramagnetic species (in this case Cu(II)) during the course of the reaction, which may suggest a change to the copper oxidation state. Changes to the spin Hamiltonian parameters could imply that there is a change in the geometry or electron spin distribution of the copper complex and evidence of additional paramagnetic species may be indicative of the formation of a reaction intermediate involving a paramagnetic Cu(II) centre.

6.2 Experimental

Full details of the experimental methods were given in Chapter 3, hence only a brief description is given here.

The synthesis of PhI=NTs was performed according to the method of Yamada *et al.*,[10] to give N-tosyliminophenyliodinane (60 – 70% yield). ^{1}H NMR (d^6-DMSO): δ 7.73-7.16 (m, 9H, Ph), 2.37 (s, 3H, Me). The general method for the aziridination reaction used was that described by Hutchings *et al.*[11] The substrates which have been used in this chapter are illustrated in Scheme 6.5.

| Iodobenzene | Pyridine | Styrene | Cyclohexene |

(Diacetoxyiodo)benzene   [N-(*p*-tolylsulfonyl)imino]phenyliodinate (PhI=NTs)
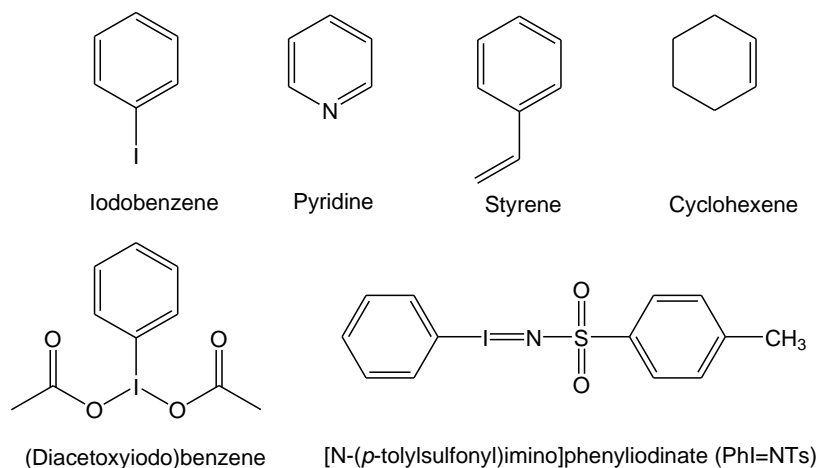
Scheme 6.5 Substrates used to investigate the effect of substrate addition on the EPR profile of [Cu(II)(**1a**)]. Styrene and PhI=NTs are used in the asymmetric aziridination reaction.

All *X*-band EPR spectra were recorded on a Bruker EMX spectrometer equipped with a high sensitivity *X*-band cavity (ER 4119HS). The CW *Q*-band ENDOR spectra were recorded at 10 K on a CW Bruker ESP 300E series spectrometer equipped with an ESP360 DICE ENDOR unit, in a *Q*-band ENDOR cavity (Bruker ER 5106 QT-E). The pulsed *X*-band EPR/ENDOR spectra were recorded on a Bruker Elexsys E580 spectrometer equipped with a liquid Helium cryostat from Oxford Inc.

6.3 Results and Discussion

6.3.1 CW-EPR of [Cu(II)(1a)] upon substrate addition

Interaction of various substrates with Cu(II) complexes can be monitored using EPR spectroscopy. In order to investigate how substrate addition can affect the EPR profile of the [Cu(II)(1a)] complex, a 10-fold excess of pyridine (C_5H_5N) was added to a solution of [Cu(II)(1a)] in MeOH:Tol. Pyridine is a basic (pK_{aH} 5.2) six membered heterocycle, with one aromatic nitrogen, and has been used for this preliminary investigation since it is a very unreactive but strongly coordinating substrate.[5] The low reactivity of pyridine is an important property for this investigation in order to observe the substrate interaction with the Cu(II) centre in conditions similar to those used catalytically but without any reaction occurring which may otherwise be incurred during the catalytic reaction (for example changes to the oxidation state of the metal centre). Figure 6.1a shows the initial EPR spectrum of [Cu(II)(1a)] in the absence of pyridine and Figure 6.1b shows the resulting spectrum after the addition of pyridine, along with the corresponding simulations in red. The roadmap of Figure 6.1b, after the addition of pyridine, is shown below the EPR spectra (blue line).

Additional well defined superhyperfine splitting is clearly evident in the perpendicular direction upon addition of a ten-fold excess of pyridine. This is due to the interaction of the unpaired electron with the spin active ($I = 1$) nitrogen of the coordinated pyridine. The spectrum has been simulated using three ^{14}N nuclei (including two from the BOX ligand itself), suggesting that one pyridine molecule interacts with the Cu(II) centre in [Cu(II)(1a)]. Both nitrogen ligand nuclei of the bis(oxazoline) complex have been simulated using the hyperfine couplings determined by ENDOR in Chapter 4. The nitrogen of the interacting pyridine has been simulated using values of $A_1 = 37$ MHz, $A_2 = 43$ MHz (± 3 MHz) and $A_3 = 41$ MHz (± 6 MHz). The ^{14}N superhyperfine splitting in the parallel region is unresolved in Figure 6.1b (after pyridine addition) and therefore it is difficult to accurately determine this value of A_3. Considering the structure of [Cu(II)(1a)], it is possible that the pyridine molecule replaces either an equatorially coordinated water molecule or an axially coordinated triflate molecule (Section 4.3.3). However, the additional superhyperfine splitting which is observed in the perpendicular region is implicative of equatorially coordinated pyridine, since no additional superhyperfine splitting would be observed should the pyridine be coordinating in the axial direction.[12,13] This therefore suggests that the pyridine molecule replaces a water molecule in [Cu((II))(1a)].
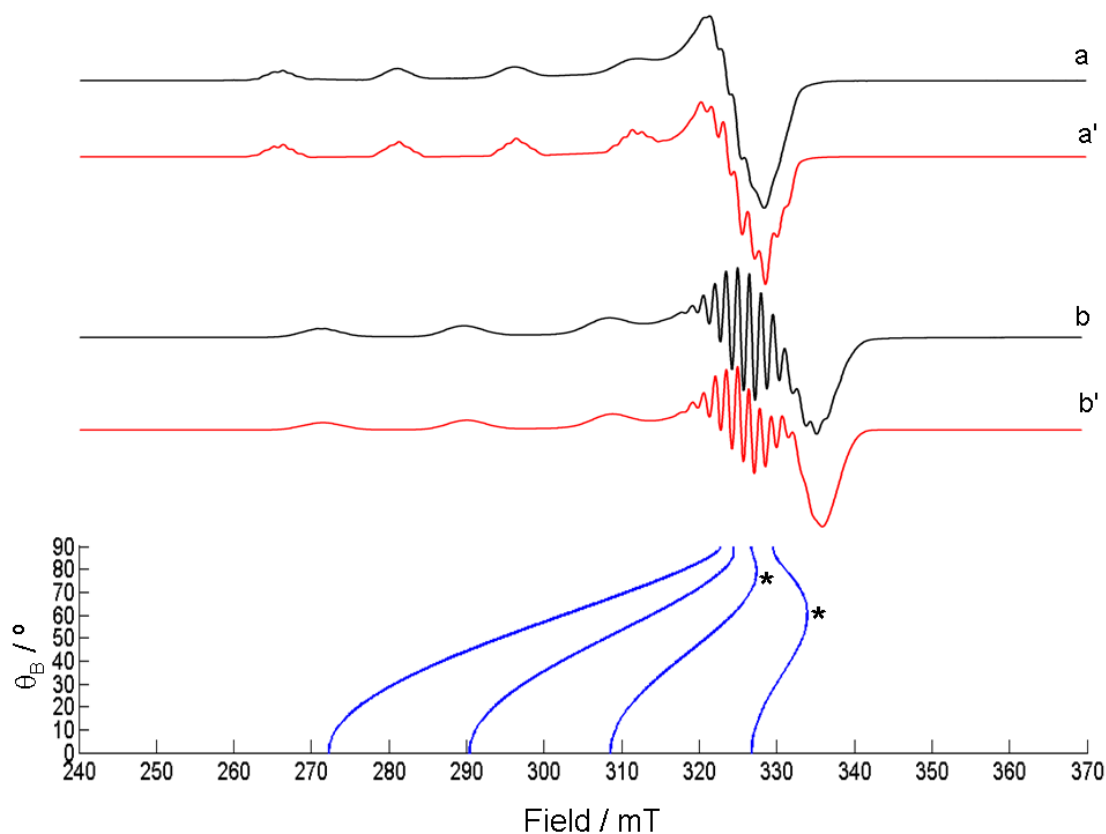
Figure 6.1 *X*-band CW-EPR spectra (140 K) of a) [Cu(II)(**1a**)] dissolved in MeOH:Tol (solvent ratio 4:3) and b) after the addition of a 10-fold excess of pyridine. The corresponding simulations are given in a' and b' (red line). The roadmap corresponding to (b) is shown in blue, with the overshoot features labelled *.

A study by Wagner and Walker,[14] of Schiff base ligands (derived from salicylaldehyde and glycine / acetyllysine) also showed that an equatorially coordinated water molecule was displaced upon addition of pyridine. Their EPR results were in agreement with the Peisach-Blumberg plots, *i.e.*, that $g_\parallel$ decreased slightly in the presence of pyridine, as expected when a nitrogen atom replaces an oxygen atom in the equatorial donor set.[14,15] This was also expected to be the case upon addition of pyridine to [Cu(II)(**1a**)] and was confirmed as g_3 ($g_\parallel$) decreased from 2.321 to 2.239. g_1 and g_2 also decreased in value, from 2.064 to 2.055 and from 2.073 to 2.042 for g_1 and g_2 respectively (see Table 6.1). The A_3 parameter increased upon pyridine addition (from 488 to 564 MHz), which is again consistent with the trend expected from the Peisach-Blumberg plots. This supports the conclusion that the pyridine has replaced one of the equatorially coordinated water molecules and therefore illustrates the utility of EPR to easily monitor changes in the metal complex coordination sphere by interaction with nitrogen bases.

The angular dependency profile (roadmap) of [Cu(II)(**1a**)] + pyridine, reveals that the decrease in g_3 has resulted in additional features in the EPR spectrum at high

field. These are most noticeable for the $m_I = -3/2$ transition (and less obviously at the $m_I = -1/2$ transition). These features are referred to as the "overshoot" or "off-axis field orientations" and are highlighted in the roadmap with asterisks (Figure 6.1). They arise from angular anomalies resulting from the relatively large anisotropy in the principal g values combined with large hyperfine splittings, particularly in the perpendicular region of the spectrum.[16] These angular anomalies, or "off-axis extrema" do not correspond to resonances from the principal directions.[17] Instead, they originate at angles in between the principal axes.[16] These effects are common in X-band powder EPR spectra, particularly in Cu(II) complexes. However they are not limited to transition metal ions and may be present in any spectrum in which the g and A anisotropy is relatively large.[13] Recording higher frequency EPR spectra (such as Q-band or W-band) can aid in the simulation of EPR spectra which display angular anomalies.[16]

Figure 6.2a shows the spectrum of [Cu(II)(**1a**)] in AcN:DMF (4:1) prior to substrate addition, with the expanded parallel region shown in Figure 6.3a. As coordinating solvents, both methanol and acetonitrile are suitable for use in these investigations. The addition of toluene / DMF is simply used to improve the glass quality in the frozen solutions. Hutchings *et al.*,[11] have expressed the importance of the use of coordinating solvents for the homogeneous [Cu(II)(BOX)] catalysed asymmetric aziridination of styrene, using PhI=NTs as the nitrene donor. They reported high *ee* of greater than 70% when the reaction was performed only in acetonitrile or methanol, with lower *ee* values in non-coordinating solvents. Evans *et al.*,[18] also examined solvent effects in the copper-catalysed aziridination of styrene with PhI=NTs. The authors reported excellent yields of aziridine in both polar and nonpolar media for this reaction. However when investigating less reactive substrates, both the reaction rate and the efficency of the reaction were found to improve in more polar solvents such as acetonitrile.[18]

Table 6.1 Experimental g and A^{Cu} spin Hamiltonian parameters for [Cu(II)(**1a**)] with the addition of a ten-fold excess of substrate.

Complex	Species	$^a g_1$	$^a g_2$	$^a g_3$	$^b A_1$	$^b A_2$	$^c A_3$	^{d}Solvent
Cu(II)(OTf)$_2$		2.083	2.083	2.412	13	13	403	A
[Cu(II)(**1a**)]		2.064	2.073	2.321	15	15	488	B
[Cu(II)(**1a**)]		2.064	2.073	2.315	15	15	491	C
Substrate addition to [Cu(II)(1a)]*								
Pyridine		2.055	2.042	2.239	63	63	564	B
Iodobenzene		2.067	2.076	2.319	15	15	487	C
(Diacetoxy)-iodobenzene	**I**	2.064	2.075	2.318	15	15	487	C
	II	2.064	2.075	2.397	49	23	402	
Styrene		2.064	2.074	2.317	15	15	491	C
PhI=NTs		2.064	2.073	2.321	15	15	488	B

* Substrate added to [Cu(II)(**1a**)] in ten-fold excess (with respect to [Cu(II)(**1a**)]). All A values given in MHz; [a] ±0.004; [b] ±3 MHz; [c] ±6 MHz. [d]Solvent A = 50% THF, 50% DCM; solvent B = 57% MeOH, 43% Tol; solvent C = 80% AcN, 20% DMF. For (diacetoxy)iodobenzene, **I** = primary species (~95%) and **II** = secondary species (~5%), as determined *via* simulation.
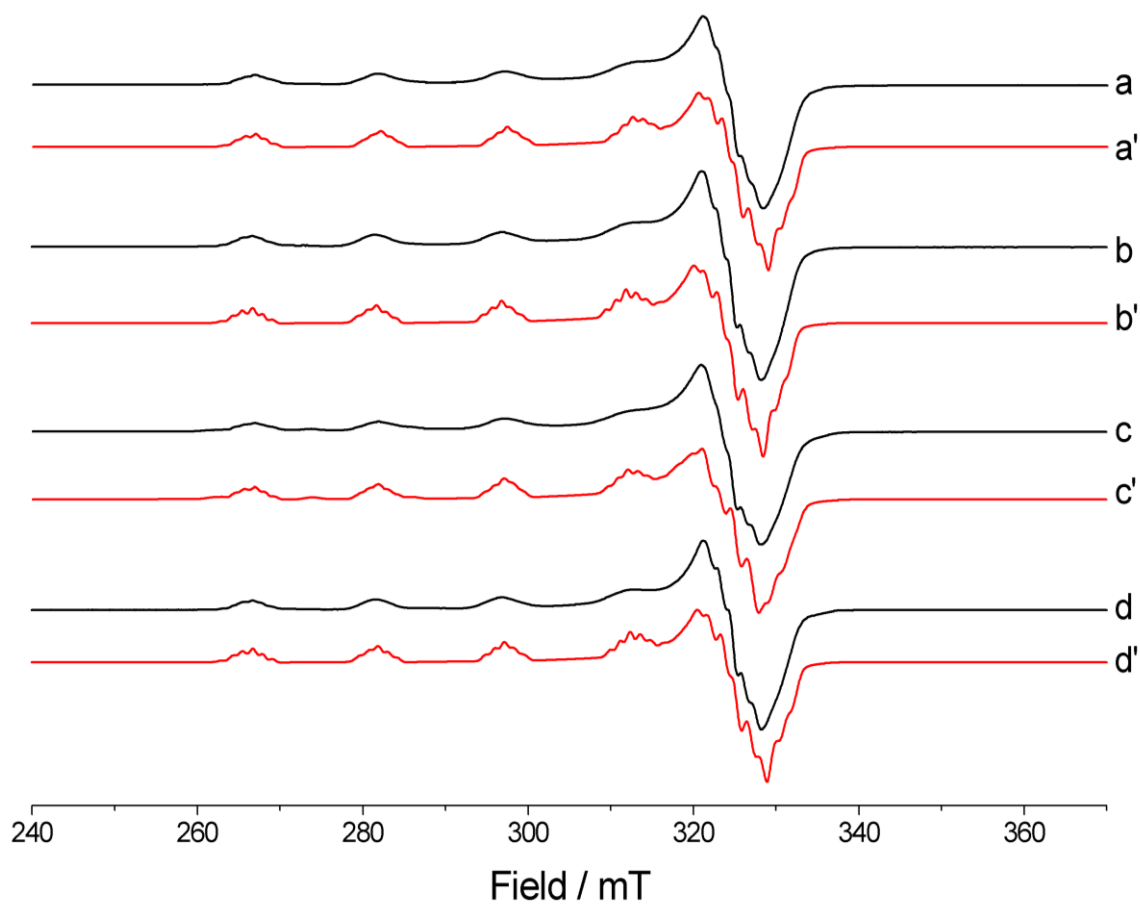
Figure 6.2 *X*-band CW-EPR spectra (140 K) of a) [Cu(II)(**1a**)] dissolved in AcN:DMF (4:1) and after addition of a 10-fold excess of b) iodobenzene, c) (diacetoxyiodo)benzene and d) styrene. The corresponding simulations are given in a'-d' (red line).
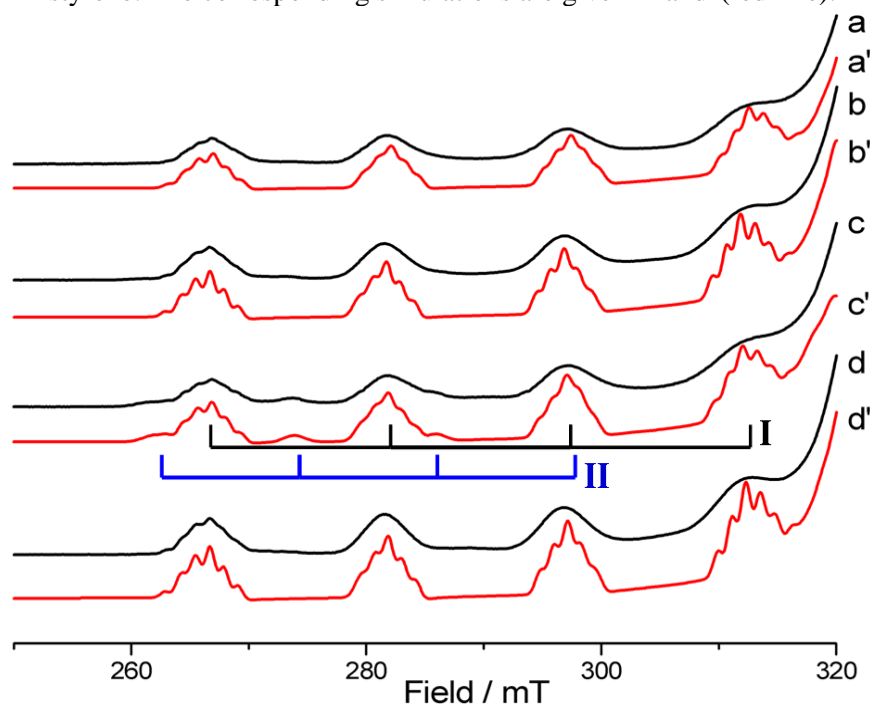
Figure 6.3 *X*-band CW-EPR spectra (140 K) of a) [Cu(II)(**1a**)] dissolved in AcN:DMF (4:1) and after addition of a 10-fold excess of b) iodobenzene, c) (diacetoxyiodo)benzene and d) styrene, highlighting the parallel region. The corresponding simulations are given in a'-d' (red line).

As a result of the changes observed in the EPR profile upon addition of pyridine, the interaction of iodobenzene (PhI) with [Cu(II)(**1a**)] was also examined. Iodobenzene is of particular interest as it is a fragment of the PhI=NTs nitrene donor used in the aziridination reaction and may therefore be regarded as a reaction intermediate. Indeed, in the Lewis acid catalysis mechanism proposed by Jacobsen *et al*.,[6] it is suggested that the PhI covalently attaches to an active intermediate. However, it is stated that their first proposed redox mechanism, in which the PhI is fully dissociated from the aziridine ring, has more supporting evidence.[6] From the EPR spectrum found in this investigation, no significant change is evident upon addition of excess iodobenzene to [Cu(II)(**1a**)] (Figures 6.2b, 6.3b). The simulation parameters listed in Table 6.1 also highlight this; the g and A values of [Cu(II)(**1a**)], and [Cu(II)(**1a**)] + iodobenzene are very similar. Since no interaction is evident between [Cu(II)(**1a**)] and iodobenzene when they are mixed directly, this could imply that it is unlikely that the reaction intermediate in the asymmetric aziridination reaction is an adduct of [Cu(II)(**1a**)] and iodobenzene.

As well as adding iodobenzene to [Cu(II)(**1a**)], the addition of the related (diacetoxyiodo)benzene (PhI(OAc)$_2$) was also investigated. This compound is used as a starting material in PhI=NTs synthesis. Figures 6.2c and 6.3c show the resulting spectrum after the addition of a 10-fold excess of (diacetoxyiodo)benzene. Here the presence of a small percentage of an additional species is evident. Both the primary species, labelled (**I**) in Figure 6.3c, and the additional species, labelled (**II**), have been simulated (see Table 6.1). Simulation revealed that species **II** is present at approximately 5% of the sample concentration (Table 6.1). The primary species (**I**) has the same spin Hamiltonian parameters as [Cu(II)(**1a**)] in AcN:DMF prior to substrate addition. However, the secondary species (**II**) is very different, largely in the parallel region; *i.e.*, g_3 is significantly larger, with a value of 2.397 (*cf*. 2.318) whilst A_3 is significantly smaller, with a value of 402 MHz (*cf*. 487 MHz). These changes in the hyperfine parameters of species **II** from [Cu(II)(**1a**)] could indicate axially coordinated substrates. Since the addition of iodobenzene to [Cu(II)(**1a**)] did not result in the formation of a second species, it can be suggested that the presence of the AcO$^-$ groups affects the coordination to the copper centre. It may be that these groups (in the presence of protic solvent) dissociate from the PhI and are protonated to form acetic acid (AcOH). Due to the absence of the Ph group, AcOH is likely to be small enough to interact with the Cu(II) centre. This could be tested by recording the EPR spectrum of [Cu(II)(**1a**)] with acetic acid. However it should also be noted that by comparison of the spin Hamiltonian parameters of species **II** and Cu(II)(OTf)$_2$, it is evident that the A_3 and

g_3 tensors are very similar. Accurate simulation of A_1, A_2, g_1 and g_2 for species **II** is difficult because these features cannot be distinguished in the perpendicular region against the more prominent species **I**. It is therefore also possible that these additional peaks are simply due to the presence of excess Cu(II)(OTf)$_2$.

Styrene (C$_6$H$_5$CH=CH$_2$) (the olefin used in the asymmetric aziridination reaction illustrated in Scheme 6.3) was then added to [Cu(II)(**1a**)]. No significant change was evident in the spectrum after the addition of styrene (Figures 6.2d, 6.3d). The simulation parameters (Table 6.1) of the sample after styrene addition are not significantly different to those of [Cu(II)(**1a**)] alone. This shows that the addition of styrene alone does not affect the composition, structure or bonding of the copper catalyst. Considering the redox aziridination mechanism proposed by Jacobsen *et al*.,[6] it is unsurprising that there is no evidence of interaction between the styrene and [Cu(II)(**1a**)] in the absence of PhI=NTs as the nitrene source. As mentioned above, Jacobsen *et al*.,[6] propose that it is probable that a discrete Cu(III)-nitrene intermediate is formed by the dissociation of PhI from the aziridinating species. It is suggested that the olefin (styrene) interacts with this Cu(III)-nitrene intermediate, as opposed to the Cu(II) catalyst itself.[6] Díaz-Requejo and co-workers also suggest that the catalytically active species is a copper nitrene species, albeit they propose a paramagnetic copper nitrene species (Scheme 6.4).[8] Interestingly, Brandt *et al*.,[19] suggest that a mixture of catalyst (a Cu(I)-diimine complex) with alkene prior to the initiation of the catalyst cycle, results in the reversible formation of a Cu(I)-alkene complex. It may be that a reversible copper-alkene complex is indeed formed upon addition of styrene to [Cu(II)(**1a**)] but that this occurs within a timescale not accessible by EPR.

After investigating the effect of addition of pyridine, iodobenzene, (diacetoxyiodo)benzene and styrene on the EPR profile of [Cu(II)(**1a**)], the addition of the nitrene donor (PhI=NTs) in the aziridination reaction illustrated in Scheme 6.3 was investigated. The effect of changing the stirring time has been studied, by varying the time from 30 minutes to 180 minutes. These results are shown in Figure 6.4, with Figure 6.4a showing the EPR spectrum of [Cu(II)(**1a**)] prior to substrate addition, and 6.4b-g showing the resulting spectra after PhI=NTs addition, with increased stirring time. These spectra have been integrated (Figure 6.5) in order to observe any changes to the Cu(II) concentration. Figure 6.6 shows both the experimental and simulated spectra of [Cu(II)(**1a**)] after addition of a 10-fold excess of PhI=NTs and 180 minutes stirring. The simulation parameters used are listed in Table 6.1.

It is evident in Figure 6.4a-g that no significant changes occur in the EPR profile of [Cu(II)(**1a**)] upon addition of a ten-fold excess of PhI=NTs with stirring times varying from 30 to 180 minutes. The spectra show some evidence of a second paramagnetic Cu(II) species, highlighted with the asterisks in Figure 6.4B. However it should be noted that this additional hyperfine pattern is present in the spectrum of [Cu(II)(**1a**)] prior to PhI=NTs addition. The hyperfine parameters of this additional feature suggest that these peaks are simply due to excess Cu(II)(OTf)$_2$. The EPR spectrum shown in Figure 6.6, for which the sample contained a 1:10 ratio of [Cu(II)(**1a**)]:PhI=NTs, (stirred for 180 minutes) was simulated using identical parameters to [Cu(II)(**1a**)] without the addition of PhI=NTs (see Table 6.1). This simulation therefore implies that PhI=NTs addition does not affect the *X*-band EPR profile of [Cu(II)(**1a**)], even when added in a 10-fold excess and after being stirred for 180 minutes. PhI=NTs is clearly different in structure compared to pyridine previously studied in Figure 6.1 since the nitrogen of pyridine is nucleophilic whilst PhI=NTs is a reactive intermediate with an electrophilic nitrogen. This is a significant difference and is likely to contribute to the dramatic changes in the EPR profile resulting from the interaction of pyridine with the electron deficient Cu(II) centre (Figure 6.1), as opposed to there being no evidence of interaction with PhI=NTs when added in a ten-fold excess.

As evidenced in Figure 6.5, there appears to be no clear relationship between the integrated signal intensity and the reaction time after addition of PhI=NTs. This implies that there is no significant change in [Cu(II)] concentration with stirring time up to 180 minutes. Considering again the mechanism proposed by Jacobsen *et al.*,[6] it is surprising that the EPR profile and signal intensity does not change more significantly upon addition of PhI=NTs. In the proposed redox mechanism, PhI=NTs addition results in the formation of the discrete Cu(III)-nitrene as the reactive intermediate, and therefore a sharp decrease in the Cu(II) concentration would be expected as a result of this change in oxidation state. In the case of the formation of a Cu(II)-nitrene intermediate, as proposed by Díaz-Requejo *et al.*,[8] substantial changes to the hyperfine parameters or evidence of the formation of a second paramagnetic species would be expected. It is likely however that formation of a copper-nitrene intermediate species occurs only in the presence of both olefin and nitrene source. It is also possible that the intermediate is unstable and persists on a timescale too fast to be observed by EPR. Unfortunately therefore, clarification of the mechanism of the copper catalysed aziridination reaction has not been achieved by the results collected from addition of a ten-fold excess of PhI=NTs to [Cu(II)(**1a**)] with stirring times up to 180 minutes (Figures 6.4-6.6).
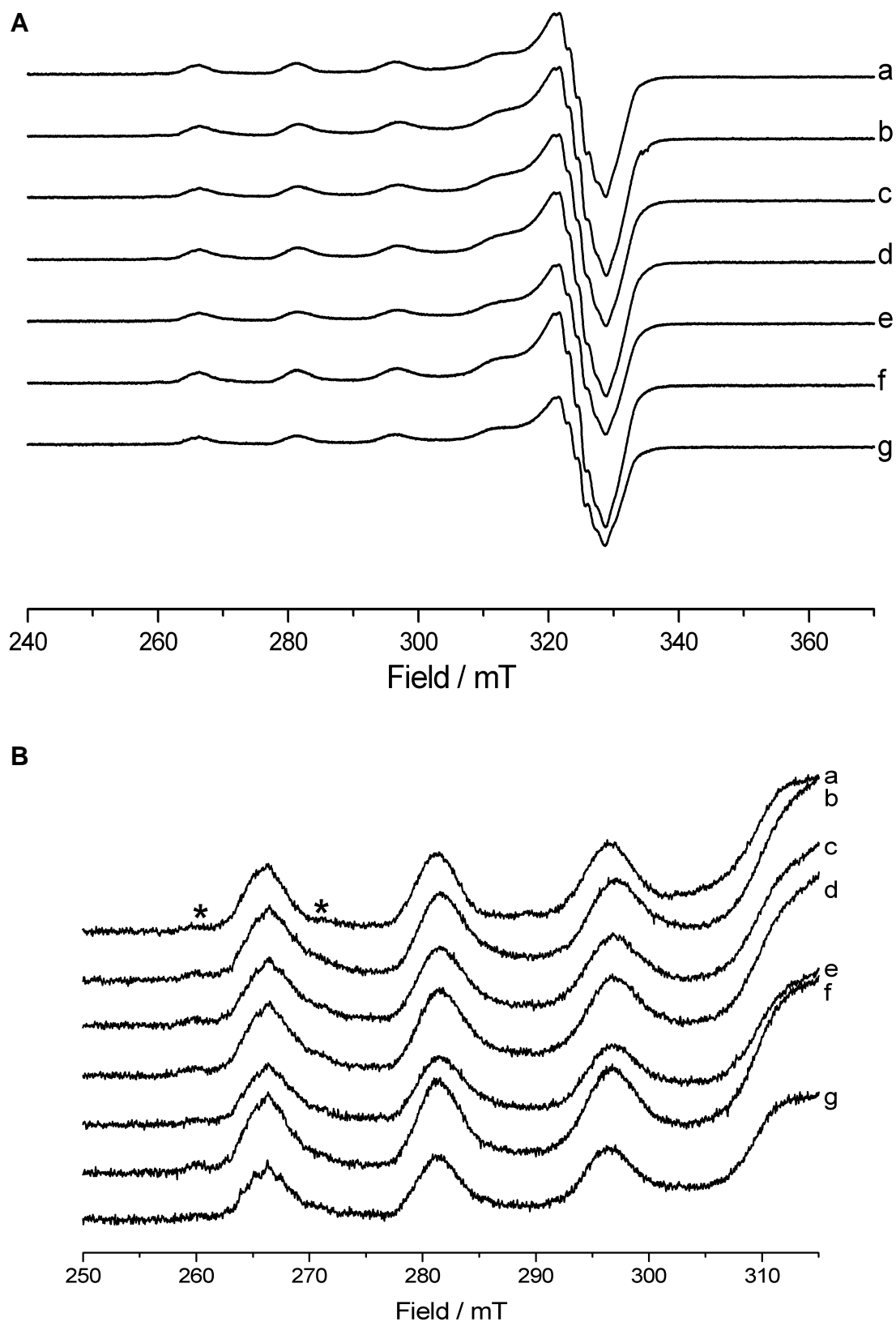
Figure 6.4 X-band CW-EPR spectra (140 K) of a) $[Cu(II)(\mathbf{1})](OTf)_2$ dissolved in MeOH:Tol (4:3) with b-g) 10-fold excess of PhI=NTs. After addition of PhI=NTs the samples were stirred for b) 30, c) 60, d) 90, e) 120, f) 150, and g) 180 mins. The parallel region is highlighted in (B) for clarity. * highlights the additional features evident in this series of spectra which have been attributed to excess $Cu(II)(OTf)_2$.
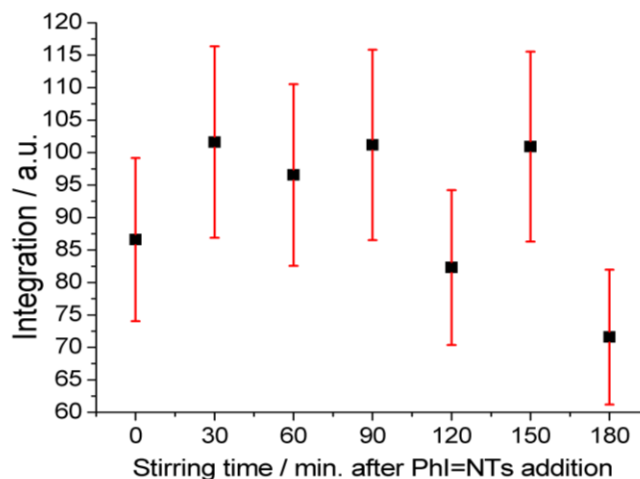
Figure 6.5 Integrated EPR signal intensities for [Cu(II)(**1a**)] + PhI=NTs with increased stirring time. Error bars (±15%) are shown in red.
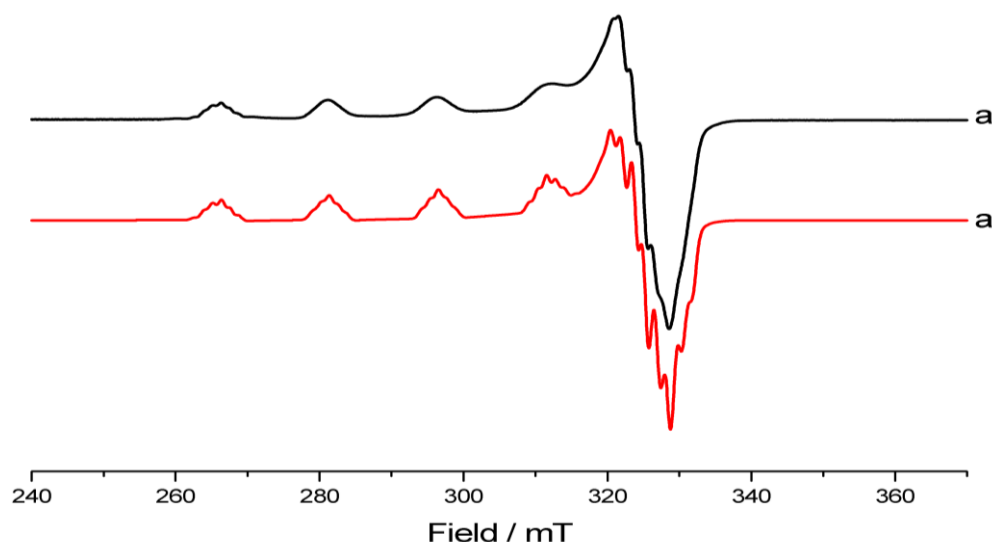
Figure 6.6 *X*-band CW-EPR spectra (140 K) of a) [Cu(II)(**1a**)] dissolved in MeOH:Tol (4:3) with a 10-fold excess of PhI=NTs (stirred for 180 minutes). The corresponding simulation is given in a' (red line).

Due to the lack of any change in the EPR profile upon addition of a ten-fold excess of PhI=NTs, the effect of increasing the ratio of PhI=NTs has been studied in order to determine whether this shifts the binding equilibrium towards the formation of a possible adduct of [Cu(II)(**1a**)] + PhI=NTs (or the nitrene moiety of PhI=NTs). Figure 6.7 presents the EPR spectra of [Cu(II)(**1a**)] upon addition of increasing amounts of PhI=NTs, from a ten-fold excess to a hundred-fold excess (after stirring for 180 minutes). Again, these spectra have been integrated (Figure 6.8) in order to monitor any change to the overall [Cu(II)] concentration. There is again some evidence of excess $Cu(II)(OTf)_2$ in this series of investigations, highlighted with asterisks in Figure 6.7B. Whilst the spin Hamiltonian parameters did not change after addition of the large excess

of PhI=NTs, the integration plot (Figure 6.8) appears to show a systematic trend of decreasing [Cu(II)] concentration with increasing equivalents of PhI=NTs. It is evident from the EPR spectra in Figure 6.7 that this decrease in intensity is noticeable, albeit relatively small. This could suggest that the addition of PhI=NTs does result in the oxidation of the Cu(II) centre to form a Cu(III) complex, such as the Cu(III)-nitrene proposed by Jacobsen et al.[6] However, it must be emphasised that this investigation was performed in the absence of the olefin (styrene), which is required for the aziridination reaction. Having investigated the addition of individual substrates to [Cu(II)(**1a**)], the aziridination reaction, with the addition of both styrene and PhI=NTs will be considered in Section 6.3.2.
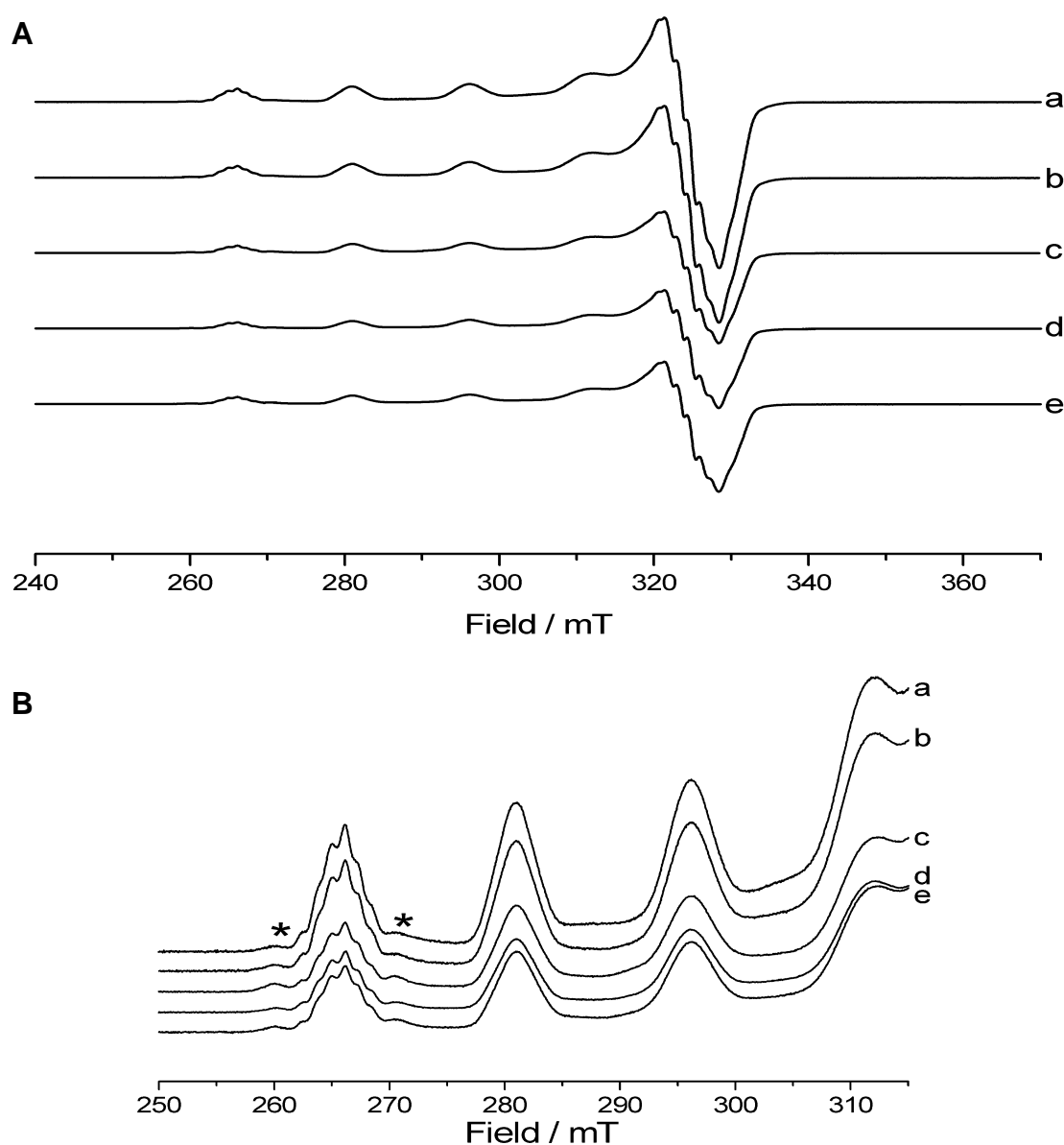
Figure 6.7 *X*-band CW-EPR spectra (140 K) of a) [Cu(II)(**1a**)] in MeOH:Tol (4:3) after addition of PhI=NTs, in increasing quantities of b) 10-fold, c) 30-fold, d) 50-fold and e) 100-fold. The parallel region is highlighted in (B) for clarity. * highlights the additional features, which have been attributed to excess Cu(II)(OTf)$_2$.
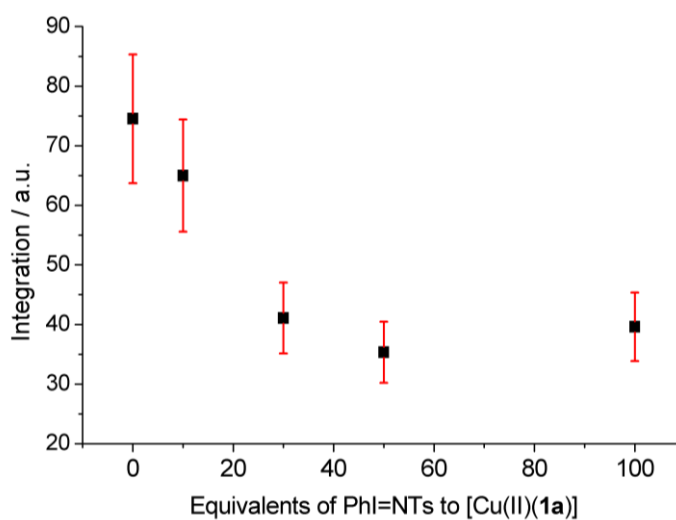
Figure 6.8 Integrated EPR signal intensities for [Cu(II)(**1a**)] + increasing equivalents of PhI=NTs. Error bars (±15%) are shown in red.

*6.3.2 CW-EPR of [Cu(II)(**1a**)] catalysed asymmetric aziridination reaction*

After probing the effect of the addition of several substrates independently, the aziridination reaction itself, based on the addition of both styrene (the olefin) and PhI=NTs (the nitrene donor) was investigated. Figure 6.9a shows the EPR profile of [Cu(II)(**1a**)] prior to substrate addition, whilst Figure 6.9b shows the resulting profile after the addition of styrene and PhI=NTs after five hours stirring time.

Taking into account both the spectra shown in Figure 6.9 and the spin Hamiltonian parameters listed in Table 6.2, it is evident that upon addition of styrene and PhI=NTs a second paramagnetic species is formed. This is illustrated with a stick diagram in Figure 6.9b' and has been labelled species **III** for clarity. The change in g_3 and A_3 after the addition of PhI=NTs + styrene to [Cu(II)(**1a**)] reflects the trend previously observed in the EPR spectrum of [Cu(II)(**1a**)] upon addition of pyridine; *i.e.*, a decrease in g_3 and increase in A_3. This suggest that there is a change in the equatorial environment of the copper complex. As discussed previously, Jacobsen *et al.*,[6] have proposed a redox reaction mechanism in which the nitrene moiety of the PhI=NTs coordinates to the copper forming a discrete Cu(III)-nitrene as the reactive intermediate. The results shown in Figure 6.9 could suggest that there is a degree of interaction between the nitrene moiety and Cu(II), which could explain the presence of species **III**. This may be in agreement with the paramagnetic copper-nitrene intermediate (Scheme 6.4) proposed by Díaz-Requejo *et al.*[8] However, no additional superhyperfine resolution can be resolved in the EPR profile of species **III** (Figure 6.9), which would be expected upon the presence of an additional interacting ^{14}N nucleus ($I = 1$) in the equatorial plane. This may be simply due to the broadness of the absorptions and the fact that they

are overlapping with the EPR profile of [Cu(II)(**1a**)]. Accordingly, it must also be considered that species **III** could in fact be due to an interaction of [Cu(II)(**1a**)] with styrene.
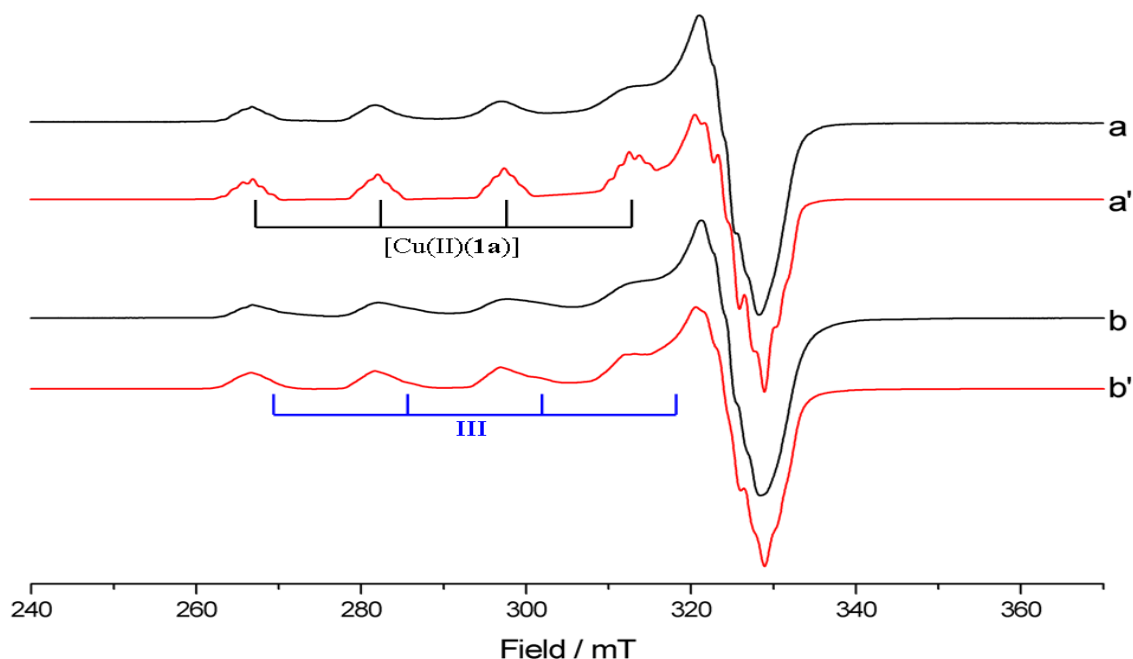
Figure 6.9 *X*-band CW-EPR spectra (140 K) of a) [Cu(II)(**1a**)] dissolved in AcN:DMF (4:1) and b) after the addition of styrene and PhI=NTs with 5 hours stirring. The corresponding simulations are given in a' – b' (red line).

Table 6.2 Experimental *g* and A^{Cu} spin Hamiltonian parameters for [Cu(II)(**1a**)] in AcN:DMF (4:1), and after the addition of PhI=NTs and styrene after 5 hours stirring.

Rxn. time / hours	Species	Relative % of species	$^a g_1$	$^a g_2$	$^a g_3$	$^b A_1$	$^b A_2$	$^c A_3$
0	[Cu(II)(**1a**)]	100	2.064	2.073	2.315	15	15	491
5	[Cu(II)(**1a**)]	56	2.064	2.073	2.320	15	14	487
	III	44	2.064	2.073	2.292	15	14	513

All *A* values given in MHz; [(a)] ±0.004; [(b)] ±3 MHz; [(c)] ±6 MHz. Solvent = 80% AcN, 20% DMF. Species **III** is illustrated with a stick diagram in Figure 6.9b'.

The formation of this second paramagnetic species (**III**) was further investigated in the study shown in Figure 6.10, but for this investigation a solvent system of MeOH:Tol was used instead of AcN:DMF. This change to the solvent system was made in order to ensure that the formation of species **III** is not exclusive to the reaction performed in acetonitrile. As mentioned previously, both methanol and acetonitrile are suitable for use in these investigations since they are coordinating solvents. In this investigation, aliquots of the reaction mixture were extracted after different stirring

times in order to monitor the course of the reaction. The resulting EPR spectra are shown in Figure 6.10, with the corresponding integrations shown in Figure 6.11 and the simulation parameters are listed in Table 6.3.
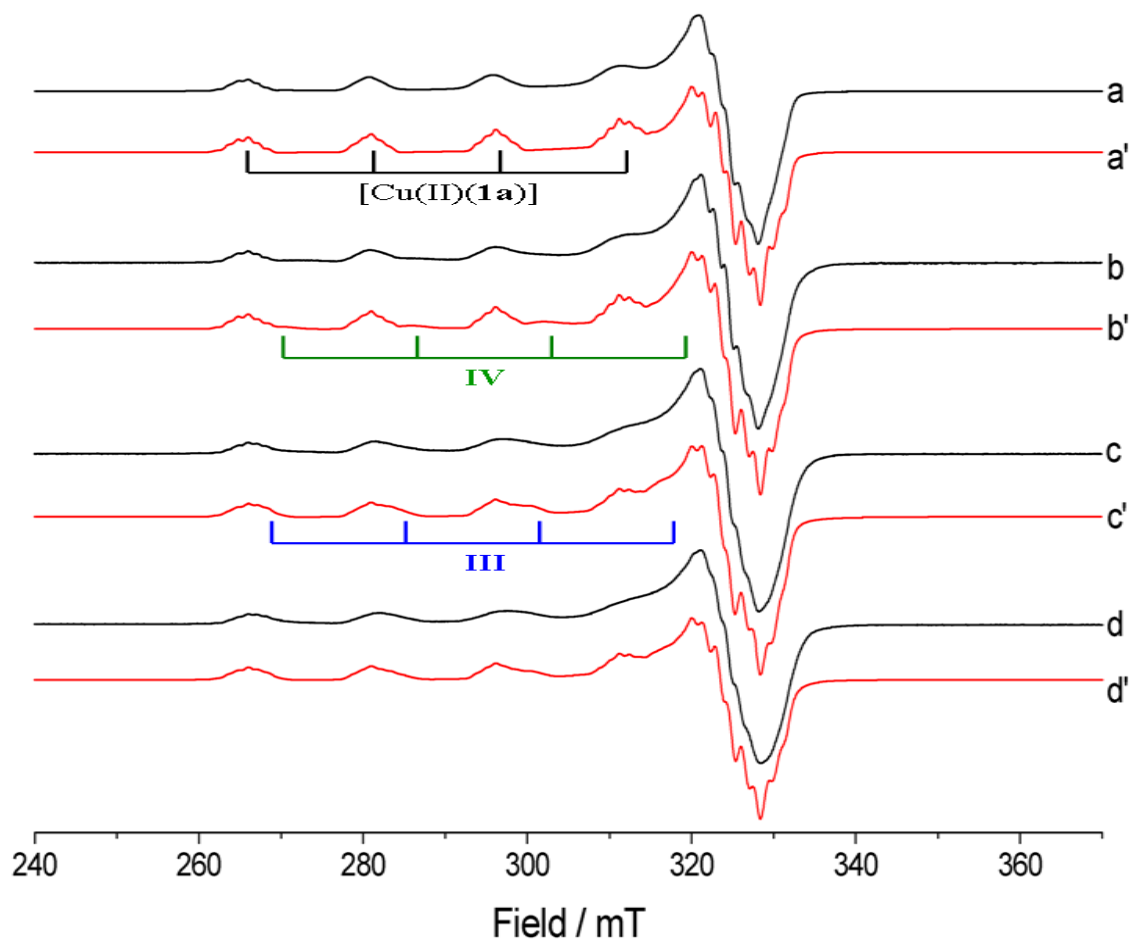
Figure 6.10 *X*-band CW-EPR spectra (140 K) of a) [Cu(II)(**1a**)] in MeOH:Tol (4:3) and after the addition of styrene and PhI=NTs after b) 5 minutes, c) 25 minutes and d) 45 minutes stirring. The corresponding simulations are given in a'-d' (red line).
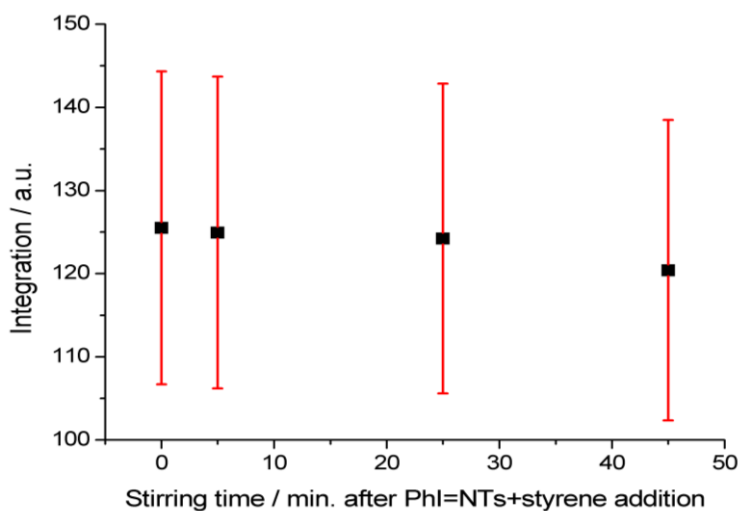
Figure 6.11 Integrated EPR signal intensities for [Cu(II)(**1a**)] + PhI=NTs + styrene with increased stirring time. Error bars (±15%) are shown in red.

Table 6.3 Experimental g and A^{Cu} spin Hamiltonian parameters for [Cu(II)(**1a**)] in MeOH:Tol (4:3), and after the addition of PhI=NTs and styrene with increasing reaction time.

Rxn. time / mins.	Species	Relative % of species	$^a g_1$	$^a g_2$	$^a g_3$	$^b A_1$	$^b A_2$	$^c A_3$
0	[Cu(II)(**1a**)]	100	2.064	2.073	2.321	15	15	488
5	[Cu(II)(**1a**)]	77	2.064	2.073	2.321	15	15	488
	IV	23	2.064	2.073	2.280	15	15	511
25	[Cu(II)(**1a**)]	63	2.064	2.073	2.321	15	15	488
	III	38	2.064	2.073	2.292	15	15	513
45	[Cu(II)(**1a**)]	63	2.064	2.073	2.321	15	15	488
	III	38	2.064	2.073	2.292	15	15	513

All A values given in MHz; [(a)] ±0.004; [(b)] ±3 MHz; [(c)] ±6 MHz. Species **III** and **IV** are illustrated with stick diagrams in Figure 6.10.

In Figure 6.10, a change is observed in the EPR profile upon addition of styrene and PhI=NTs after only 5 minutes stirring. An additional paramagnetic species is evident (labelled **IV** in Figure 6.10b), which is more evident in the parallel region. After a further 20 minutes of stirring (Spectrum 6.10c), there is a slight shift in the hyperfine parameters of this second paramagnetic species (labelled **III**), as shown in Table 6.3. The relative intensity of this second species (as determined through simulation) also increased from ~23% after 5 minutes stirring to ~38% after 25 minutes stirring. No further changes in these parameters were evident after a further 20 minutes of stirring (Spectrum 6.10d). Also, by this point, the parameters of the second paramagnetic species (**III**) are unanimous with that seen in Figure 6.9 (Table 6.2) in AcN:DMF (recorded after 5 hours stirring). This is evidence that species **III** is not simply due to a solvent effect and is therefore implicative of substrate interaction with the Cu(II) centre in the equatorial plane (due to the decrease in g_3 and increase in A_3). The spectra shown in Figure 6.10 have been integrated to monitor any change in [Cu(II)] concentration. The plot shown in Figure 6.11 shows no evidence of any change in the [Cu(II)] concentration. This investigation therefore provides no supporting evidence for the proposed redox mechanism of Jacobsen *et al.*,[6] since a reduction in concentration would be expected upon the formation of a Cu(III)-nitrene intermediate. However, the presence of the additional paramagnetic species (labelled **III**), could be implicative of a Cu(II) reaction intermediate. It should be noted that the investigations reported in this chapter (unless otherwise noted) were performed at room temperature. Evans *et al.*,[18]

reported a similar reaction temperature of 25ºC. However, Evans *et al.,*[18] suggested that it may be that the +2 oxidation state may not be accessible at lower temperatures (*e.g.*, -78ºC) and in less polar solvents, which were the conditions reported by Jacobsen.[6] It is possible that different observations in the EPR profile would therefore be made if the reaction was performed at much lower temperatures. It must also be considered that any redox change is short-lived and occurs within a timescale inaccessible to EPR.

The synthesis of [Cu(II)(**1a**)] and the catalytic reaction itself is generally performed *in-situ* for convenience, with Cu(II)(OTf)$_2$ and the appropriate BOX ligand stirred in solution prior to the addition of styrene and PhI=NTs. This can however lead to the presence of multiple species (unreacted Cu(II)(OTf)$_2$, heteroleptic [Cu(II)(**1a**)] and homoleptic [Cu(II)(**1b**)], see Scheme 4.1). Figure 6.12 shows an investigation which was performed *in-situ*. The spectrum was first recorded prior to substrate addition (Figure 6.12a). Styrene and PhI=NTs were then added to the solution of [Cu(II)(**1a**)] and [Cu(II)(**1b**)]. Aliquots of this solution were extracted after 15 minutes, 30 minutes, 1 hour and 24 hours of stirring (Figure 6.12b-e). Here the presence of [Cu(II)(**1a**)] and [Cu(II)(**1b**)] is evident throughout the series of spectra (6.12a-e). The absorptions in the parallel region which have been attributed to each of these species are highlighted with stick diagrams in Figure 6.12a and a'.

By comparison of Figure 6.12a and Figure 6.12b-e (specifically looking at the peaks highlighted with asterisks in Figure 6.12a,e) it can be seen that upon addition of PhI=NTs and styrene there is a decrease in the relative concentration of the homoleptic complex, [Cu(II)(**1b**)] (with two coordinated BOX ligands). The simulation parameters for Figure 6.12a-e shown in Table 6.4 support this. From the percentage contribution of the two species, as determined *via* simulation, the contribution of [Cu(II)(**1b**)] decreased from ~60% to ~50% within 15 minutes after substrate addition. This is interesting considering that the homoleptic complex (with two coordinated BOX ligands) is not the catalytically active species, since labile counterions are required for facile substrate interactions in the catalysis.[20] It is possible that this suggests that the presence of substrates is causing a bis(oxazoline) ligand to dissociate from the homoleptic complex [Cu(II)(**1b**)] to form the heteroleptic complex [Cu(II)(**1a**)]. After 24 hours reaction time, the relative contribution of [Cu(II)(**1b**)], decreased further to ~40%. Despite this change in the relative percentage of [Cu(II)(**1b**)], the spin Hamiltonian parameters for this species do not change after substrate addition or with increasing reaction time. In [Cu(II)(**1a**)] there is a very slight decrease in g_3 (from 2.321 to 2.312) and A_3 (from 488 to 486 MHz). This change in the hyperfine parameters is minimal and is not significant

enough to suggest substrate coordination, particularly since the change in A_3 is well within the error margin of ±6 MHz. If [Cu(II)(**1b**)] is converted to [Cu(II)(**1a**)] in the presence of the olefin and nitrene donor, these results could suggest that an excess of BOX ligand in the catalytic reaction mixture may not be overly detrimental to the yield of the reaction, although it is likely to have some negative impact on the rate of the reaction due to the additional time taken for the bis(oxazoline) to dissociate from [Cu(II)(**1b**)] to give [Cu(II)(**1a**)]. Hager et al.,[20] also suggest that the formation of the catalytically inactive [Cu(BOX)$_2$] is reversible.
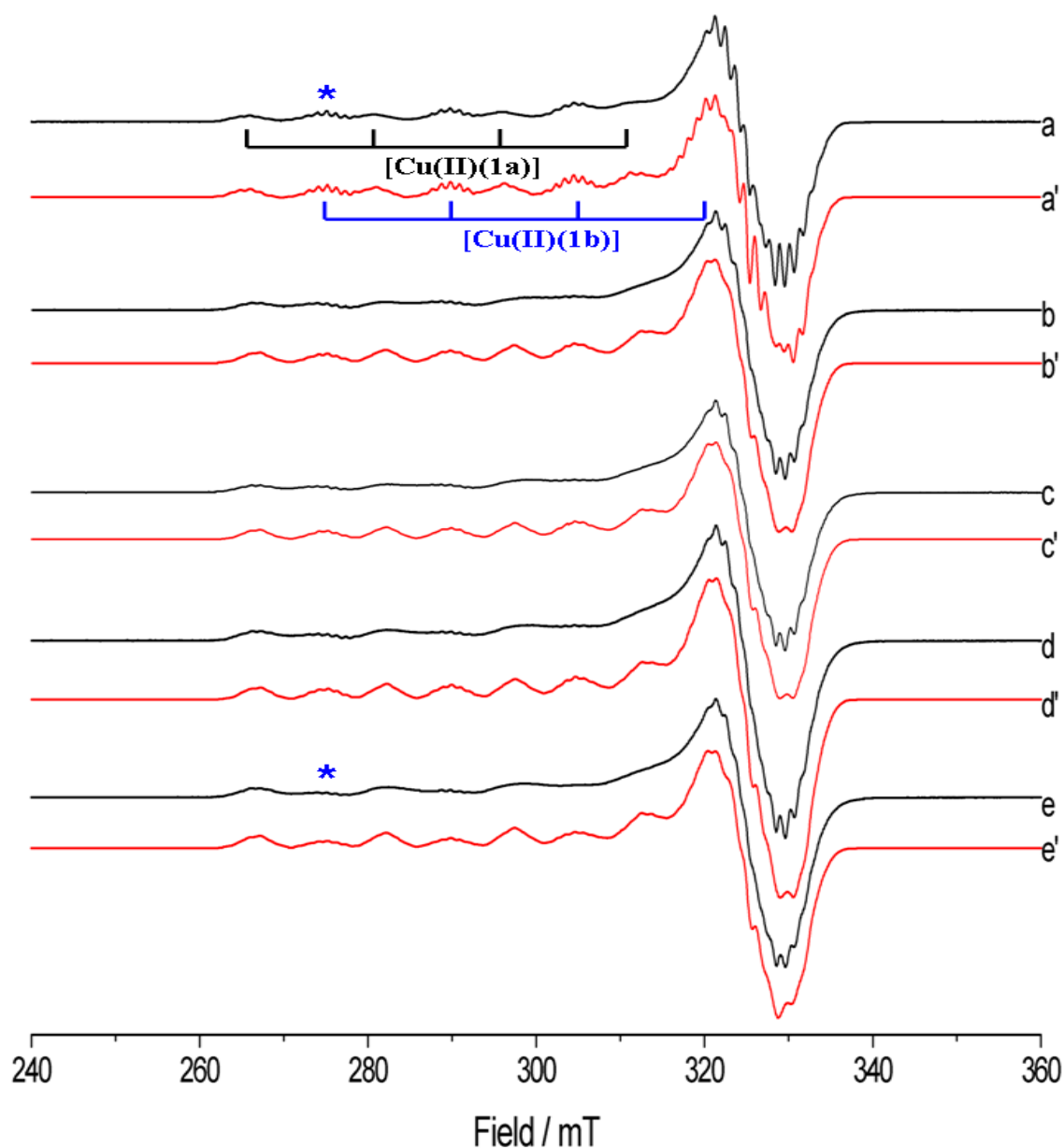
Figure 6.12 *X*-band CW-EPR spectra (140 K) of a) Cu(II)(OTf)$_2$: BOX (1:1.5) dissolved in MeOH:Tol (4:3) and after the addition of styrene and PhI=NTs with b) 15 minutes, c) 30 minutes, d) 1 hour, and e) 24 hours stirring. The corresponding simulations are given in a' – e' (red line). * highlights the intensity change in [Cu(II)(**1b**)].

Table 6.4 Experimental *g* and A^{Cu} spin Hamiltonian parameters for a mixture of [Cu(II)(**1a**)] and [Cu(II)(**1b**)] in MeOH:Tol (4:3), and after the addition of PhI=NTs and styrene with increasing reaction times.

Rxn. time / hours	Species	Relative % of species	$^a g_1$	$^a g_2$	$^a g_3$	$^b A_1$	$^b A_2$	$^c A_3$
0	[Cu(II)(**1a**)]	40	2.064	2.073	2.321	15	15	488
	[Cu(II)(**1b**)]	60	2.054	2.063	2.255	26	29	462
0.25	[Cu(II)(**1a**)]	50	2.064	2.073	2.312	15	15	486
	[Cu(II)(**1b**)]	50	2.054	2.063	2.255	26	29	462
0.5	[Cu(II)(**1a**)]	50	2.064	2.073	2.312	15	15	486
	[Cu(II)(**1b**)]	50	2.054	2.063	2.255	26	29	462
1	[Cu(II)(**1a**)]	50	2.064	2.073	2.312	15	15	486
	[Cu(II)(**1b**)]	50	2.054	2.063	2.255	26	29	462
24	[Cu(II)(**1a**)]	60	2.064	2.073	2.312	15	15	486
	[Cu(II)(**1b**)]	40	2.054	2.063	2.255	26	29	462

All *A* values given in MHz; [(a)] ±0.004; [(b)] ±3 MHz; [(c)] ±6 MHz.

In addition to using styrene as the olefin in the [Cu(II)(BOX)] catalysed asymmetric aziridination reaction, other olefins can be used.[7] Figure 6.13 presents an investigation in which PhI=NTs and cyclohexene were added to [Cu(II)(**1a**)] in order to compare the previous results (obtained using styrene) with the results obtained with this less reactive olefin. It is clear from the simulation parameters shown in Table 6.5 that there is very little change in the spectrum upon addition of PhI=NTs and cyclohexene, and the changes that are observed are within the given error margins. Evans *et al.*,[18] investigated the effect of a range of olefins on the copper-catalysed aziridination reaction. The authors focused on comparing the results obtained using styrene as the olefin with those obtained using cyclohexene as the olefin. Cyclohexene was chosen for this purpose as a representative aliphatic disubstituted olefin.[18] It was found that styrene gave extremely high yields (92%) of aziridine when using Cu(II)(OTf)$_2$ as the catalyst, whilst cyclohexene gave a much lower yield of 60%. This lower reactivity of cyclohexene explains why no change is seen in the EPR profile after addition of cyclohexene and PhI=NTs (Figure 6.13).
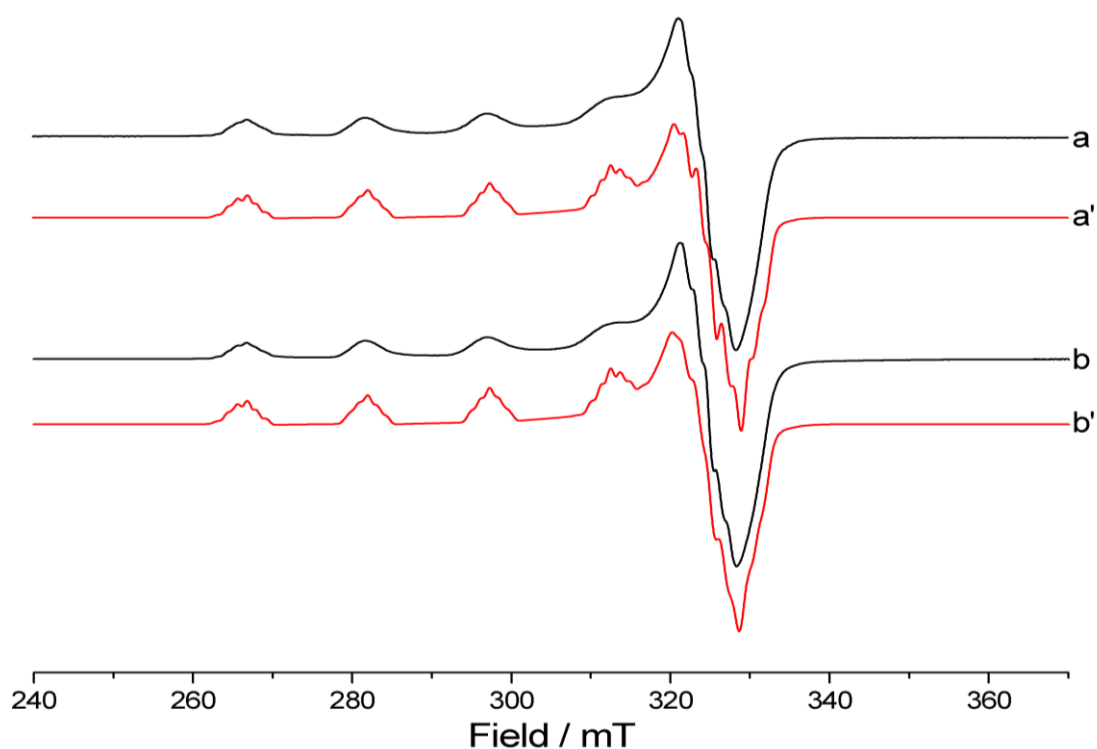
Figure 6.13 *X*-band CW-EPR spectra (140 K) of a) [Cu(II)(**1a**)] in AcN:DMF (4:1) and b) after the addition of cyclohexene and PhI=NTs. The corresponding simulations are given in a' – b' (red line).

Table 6.5 Experimental *g* and A^{Cu} spin Hamiltonian parameters for [Cu(II)(**1a**)] in AcN:DMF (4:1), and after the addition of PhI=NTs and cyclohexene after 5 hours stirring.

Rxn. time / hours	$^a g_1$	$^a g_2$	$^a g_3$	$^b A_1$	$^b A_2$	$^c A_3$
0	2.064	2.073	2.315	15	15	491
5	2.066	2.075	2.316	15	15	491

All *A* values given in MHz; [(a)] ±0.004; [(b)] ±3 MHz; [(c)] ±6 MHz. Solvent = 80% AcN, 20% DMF.

The effect of increasing the reaction temperature was then examined in order to monitor whether an increased reaction temperature results in more significant changes to the resulting EPR profile due to an increased rate of reaction. The temperature for the asymmetric aziridination of styrene was thus increased to 40ºC (see Figure 6.14) after the addition of styrene and PhI=NTs. Integration of the spectra (Figure 6.15) shows that the [Cu(II)] concentration decreased dramatically after substrate addition with stirring at 40ºC. Comparison of Figure 6.14a with Figure 6.14b-g shows that the absorptions in the parallel region are broader after the addition of styrene and PhI=NTs at 40ºC. The decrease in [Cu(II)] concentration may suggest that the Cu(II) was easily reduced to Cu(I) at this temperature. Table 6.6 shows the spin Hamiltonian parameters used to simulate Figures 6.14a and 6.14g. From these values, it can be seen that the changes in the hyperfine pattern are minimal, with only a small decrease in g_3 from 2.315 to 2.305.

However when [Cu(II)(**1a**)] without substrates was heated to this temperature, no changes in the spin Hamiltonian parameters or broadening of the absorptions in the parallel region were observed. This therefore could suggest that the presence of styrene + PhI=NTs is promoting the reduction of the Cu(II) at this increased temperature. However, since the aziridination reaction is commonly performed at room temperature, this result may not be a true representation of the catalytic reaction.[7,11]
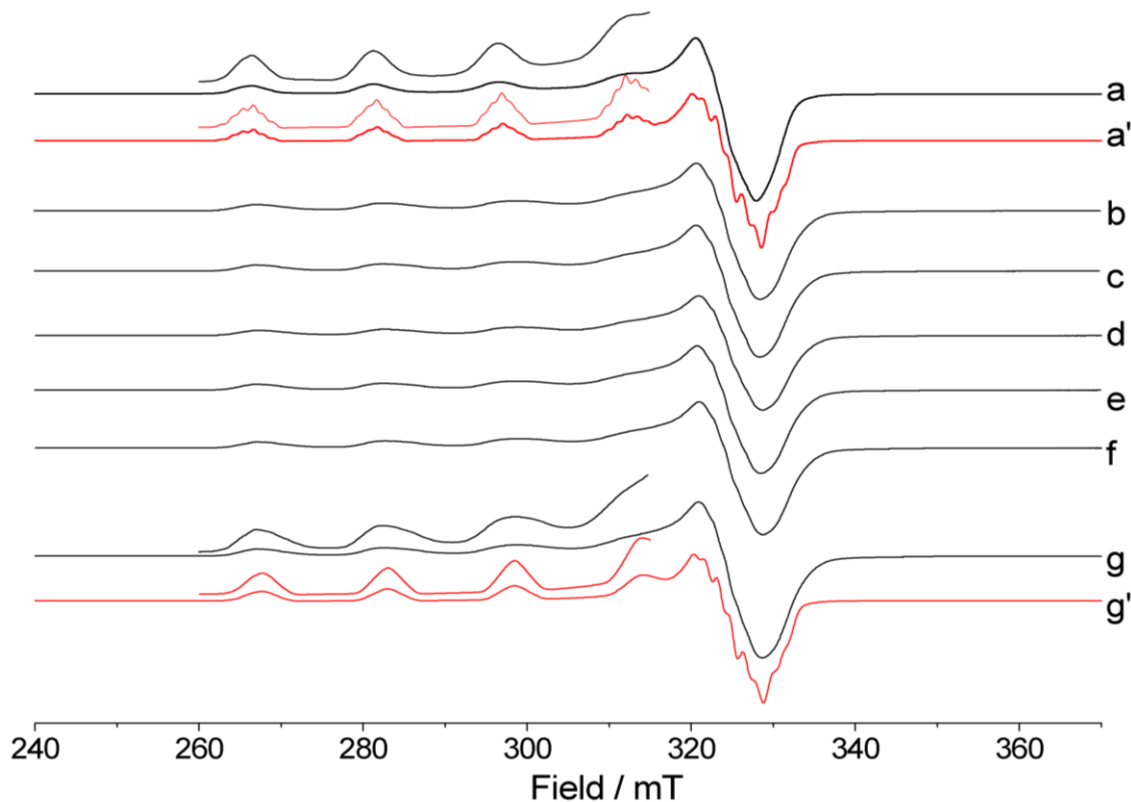
Figure 6.14 *X*-band CW-EPR spectra (140 K) of a) [Cu(II)(**1a**)] in AcN:DMF (4:1) and b) after the addition of styrene and PhI=NTs at 40 °C after b) 30, c) 60, d) 90, e) 120, f) 150 and g) 180 minutes stirring. The simulations of a and g are shown in a' and g' respectively. The expanded parallel regions of a, a', g and g' are also shown for clarity.
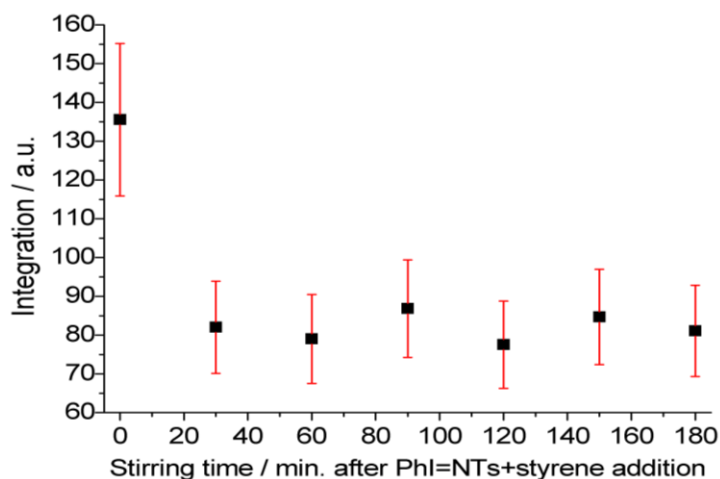
Figure 6.15 Integrated EPR signal intensities for [Cu(II)(**1a**)] and after addition of PhI=NTs + styrene at 40°C. Error bars (±15%) are shown in red.

Table 6.6 Experimental g and A^{Cu} spin Hamiltonian parameters for [Cu(II)(**1a**)] in AcN:DMF (4:1), and after the addition of PhI=NTs and styrene at 40ºC after 180 minutes stirring.

Rxn. time / mins.	Species	$^{a}g_1$	$^{a}g_2$	$^{a}g_3$	$^{b}A_1$	$^{b}A_2$	$^{c}A_3$
0	[Cu(II)(**1a**)]	2.064	2.073	2.315	15.0	14.5	490.9
180	[Cu(II)(**1a**)]	2.064	2.073	2.305	15.0	14.5	487.8

All A values given in MHz; [a] ±0.004; [b] ±3 MHz; [c] ±6 MHz. Solvent = 80% AcN, 20% DMF.

6.4 Discussion of results

Herein, the interaction of [Cu(II)(**1a**)] with the range of substrates utilised in the asymmetric aziridination reaction has been studied. Investigating the interaction of [Cu(II)(**1a**)] with pyridine exemplified the extent of the changes which may be observed in the EPR profile of [Cu(II)(**1a**)] upon substrate addition. In the case of pyridine addition, additional superhyperfine splitting arising from the interaction of the Cu(II) centre with the nucleophilic nitrogen of pyridine in the equatorial plane was observed, which suggested the replacement of a water molecule with pyridine. This result therefore demonstrates that EPR is a useful technique for studying substrate-complex interactions. Other substrates which are more relevant to aziridination were then investigated; iodobenzene, (diacetoxyiodo)benzene, styrene and PhI=NTs. The effect of these substrates on the resulting EPR profile was not as significant as the changes observed upon pyridine addition. No changes in the EPR profile were evident upon addition of iodobenzene or styrene, suggesting that there is little or no interaction between these substrates and the Cu(II) centre when they are added separately. Upon addition of (diacetoxyiodo)benzene, there was some evidence for the presence of a small amount (~5%, as determined *via* simulation) of an additional paramagnetic species (species **II**, Figure 6.3c). It has been suggested that this is either due to excess Cu(II)(OTf)$_2$ or axially coordinated acetic acid. Addition of increasing quantities of PhI=NTs resulted in a decrease in the Cu(II) concentration, as shown by integration. This may support the proposed redox mechanism of Jacobsen *et al.*,[6]; however the decrease in concentration was too small to confirm this with certainty. Furthermore, this was only observed when PhI=NTs alone was added to [Cu(II)(**1a**)] and not when both substrates required for the aziridination reaction (styrene and PhI=NTs) were added to [Cu(II)(**1a**)].

The aziridination reaction was then probed by recording a series of EPR spectra at different time intervals to follow the progress of the reaction. When using styrene as

the olefin and PhI=NTs as the nitrene donor, reactions performed in solvent systems of both AcN:DMF (4:1) and MeOH:Tol (4:3) revealed the formation of an additional paramagnetic species (species **III**, Figures 6.9, 6.10). There was some evidence of this after only 5 minutes stirring, but after 25 minutes stirring time the *g* and *A* values of this second paramagnetic species were almost identical in both solvent systems. This suggests that there is a direct interaction of substrate with the Cu(II) centre. The decrease in g_3 and the increase in A_3 imply that the equatorial environment of the Cu(II) centre has changed, perhaps due to an interaction of the nitrene moiety of PhI=NTs resulting in a change in geometry and electron spin distribution around the metal centre. No change was witnessed in the [Cu(II)] concentration, which could indicate that the reaction is catalysed through Cu(II), as suggested by Evans.[18] However, it is also possible that Cu(II) is simply the resting state of the catalyst and that any redox changes occur too quickly to be observable by EPR.

The resulting EPR spectra after addition of styrene + PhI=NTs to a mixture of heteroleptic [Cu(II)(**1a**)] and homoleptic [Cu(II)(**1b**)], seemed to suggest that a bis(oxazoline) ligand dissociates from the homoleptic complex in the presence of substrates to form the heteroleptic complex. This could be of significance if this means that the presence of a slight excess of bis(oxazoline) ligand does not hinder the yield of the catalytic reaction.

Reaction temperature and the choice of olefin were also found to influence the resulting EPR spectra. In order to determine whether an increased reaction temperature promoted a more significant change in the EPR profile by overcoming energy barriers, the reaction was performed at 40ºC. The addition of PhI=NTs + styrene to [Cu(II)(**1a**)] at this increased temperature resulted in a decrease in the overall [Cu(II)] concentration, perhaps due to the reduction of the Cu(II) centre to Cu(I). However, the [Cu(II)(BOX)] catalysed aziridination reaction is generally performed at room temperature and therefore the results from this investigation under increased reaction temperature should be considered with care as this may not be representative of the catalytic reaction.[7,11] To investigate the importance of olefin selection, cyclohexene was used instead of styrene to enable a comparison to be made using this less reactive olefin (cyclohexene). In contrast to the investigations in which styrene was used as the olefin, no evidence of the formation of an additional paramagnetic species was observed with cyclohexene.

As mentioned earlier, both Jacobsen and Brandt concluded that Cu(I) is the active species in the copper-catalysed aziridination of olfins.[6,19] Through density functional theory (DFT) calculations and kinetic experiments, Brandt *et al.,*[19] deduced

that a Cu(I)-PhI=NTs complex could not be the resting state for the catalytic cycle because of the favourable free energy of N-I bond dissociation (-3.6 kcal/mol). The authors explained that the Cu(III)-nitrene intermediate proposed by Jacobsen *et al.*,[6] is therefore immediately formed upon the dissociation of iodobenzene.[19] Brandt *et al.,*[19] used DFT calculations to illustrate that Cu(II) can also enter the Cu(I)/Cu(III) cycle suggested by Jacobsen.[6] Evans *et al.,*[18] conversely found evidence that PhI=NTs promotes catalyst oxidation with the chiral complex derived from Cu(I)OTf and bis(oxazoline), and proposed that the Cu(II) species therefore catalyses the reaction. Díaz-Requejo *et al.*,[8] agreed that the active catalyst is in a +2 oxidation state and suggested that the intermediate which attacks styrene is in fact an electrophilic, paramagnetic copper nitrene species (Scheme 6.4). It is difficult to determine with certainty from the EPR results collected in this work which of these proposed mechanisms is the most likely, although it can be argued that the results presented in this chapter do provide some supporting evidence for the Cu(II) intermediate suggested by Evans *et al.*,[18] and later by Díaz-Requejo *et al.*,[8] for the copper catalysed aziridination reaction.

6.5 Conclusion

In the current chapter, a detailed EPR investigation of the interaction of various substrates of relevance to the aziridination reaction (iodobenzene, (diacetoxyiodo)benzene, styrene and PhI=NTs) with [Cu(II)(**1a**)] has been presented. The [Cu(II)(**1a**)] catalysed asymmetric aziridination of styrene, with PhI=NTs as the nitrene source, has also been studied. Initially using pyridine as a model substrate, different g/^{Cu}A parameters and additional superhyperfine splitting in the perpendicular region were observed by EPR, indicative of an equatorial interaction of pyridine with the Cu(II) centre due to displacement of water. No changes in EPR profile were observed in the presence of iodobenzene or styrene, and only slight changes were observed in the presence of (diacetoxyiodo)benzene and PhI=NTs. Addition of the substrates used in the asymmetric aziridination reaction, styrene + PhI=NTs, to [Cu(II)(**1a**)] resulted in the formation of an additional paramagnetic species (labelled **III**). The g/^{Cu}A parameters of this species, as observed by EPR, demonstrate that the equatorial environment of the Cu(II) centre has changed. This may suggest that the active catalyst is in a +2 oxidation state, as concluded by Evans.[18] This catalytic intermediate may be in the form of a paramagnetic copper-nitrene, as suggested by Díaz-Requejo *et al.*[8] Integration of the spectra after addition of PhI=NTs + styrene

showed no change in the [Cu(II)] concentration, again suggesting a +2 catalyst oxidation state. It has also been considered that the Cu(II) state is simply the resting state of the catalyst and that any redox changes do not occur within a timescale accessible to EPR. This work also revealed that the addition of styrene + PhI=NTs to a mixture of heteroleptic [Cu(II)(**1a**)] and homoleptic [Cu(II)(**1b**)] resulted in a decrease in the relative intensity of [Cu(II)(**1b**)], suggesting that over a period of time, in the presence of substrates, the second bis(oxazoline) ligand dissociates from [Cu(II)(**1b**)] to form [Cu(II)(**1a**)]. Although the results presented in the current chapter have been inconclusive in gaining a complete understanding of the mechanism of copper-catalysed asymmetric aziridination, it can be surmised that an increased understanding of the complexity and sensitivity of the system has been accomplished. This was achieved by careful analysis of the extremely subtle changes in the EPR spectra upon substrate addition to [Cu(II)(**1a**)]. To conclude, more evidence has been gathered that supports a Cu(II) active catalyst oxidation state, as opposed to Cu(I) or Cu(III) intermediates.

6.6 References

1   Murphy, D. M.; Fallis, I. A.; Carter, E.; Willock, D. J.; Landon, J.; Van Doorslaer, S.; Vinck, E. *Physical Chemistry Chemical Physics,* **2009**, *11*, 6757.

2   Murphy, D. M.; Caretti, I.; Carter, E.; Fallis, I. A.; Göbel, M. C.; Landon, J.; Doorslaer, S. V.; Willock, D. J. *Inorganic Chemistry,* **2011**, *50*, 6944.

3   Vinck, E.; Carter, E.; Murphy, D. M.; Van Doorslaer, S. *Inorganic Chemistry,* **2012**, *51*, 8014.

4   Zamani, S.; Carter, E.; Murphy, D. M.; Van Doorslaer, S. *Dalton Transactions,* **2012**, *41*, 6861.

5   Clayden, J.; Greeves, N.; Warren, S.; Wothers, P. *Organic Chemistry*; Oxford University Press: Oxford, **2006**.

6   Li, Z.; Quan, R. W.; Jacobsen, E. N. *Journal of the American Chemical Society,* **1995**, *117*, 5889.

7   Evans, D. A.; Faul, M. M.; Bilodeau, M. T.; Anderson, B. A.; Barnes, D. M. *Journal of the American Chemical Society,* **1993**, *115*, 5328.

8   Díaz-Requejo, M. M.; Pérez, P. J.; Brookhart, M.; Templeton, J. L. *Organometallics,* **1997**, *16*, 4399.

9   Carter, E.; Murphy, D. M. In *Spectroscopic Properties of Inorganic and Organometallic Compounds: Volume 40*; The Royal Society of Chemistry: **2009**; Vol. 40, p 355.

10   Yamada, Y.; Yamamoto, T.; Okawara, M. *Chemistry Letters,* **1975**, 361.

11   Taylor, S.; Gullick, J.; McMorn, P.; Bethell, D.; Page, P. C. B.; Hancock, F. E.; King, F.; Hutchings, G. J. *Journal of the Chemical Society-Perkin Transactions 2,* **2001**, 1714.

12   Schweiger, A.; Günthard, H. H. *Chemical Physics,* **1978**, *32*, 35.

13   Pilbrow, J. R. *Transition Ion Electron Paramagnetic Resonance*; 1st ed.; Oxford Science Publications, Oxford University Press, **1990**.

14   Wagner, M. R.; Walker, F. A. *Inorganic Chemistry,* **1983**, *22*, 3021.

15   Peisach, J.; Blumberg, W. E. *Archives of Biochemistry and Biophysics,* **1974**, *165*, 691.

16   F. E. Mabbs; Collison, D. *Electron Paramagnetic Resonance of d Transition Metal Compounds*; Elsevier Science Publishers B.V.: Amsterdam, **1992**; Vol. 16.

17   Brustolon, M.; Giamello, E. *Electron Paramagnetic Resonance: A Practitioner's Toolkit*; John Wiley & Sons, Inc., **2009**.

18   Evans, D. A.; Bilodeau, M. T.; Faul, M. M. *Journal of the American Chemical Society,* **1994**, *116*, 2742.

19   Brandt, P.; Södergren, M. J.; Andersson, P. G.; Norrby, P. *Journal of the American Chemical Society,* **2000**, *122*, 8013.

20   Hager, M.; Wittmann, S.; Schätz, A.; Pein, F.; Kreitmeier, P.; Reiser, O. *Tetrahedron: Asymmetry,* **2010**, *21*, 1194.

Chapter 7

Conclusion

Asymmetric catalysis is a leading field of chemical research due to the importance of obtaining enantiomerically pure compounds. *Privileged chiral catalysts* are a particular class of asymmetric catalysts that result in excellent enantioselectivities for a variety of substrates and also for a range of mechanistically unrelated reactions. The fundamentals of catalysis, including an overview of the literature on asymmetric catalysis and privileged catalysts was provided in Chapter 1. The particular *privileged chiral catalyst* which has been investigated in this thesis is copper(II)-bis(oxazoline), labelled [Cu(II)(BOX)], which is an excellent catalyst for the asymmetric aziridination reaction. *X*- and *Q*-band EPR and ENDOR spectroscopies (described in Chapter 2) have been used to characterise a series of [Cu(II)(BOX)] complexes and to investigate the nature of any reaction intermediates in the asymmetric aziridination reaction.

After explaining the experimental procedures in Chapter 3, a detailed EPR and ENDOR investigation of a series of heteroleptic and homoleptic [Cu(II)(BOX)] complexes, labelled [Cu(II)(**1a-c**)], was presented in Chapter 4. Different g/^{Cu}A parameters were observed by EPR for the heteroleptic complexes [Cu(II)(**1a**)] and [Cu(II)(**1c**)], indicating that the choice of counterion significantly affects the geometries of these two complexes. When using an excess of the BOX ligand (**1**), formation of the homoleptic complex [Cu(II)(**1b**)] only occurred in the presence of the Cu(OTf)$_2$ salt; the CuCl$_2$ salt (with less labile Cl$^-$ counterions) prevented the coordination of a second bis(oxazoline) ligand. The hyperfine technique of ENDOR was used to determine the hyperfine (and where relevant quadrupole) parameters of the surrounding nuclei including ^{1}H, ^{14}N and ^{19}F. Comparison of the heteroleptic complexes, [Cu(II)(**1a**)] and [Cu(II)(**1c**)], revealed significant differences in the ligand derived ^NA values, consistent with the more distorted arrangement of the latter complex. Smaller ^NA and ^NP values were detected in the homoleptic complex, [Cu(II)(**1b**)], resulting from the redistributed spin density over the four nitrogen nuclei in the homoleptic complex. Well resolved ^{19}F couplings in [Cu(II)(**1a**)] confirmed the presence of coordinated TfO$^-$ counterions along the unique axial (*z*) direction. Strong ^{1}H couplings indicative of the presence of bound water molecules along the equatorial (*x,y*) direction were also observed. In Chapter 4, EPR/ENDOR was therefore successfully used to probe the inner- and outer-sphere coordination environment of [Cu(II)(BOX)] complexes in the catalytically relevant,

'solvated' environment where counterion effects are evident. The structures obtained by EPR and ENDOR for [Cu(II)(**1a**)] and [Cu(II)(**1c**)] were found to be consistent with the crystal structures reported by Evans and Thorhauge respectively.[1,2] Good agreement was also achieved between the experimental results and DFT calculations for these complexes.

The effects of changing the Cu(II):BOX ligand ratio and the counterion effect were further investigated in Chapter 5. Different ligand architectures were also examined to probe the effect of the substituents, both on the bridging carbon between the oxazoline rings and on the chiral carbon of the oxazoline rings. It was found that when using ligand **2**, coordination of two BOX ligands to the Cu(II) centre occurred when using both Cu(OTf)$_2$ and CuCl$_2$ starting salts. This was not the case with ligands **1** and **3** (for which only the presence of the more labile TfO$^-$ counterion enabled the formation of the homoleptic complex). This therefore suggests that the removal of the methyl groups has a direct influence on the electronic environment of the Cu(II) centre. CW-ENDOR was also used to probe the homoleptic complex, [Cu(II)(**2b**)] and further investigate the effect of the removal of the methyl groups from the bridging carbon. Larger *o*-phenyl and α-H couplings were observed in the ^{1}H ENDOR spectra of this complex in comparison to the analogous [Cu(II)(**1b**)], a direct result of replacing the methyl groups (which are electron donating by inductive effects) with proton groups (which have less directing effect on the electron spin, making more electron spin available for delocalisation around the ligand). Pulsed ENDOR of the heteroleptic complex, [Cu(II)(**3c**)], was recorded to explore the effect of replacing the phenyl groups with *tert*-butyl substituents.

In Chapter 6, [Cu(II)(**1a**)] was explored as a catalyst in the asymmetric aziridination of olefins. The suitability of EPR to investigate the interaction of this complex with substrates was demonstrated upon the addition of a 10-fold excess of pyridine. Here, clear evidence of additional superhyperfine splitting was seen resulting from the interaction of the Cu(II) centre with the nucleophilic nitrogen of pyridine in the equatorial plane, suggesting that the pyridine displaces one of the equatorially coordinated water molecules. Substrates with more relevance to the aziridination reaction were then investigated, including iodobenzene, (diacetoxyiodo)benzene, styrene and PhI=NTs. The changes observed in the EPR profile of [Cu(II)(**1a**)] upon substrate addition were minimal, suggesting that any interaction between the substrates and the Cu(II) centre is very weak when they are added separately. The [Cu(II)(**1a**)] catalysed asymmetric aziridination reaction was then probed using EPR to monitor and

follow the progress of the reaction. Addition of both styrene (the olefin) and PhI=NTs (the nitrene source) to [Cu(II)(**1a**)] resulted in the formation of an additional paramagnetic species (labelled **III**). The $g/^{Cu}A$ parameters of this additional species, as observed by EPR, evidences the change in the equatorial environment of the Cu(II) centre. Integration of the spectra after addition of PhI=NTs + styrene showed no change in the [Cu(II)] concentration. These observations could imply that the active catalyst is the Cu(II) species, as suggested by Evans *et al.*,[3] possibly as a paramagnetic copper-nitrene, as proposed by Díaz-Requejo.[4] Alternatively, this result could simply imply that Cu(II) is the resting state of the catalyst, where any redox changes involved in the reaction occur on a timescale inaccessible to EPR. This work also revealed that the addition of styrene + PhI=NTs to a mixture of heteroleptic [Cu(II)(**1a**)] and homoleptic [Cu(II)(**1b**)] results in a decrease in the relative intensity of [Cu(II)(**1b**)], seemingly implying that with time, the second bis(oxazoline) ligand dissociates from [Cu(II)(**1b**)] to form [Cu(II)(**1a**)]. Despite gaining an increased understanding of the effect of substrate interaction with the [Cu(II)(**1a**)] catalyst, the EPR spectra recorded did not provide enough evidence to fully understand the mechanism of the aziridination reaction. However, a Cu(II) reaction intermediate seems more probably than a Cu(III) intermediate, considering the presence of an additional paramagnetic species (**III**) and the lack of change in [Cu(II)] concentration upon addition of styrene + PhI=NTs.

In conclusion, EPR and ENDOR have been shown to be suitable techniques to investigate the *privileged chiral catalyst*, [Cu(II)(BOX)], in frozen solution. The effect of changing the counterion, ligand architecture and metal:ligand ratio have been studied. The choice of counterion was found to influence the geometry of the resulting complex, whilst the formation of the catalytically inactive homoleptic complex was found to depend on the choice of counterion and the ligand backbone. After characterising the [Cu(II)(BOX)] complexes [Cu(II)(**1a-c**)], [Cu(II)(**2a-c**)] and [Cu(II)(**3a-d**)], the catalytic reaction itself was investigated. The interactions of single substrates with [Cu(II)(**1a**)] were probed using EPR, before investigating the [Cu(II)(**1a**)] catalysed asymmetric aziridination of styrene, with PhI=NTs as the nitrene source. Limited changes were observed to the [Cu(II)] concentration which may suggest that Cu(II) is simply the resting state of the catalyst and any redox change in copper occurs on a timescale not accessible to EPR. The formation of an additional paramagnetic species upon addition of styrene and PhI=NTs, and the lack of evidence of a change in the [Cu(II)] concentration, could however be indicative that the active catalyst intermediate is a Cu(II)-nitrene adduct.

7.1 References

1   Evans, D. A.; Burgey, C. S.; Paras, N. A.; Vojkovsky, T.; Tregay, S. W. *Journal of the American Chemical Society,* **1998**, *120*, 5824.

2   Thorhauge, J.; Roberson, M.; Hazell, R. G.; Jorgensen, K. A. *Chemistry - A European Journal,* **2002**, *8*, 1888.

3   Evans, D. A.; Bilodeau, M. T.; Faul, M. M. *Journal of the American Chemical Society,* **1994**, *116*, 2742.

4   Díaz-Requejo, M. M.; Pérez, P. J.; Brookhart, M.; Templeton, J. L. *Organometallics,* **1997**, *16*, 4399.